# A LOW-COST SHORT-DISTANCE THERMAL CONDUCTION PRESSURE SENSOR

by

Yan Ma
B.E. in Electrical Engineering
Huazhong University of Science and Technology, 1990

THESIS SUBMITTED IN PARTIAL FULFILLMENT OF
THE REQUIREMENTS FOR THE DEGREE OF

MASTER OF APPLIED SCIENCE

In the School
of
Engineering Science



SIMON FRASER UNIVERSITY

Fall 2004

# APPROVAL

**Name:** Yan Ma

**Degree:** Master of Applied Science

**Title of Thesis:** A Low-Cost Short-Distance Thermal Conduction Pressure Sensor

**Examining Committee:**

**Chair:** **Dr. Steve Hardy**
Professor of the School of Engineering Science

---

**Dr. Albert M. Leung**
**Senior Supervisor**
Professor of the School of Engineering Science

---

**Dr. John D. Jones**
**Supervisor**
Professor of the School of Engineering Science

---

**Dr. Ash M. Parameswaran**
**Internal Examiner**
Professor of the School of Engineering Science

**Date Defended/Approved:** Nov. 24, 2004

# SIMON FRASER UNIVERSITY

# PARTIAL COPYRIGHT LICENCE

# ABSTRACT

A low-cost thermal pressure sensor based on short-distance thermal conduction and used in atmospheric pressure range has been explored. This simple device consists of a heater made of a polysilicon resistor, a heat sink made by the silicon substrate and a tiny air gap between them. With innovative ideas and simple processes, the gap can be made in the order of nanometers inexpensively, which significantly increases the measurement range of the sensor. Devices capable of measuring 700kPa (7atm) or more have been fabricated with a 3-mask, 3μm and CMOS compatible process. The device can be made as small as $50x50\mu m^2$, less than the size of a standard bonding pad. The simple process and low cost associated with these devices could make commercial adaptation promising.

# DEDICATION

To my husband Hongfei and my son Brian for their love and support

# ACKNOWLEDGEMENTS

I wish to express my deep gratitude to my senior supervisor, Dr. Albert M. Leung for his skilful guidance, patient support and valuable advices of my work over the years. As a supervisor, he not only shared his vast amount of knowledge with me, also taught me various practices and skills that are lifetime valuable.

I am very thankful to my supervisor, Dr. John Jones, for his insightful comments and advice. My gratitude also goes to Dr. Ash M. Parameswaran, for many helps during these years as well as serving examiner of the committee, patiently reading through my thesis and providing valuable feedback. My gratitude also goes to Dr. Steve Hardy, for serving chair of the committee.

I would like to express my sincere thanks to Ms. Eva Czyzewska and Mr. Bill Woods for their many helps in the cleanroom.

I would like to express my sincere thanks to my fellow graduate student Ming Lu for his kind help over these years.

Last but not least, I am very grateful to my parents and my husband for their continuous moral support and encouragement. I hope I will make them proud of my work, as I am proud of them.

# TABLE OF CONTENTS

# LIST OF FIGURES

# LIST OF TABLES

# GLOSSARY

| | |
|---|---|
| $A$ | area |
| $C_v$ | the specific heat at constant volume |
| $C_p$ | the specific heat at constant pressure |
| $d$ | the gap height, or the distance travelled by gas molecules, characteristic dimension of the container |
| $k$ | thermal conductivity of materials |
| $k_c$ | thermal conductivity of gases in continuum range |
| $k'$ | Boltzmann's constant, equal to $1.3807\times10^{-23}$ J/K |
| $K_N$ | the Knudsen number, the ratio between the MFP and the travel distance of the gas molecules |
| $l$ | distance |
| $m$ | mass |
| $n$ | the number of moles of gas (mole is defined as the amount of a substance that contains Avogadro number, $6.023 \times 10^{23}$, molecules), |
| $P$ | pressure |
| $Pr$ | the Prandtl number, is a dimensionless number approximating the ratio of momentum diffusivity and thermal diffusivity, equal to $\nu/\alpha$ |
| $P_{tr}$ | transition pressure |
| $Q$ | heat transfer rate |
| $q$ | heat flux, equal to Q/A |
| $R$ | the universal gas constant, equal to 8.3145 J/mol K |
| $T$ | temperature |
| $V$ | volume |
| $v$ | velocity |
| $v_{ave}$ | the average molecular velocity |
| $\Delta T$ | temperature difference |
| $\alpha$ | thermal diffusivity or temperature coefficient of resistance (TCR) |
| $\lambda$ | mean free path of gas molecules |
| $\gamma$ | the ratio of specific heats, equal to $C_p/C_v$ |
| $\nu$ | kinematic viscosity |
| $\rho$ | the molecular density<br>the electrical resistivity of a material |
| $\xi$ | the coefficient denoting the percentage of the solid contact area that takes in the beam area in the heater |

# CHAPTER 1 INTRODUCTION

## 1.1 Pressure Sensor

A pressure sensor is a device whose output is determined by the applied pressure. Depending on the sensing principle and the type of the output signals, pressure sensors are classified into four types as elastic-member, gravitational, electrical/thermal and strain gage [1].

Amongst these sensor types, the diaphragm pressure sensor is widely used because of its electrical output, moderate precision and wide pressure measurement range [1]. The sensor consists of a pressure reference chamber sealed by a diaphragm [37]. The deflection in the diaphragm resulting from the pressure change can be measured by resistance, capacitance, or reflected light [1]. The limitations of the diaphragm sensor are damages from excessive pressure, limited dynamic range, higher manufacturing cost, and long-term stability issues [1, 37].

The device presented in this thesis is a gas pressure sensor similar to the Pirani gauge [2, 7]. It has no moving or bending parts so there is no inherent overpressure limit. A low-cost fabrication method is employed and the experimental results demonstrate the potential for a commercial design with moderate precision.

## 1.2 Pirani Gauge

The Pirani gauge, invented by Italian Marcello Pirani in 1906, utilizes the thermal conductivity of a gas to detect pressure changes when the pressure is below a limit [7]. It is the first of the thermal conduction pressure sensors. The sensor simply consists of a hot wire with a temperature-dependent electrical resistance [2]. The temperature of the wire is determined by the constant electrical power that heats the wire and the heat loss to the environment by the thermal

conduction of the surrounding gas. Higher pressure brings more gas molecules in contact with the wire and reduces the temperature of the wire. The resistance of the wire changes with the temperature and becomes a measure of the pressure.

Some Pirani gauges use temperature probes to directly monitor the temperature of the wire. Traditional Pirani sensors are extensively used as inexpensive vacuum sensors for pressure sensing in the range between 100mPa and 100kPa [2]. Because their sensitivity depends on the gas type and temperature, Pirani gauges are not very stable or accurate.

## 1.3 Micromachined Pirani Sensor

There have been significant progresses in the miniaturization of Pirani sensors since the advent of silicon micromachining. The benefits of micromachining are simple design and robust device, low-cost fabrication, low power consumption and fast response. These advantages, as well as the prospect of digital sensors and integrated system-on-chip, have led to the development of many micro-Pirani sensors over recent years.

Figure 1-1 illustrates the conceptual structure of a micro-Pirani sensor, which consists of a heater and a heat sink separated by a small air gap. The most important dimension in the system is the gap between the heater and the heat sink, which determines the pressure measurement range. A sensor with a smaller gap can measure a higher pressure.

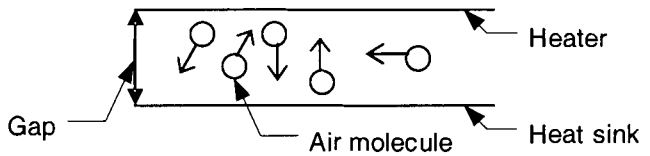


**Figure 1-1 Conceptual structure of a micro-Pirani sensor**

Most micromachined Pirani sensors operate in the vacuum pressure range, a pressure range well below 1atm (101kPa), because a small gap is hard to make without complicating the manufacturing processes and increasing the cost. The common procedure is to shrink the gap and

keep the heater membrane straight without touching the heat sink. When the gap reduces to the sub-micron range, this procedure becomes challenging because of the surface tension and the stiction effect in the structure-releasing step. Details will be discussed in Chapter 3. Some novel but rather complicated and expensive ideas have been proposed [3, 4].

The sensor we made, based on the same working principle, measures higher pressure (atmospheric or above) with a simple and low-cost fabrication procedure. Contrary to other methods of holding the heater membrane straight at a high cost, we allow it to collapse. Taking advantage of the surface irregularities of the heater, a tiny air gap can be made inexpensively. The measurable pressure range has been extended to more than 7atm (700kPa), much higher than that of the existing sensors. The procedure only needs three masks with a 3μm CMOS-compatible technology.

The functional device designed and fabricated in Simon Fraser University's (SFU) cleanroom consists of four identical polysilicon resistors; two of them are sensing elements (called heaters) suspended over the silicon substrate by a tiny air gap and are used for pressure measurement; the other two are dummy resistors that lay directly on the substrate and are used for temperature compensation. All of the resistors have the same structure and dimensions as beams embedded in silicon dioxide ($SiO_2$) films. The sensor is tested by connecting the four resistors in a Wheatstone bridge configuration, although each heater can be tested individually as well. The finished micro-beam structures are typically 150$\mu$m long, 6$\mu$m wide and 0.55$\mu$m thick. The gap between the collapsed heater structure and the substrate is estimated to be in the nanometer range.

## 1.4 Thesis Outline

Chapter 2 introduces the basic principles and the related work. The design and fabrication procedures are discussed in Chapter 3. Chapter 4 presents the experimental results, followed by discussions in Chapter 5. Chapter 6 is the conclusion, followed by Appendices and References.

# CHAPTER 2 BACKGROUND

This chapter introduces the basic concepts and principles used in our research, including the kinetic theory of gases, heat conduction and thermal conductivity. The first section introduces the concepts of mean free path of gas molecules, the Knudsen number, the continuum and non-continuum gas behaviours; the second section discusses the heat conduction, the contact thermal conductance, and the surface irregularities of two solid contact areas. The chapter concludes with a summary of related research work.

## 2.1 Kinetic Theory of Gases

### 2.1.1 Properties of Gases

Gas consists of molecules in random and rapid motion. The motion of the molecules provides them with kinetic energy ( $K_E = \frac{1}{2}mv^2$, where $m$ is mass and $v$ is velocity of the molecules). The temperature of the gas corresponds to the kinetic energy of the gas molecules and hence the speed at which they are moving.

Gas molecules constantly collide with each other or anything in their vicinity. They are so small and so far apart that their volume is negligible compared to the total volume. The molecules repel each other upon collision because the attractive forces between them are negligible [5]. The collisions result in no loss of kinetic energy, but kinetic energy can be transferred from one molecule to another. The rapid motion and lack of attractive forces of the gas molecules explains why gas molecules expand to occupy the volume of an enclosed container. The molecules continue to move until they collide with the inside wall of the container. The number of collisions per unit area determines the pressure the gas exerts on the container [5].

Ideal gases obey the perfect gas law $PV=nRT$, where $P$ is pressure (Pascal in SI units), $V$ is volume ($m^3$), $n$ is the number of moles of gas (mole is defined as the amount of a substance that contains Avogadro number, $6.023 \times 10^{23}$, molecules), $R$ is the universal gas constant, equal to 8.3145 J/mol K and $T$ is temperature (Kelvin).

### 2.1.2 Mean Free Path of Gas Molecules

The average distance travelled by a gas molecule before colliding with another one is known as its mean free path (MFP). Considering gas molecules as elastic spheres with an average diameter $\sigma$, a mean free path can be estimated from kinetic theory as

$$\lambda = \frac{k'T}{\sqrt{2}\pi P\sigma^2} \tag{2.1}$$

where $k'$ is the Boltzmann's constant and equal to $1.3807\times10^{-23}$ J/K; $T$ is the absolute temperature of the gas and $P$ is the pressure [5].

The $\lambda$ is inversely proportional to pressure, for example, for air at room temperature, $\lambda$ is about 80m when the pressure is $1.3\times10^{-4}$Pa; the number becomes 0.1μm at 101kPa.

### 2.1.3 The Knudsen Number

At low pressure in a confined volume, the molecular MFP is relatively large; most of the collisions that a molecule makes are with the walls of the container, not with other gas molecules. The average distance between collisions is no longer $\lambda$ but simply the characteristic dimension of the container $d$. The gas behaviour is different from that at high pressure.

The Knudsen number $K_N$ is the dimensionless parameter that characterizes the gas behaviour at low pressure [8]. It is defined as the ratio of the molecular MFP $\lambda$ to the characteristic dimension of the container $d$, which is the distance travelled by gas molecules [8].

$$K_N = \frac{\lambda}{d} \tag{2.2}$$

For $K_N < 10^{-3}$ the gas can be treated as a continuum [8]. For Knudsen numbers in the range of $10^{-3} \leq K_N \leq 10$, the gas may be considered rarefied [8]. The rarefied gas range has traditionally been further divided into the slip-flow regime ($10^{-3} \leq K_N \leq 0.1$) and the transitional flow regime ($0.1 < K_N \leq 10$) [8]. Gases with Knudsen numbers greater than 10 are considered free molecular gases [8]. Pirani sensor works in the non-continuum range where the Knudsen number is larger than $10^{-3}$.

## 2.2 Heat Conduction and Thermal Conductivity

Fourier's law indicates that the rate of heat conduction through a material is proportional to the temperature difference across the material and to the area perpendicular to heat flow and inversely proportional to the distance travelled by the flow [9]. With the notation indicated in Figure 2-1 ($A$ for area, $l$ for distance and $T$ for temperature), Fourier's law is expressed as

$$Q = \frac{kA}{l}(T_1 - T_2). \tag{2.3}$$

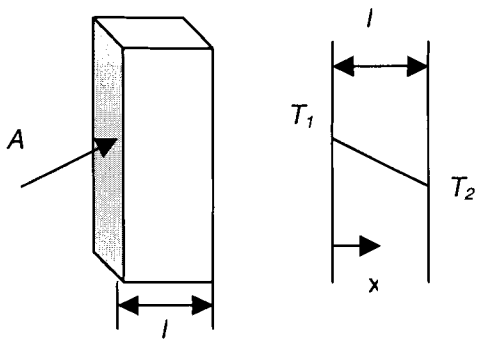


**Figure 2-1 One-dimensional steady-state heat conduction**

Equation (2.3) may also be written as,

$$q = \frac{Q}{A} = -k\frac{dT}{dx} \quad . \tag{2.4}$$

The quantity $q$ is called heat flux, which is the heat transfer rate per area. The minus sign is used because the heat flows in the opposite direction to the temperature gradient.

The thermal conductivity $k$ is the constant of proportionality in Fourier's law. It is a property of the conducting material and of its state. The thermal conductivity varies a lot with different materials. Generally gases have the lowest values, followed by good insulators, nonmetallic liquids, nonmetallic solids, liquid metals, metal alloys, and finally, the best group of conductors, pure metals [9]. The thermal conductivities of a material are affected by its state, like temperature and pressure. Some may vary with different directions through the materials [9].

### 2.2.1 Thermal Conductivity of Gases

In a container filled with a gas, heat is conducted by the random movement of molecules. The presence of a hot body in the container sets up a temperature gradient with the gas closer to the heat source getting hotter. Some of the fast-moving molecules from higher-temperature regions randomly reach the lower-temperature regions, while slower molecules in the lower-temperature regions reach higher-temperature regions by a similar random process [9]. Energy is exchanged. The thermal conductivity depends upon the density, the MFP, and the speed of the molecules [9].

#### 2.2.1.1 In the Continuum Regime

In the continuum regime, the characteristic dimension of the container is much larger than the MFP of the molecules ( $K_N < 10^{-3}$ ), the molecules collide with each other before hitting the wall of the container. Energy is exchanged by the intermolecular collisions; the $k$ of a gas is given from kinetic theory by [12, 26]:

$$k_c = \frac{1}{3}\rho v_{ave}\lambda C_v \tag{2.5}$$

where $\rho$ is the molecular density, $v_{ave}$ is the average molecular velocity, $\lambda$ is the MFP, $C_v$ is the specific heat at constant volume.

Since $\lambda$ is inversely proportional to pressure and $\rho$ is proportional to pressure, the thermal conductivity of a gas $k$ does not change with pressure in the continuum regime. It is 0.026 W/m K for air at room temperature and atmospheric pressure.

#### 2.2.1.2 In the Non-continuum Regime

When the characteristic dimension of the container is reduced to be in the order of molecular MFP or lower, molecules can reach the walls of the container without hitting other molecules on the way. This process is actually less efficient than that of the intermolecular collisions, so the conductivity falls off [7]. In the non-continuum regime, the thermal conductivity of gases is approximately proportional to pressure and becomes [9]

$$k = \frac{k_c}{\left[1 + \frac{2K_N}{\Pr}\left(\frac{2\gamma}{\gamma+1}\right)\right]}. \tag{2.6}$$

The Prandtl number $Pr$ is the ratio of the fluid viscosity $\nu$ to the thermal diffusivity $\alpha$, expressed as $Pr = \nu/\alpha$ [2]. The value of $Pr$ describes the relation between the diffusion of momentum and that of heat in a fluid [2]. For ideal gases, $Pr$ has a value near unity; for real gases, $Pr$ is about 0.7 [2]. The parameter $\gamma$ is the ratio of the specific heat at constant pressure to that at constant volume, denoted as $C_p/C_v$. It is always greater than unity, approximately 1.6 for monatomic gases, 1.4 for diatomic gases and approaches unity for gases with more complex molecules [2]. In (2.6) $k_c$ is the constant value of the thermal conductivity in the continuum regime and the upper limit of $k$. Using $Pr = 1$, $\gamma = 1$, (2.6) can be simplified as

$$k = \frac{k_c}{1 + 2\frac{\lambda}{d}} \tag{2.7}$$

Figure 2-2 gives the values of $k$ changes with pressure for $d$=400nm using (2.7) with $k_c$=0.026W/m K.

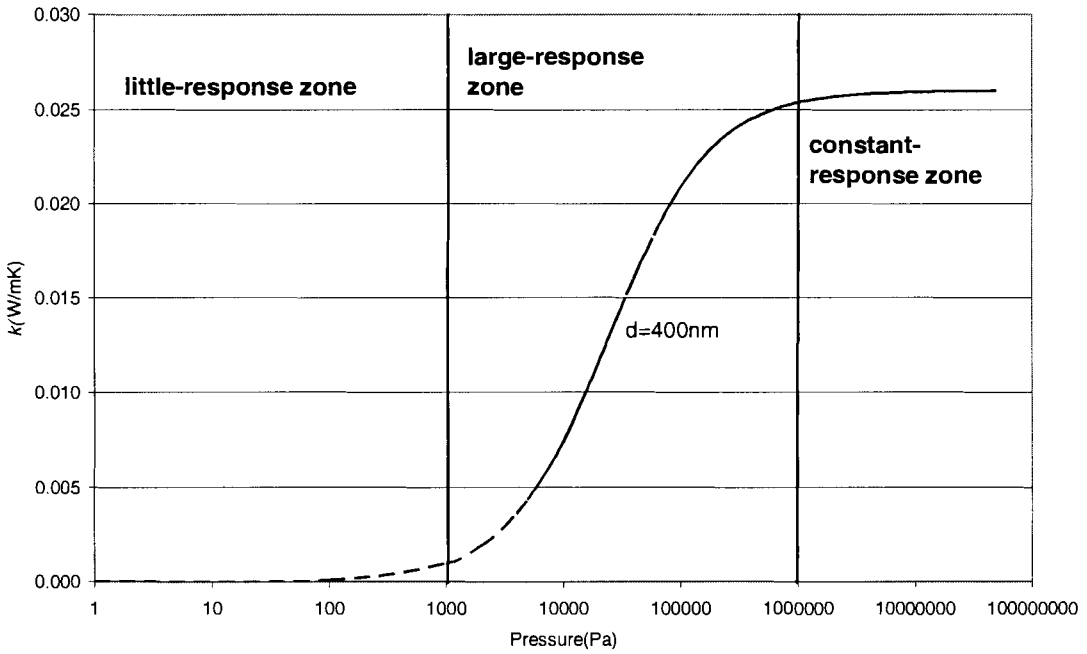


**Figure 2-2 Thermal conductivity $k$ changes with pressure and the three response zones**

In Figure 2-2, the $S$-shape curve of $k$ can be divided into three zones according to its response to pressure: little-response zone, large-response zone and constant-response zone. In the little-response zone when pressure is very low, there are simply not many gas molecules available for thermal conduction, radiation and thermal conductions through the solid contacts dominate. Since these heat losses are independent of pressure, the thermal conductivity overall changes little with pressure. With pressure rising, gas thermal conduction becomes significant and from (2.7), when $\lambda$ is much larger than the distance $d$, $k$ changes almost linearly with pressure. This is the large-response zone. However, when pressure keeps rising to the point where $\lambda$ is comparable to

$d$, the change of $k$ slows down and eventually approaches the constant value in the constant-response zone. Our design focuses on the gas behaviours in the large-response zone and tries to extend the transition pressure that delimits the large-response and the constant-response zones.

Transition pressure $P_{tr}$ is the pressure range where the gas transits from the non-continuum regime to the continuum regime. During the transition period, the sensor's response to pressure change slows down and eventually becomes independent of pressure.

Figure 2-3 gives the values of $k$ calculated using (2.7) for three different $d$ values, 2000nm, 400nm and 50nm. The curves clearly shift to right with a decrease in $d$, which means a higher transition pressure.

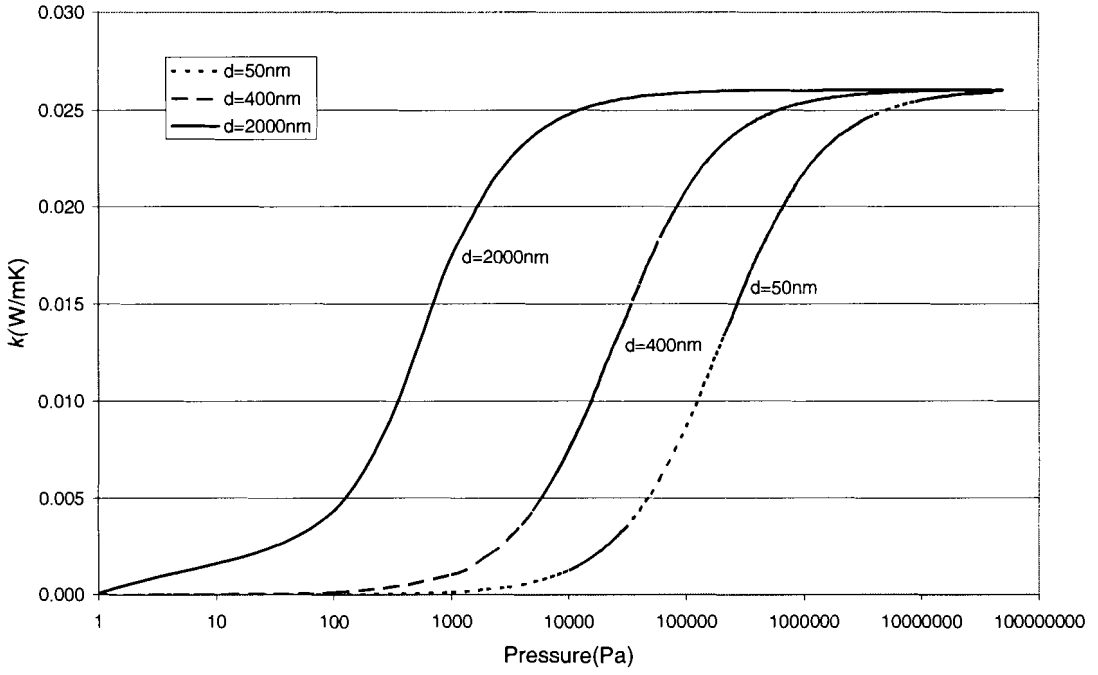


**Figure 2-3 Thermal conductivity $k$ changes with pressure for various $d$**

The experimental relationship between $P_{tr}$ and $k$ is expressed as [2–4]

$$k = \frac{k_c}{1+\frac{P_{tr}}{P}}. \tag{2.8}$$

Combining (2.6) and (2.8), transition pressure can be expressed as

$$P_{tr} = \frac{2K_N}{\Pr}\left(\frac{2\gamma}{\gamma+1}\right)P. \tag{2.9}$$

Equation (2.9) proves that transition pressure $P_{tr}$ is inversely proportional to $d$.

### 2.2.2 Surface Irregularities of Contacts

The reason we can still measure pressure by the gas thermal conduction even though the heater collapses to the heat sink is because of the surface irregularities of the contacts between the heater and the heat sink. Surface irregularities consist of macroscopic and microscopic irregularities. Macroscopic irregularities include flatness deviations and waviness while microscopic irregularity is measured by surface roughness [10]. Both irregularities exist in all practical solid surfaces. "Two solid surfaces apparently in contact only touch each other at a few individual spots. Even at relatively high contact pressure (of the order of 10MPa), the actual contact area for most solid surfaces is only about 1 to 2% of the nominal contact area [10]".

Figure 2-4 illustrates a magnified view of an interface between two materials in contact.

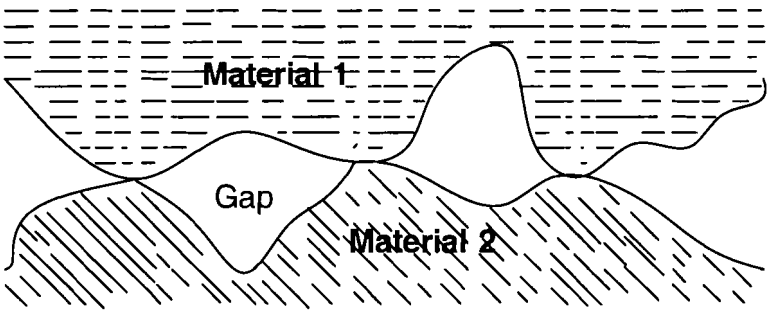


**Figure 2-4 Surface irregularities of the interface between two materials**

Heat may be transferred through this kind of interface in the following three ways [10]:

a. Conduction through the actual contact spots.

b. Conduction through the medium in the gap, such as air.

c. Radiation.

The thickness of the interfacial gap usually is too small for convection currents to set up. "Convective heat transfer can be neglected for gap widths less than about 6mm (corresponding to Grashof numbers of 2000 for air at pressure of 101kPa and temperature of 300K) [10]". Radiation is neglected because the temperature of the contacts is less than 300°C [10]. This leaves the heat transfer to only the conductions through the contact spots and the air gap. Because the actual contact areas only accounts to 1 to 2% of the total area even at relative high contact pressure, so at low contact pressure (up to several hundred kPa), heat transfer is predominantly "b", the conduction through the air gap [10].

## 2.3 Related Work

In 1985, A.W. Van Herwaarden et al introduced an integrated vacuum sensor (shown in Figure 2-5). From then on, extensive researches have been conducted in the micro-Pirani sensor.

The vacuum gauge made by Van Herwaarden was capable of measuring pressure from 1mPa to 1kPa. It consisted of a heating resistor and a thermopile integrated in a cantilever beam suspended over a heat sink. The temperature of the heating resistor was measured by the thermopile and determined by the constant electrical heating power and the heat loss to the environment. The heat was lost partly through the beam and partly through the gas to the sink. The thermal conductance of the beam and the gap between the beam and the heat sink determined the magnitude of losses [36].

Van Herwaarden went on to analyse the performance of integrated thermopile vacuum sensors in his 1988 paper [14]. The performance of two sensor structures shown in Figure 2-5, the cantilever-beam (a) and floating-membrane (b), was evaluated in thermal conduction and convection situations under three different pressure ranges: up to 10mPa, 1–100Pa and 5–50kPa.

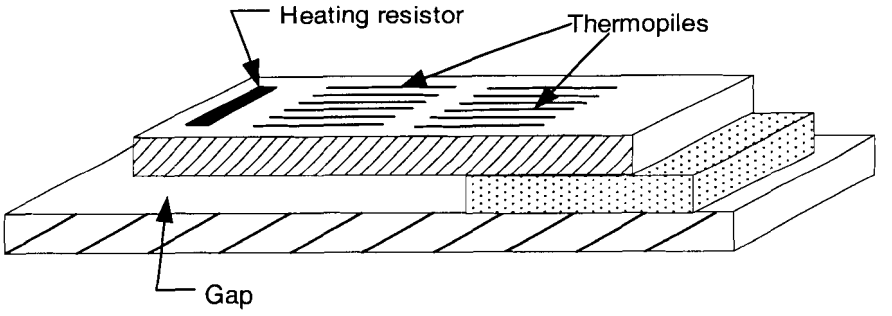


**(a) Cantilever beam**

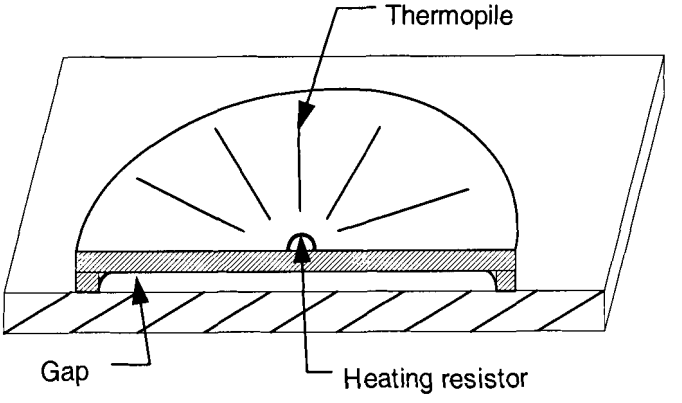


**(b) Floating membrane**

**Figure 2-5 Structures of two sensors made by Van Herwaarden**

[Van Herwaarden, 1985/1988, redrawn by author with permission from Elsevier]

In 1988, R. E. Higashi et al introduced a micro absolute pressure sensor with pressure range from 0.015psia (103.4Pa) to 150psia (1.03MPa) under constant power operating mode [1].

The device was fabricated on standard (100) silicon wafers with a simple four-mask process. The sensing element was a slim temperature-sensitive resistor (NiFe) embedded in a silicon nitride microbridge. A V groove was anisotropically etched underneath the microbridge to enhance the thermal isolation for the sensor. The microbridge was typically 90μm long, 6μm wide and 0.75μm thick. The cavity was approximately 25μm deep while the nearest distance between the edge of the microbridge and the substrate was typically 2μm [1].

In 1991, C. H. Mastrangelo and R. S. Muller introduced an integrated absolute pressure digital meter using a polysilicon microbridge as the sensing element. "The device consists of a microbridge, a constant-resistance (temperature) active bias circuit, and an 8-b successive-approximation register A/D converter, all implemented on the same substrate with a 4$\mu$m NMOS technology merged with the microsensor process. The chip, which contained about 1000 devices, was sensitive to variations in absolute gas pressure between 10Pa and $10^4$Pa [15]."

The microbridge was an n+ polysilicon beam coated with low-stress silicon nitride suspended over a 25μm-deep V groove etched into the silicon substrate. The beams were typically 400μm–600μm long, 1μm thick and 3μm wide. The process takes 14 masks.

In 1992, A.M. Robinson and M. Parameswaran reported a microstructural polysilicon device used as a pressure sensor. The sensor was fabricated in a standard CMOS process in the form of a suspended platform structure [16].

The sensing element was a pair of CMOS polysilicon resistors sandwiched between the field and the chemical vapour deposited (CVD) oxide layers [16]. A V groove similar to the above two separated the sensing element with the silicon substrate.

As shown in Figure 2-6, the cavity, in the form of a trench, was 200μm wide and approximately 50μm deep. "The 53μm × 48μm platform is supported by four diagonal arms of oxide and polysilicon, extending from one side of the trench to the other, with a meandering pattern on the platform. The total length of the resistor is approximately 340μm." The test was conducted by passing a constant current through the polysilicon resistor and monitoring the voltage drop across it. The devices reported were not fabricated specifically nor optimally designed for pressure sensing. However, it showed a 2% change over the pressure range from 0.01torr (1.33 Pa) to 100torr (13.3kPa) under a current of 200μA.

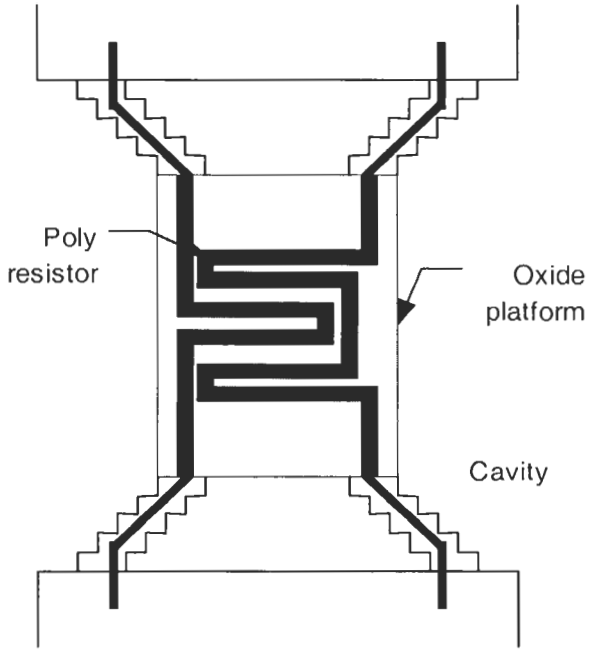


**Figure 2-6 Top view of the sensor made by Robinson and Parameswaran**

[Robinson and Parameswaran, 1992, redrawn by author with permission]

In 1993, Ping Kuo Weng and Jin-Shown Shie reported a highly sensitive micro-Pirani vacuum gauge fabricated by a semiconductor planar process shown in Figure 2-7 [17]. A square glass membrane was formed on (100) silicon substrate with a platinum (Pt) resistor in a serpentine shape as the heater. The membrane was suspended by its four leads extended to the corners of an etched V-groove cavity. The typical size of the cavity is 128μm×128μm, while the width and length of the leads were $\sqrt{2}\times 10\,\mu m$, $\sqrt{2}\times 16\,\mu m$, respectively. The sensor had a linear response of pressure from $8\times10^{-5}$torr (0.01Pa) to 6torr (800Pa) with constant-temperature operation.

An improvement was made by Shie et al in 1995 to extend the gauge's capability down to $10^{-7}$torr ($1.3\times10^{-5}$Pa) [18]. A partial dummy compensation and a constant-temperature circuit to stabilize the substrate temperature were credited for the high performance.

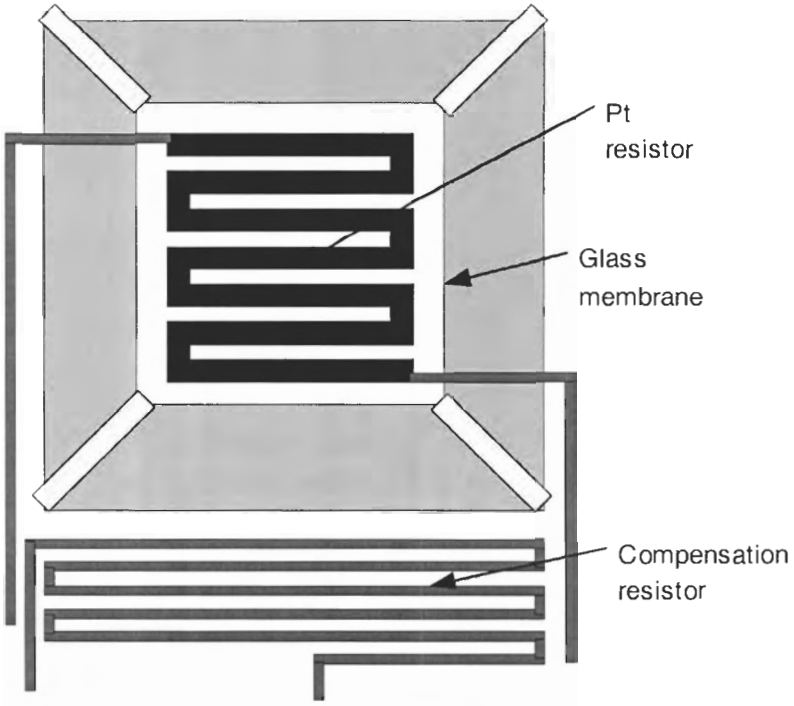


**Figure 2-7 Top view of the sensor made by Weng and Shie**

[Weng and Shie, 1993, redrawn by author with permission]

Oliver Paul and Henry Baltes presented a CMOS-compatible pressure sensor operating in the range of 100Pa–$10^6$Pa [19]. The heat sink was the silicon substrate, the heat source was a "metal 2" resistor in the shape as "a meandering, 3-μm wide line" sandwiched "between the intermetal dielectric and the passivation layers" on a round membrane [19] (Figure 2-8). It was used both as a heating resistor and a temperature sensor. The sacrificial layer was the lower metal layer ("metal 1") below the upper metal layer ("metal 2") and the intermetal dielectric. After removing the "metal 1" layer (nominal thickness of 0.65 μm), a thin gap was produced. The gap is delimited above by the membrane sandwich, and below by the silicon substrate covered by thermal and CVD $SiO_2$.

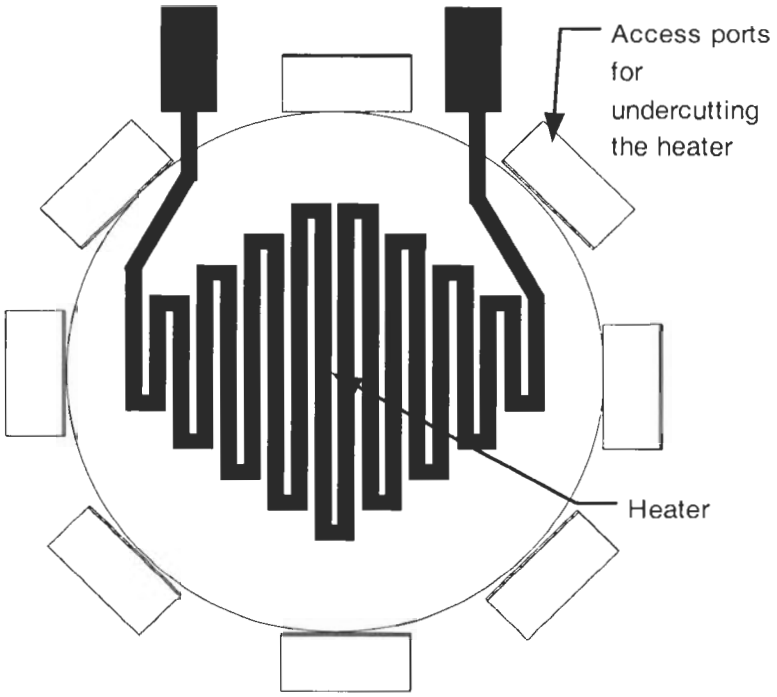


**Figure 2-8 Structure of the sensor made by Paul and Baltes**

[Paul and Baltes, 1995, redrawn by author with permission from Elsevier]

W. J. Alvesteffer et al introduced a miniaturized thin-film thermal vacuum sensor in 1995 [20]. The sensor employed a temperature-sensitive resistor deposited on a silicon nitride membrane in the center of a square silicon (Si) substrate. The resistor was formed by electron beam vapour deposition of a multilayer sheet with 30nm of Chromium (Cr) for adhesion and 200nm of Nickel (Ni). The high TCR (4650 ppm/°C) resistors were configured in the square wave pattern shown in Figure 2-9 (b). A silicon plate with a recessed region was put about 5$\mu$m above the membrane and served as a lid and heat sink for the heater. The inverted-box geometry showed in Figure 2-9 (a) allowed gas flow above and below the membrane. The compensating resistor was deposited directly on the silicon substrate and had approximately three times the resistance of the heater. The output was linear from $1\times10^{-4}$torr (0.013Pa) to 1torr (133Pa), and then monotonically increased to beyond 760torr (101kPa).

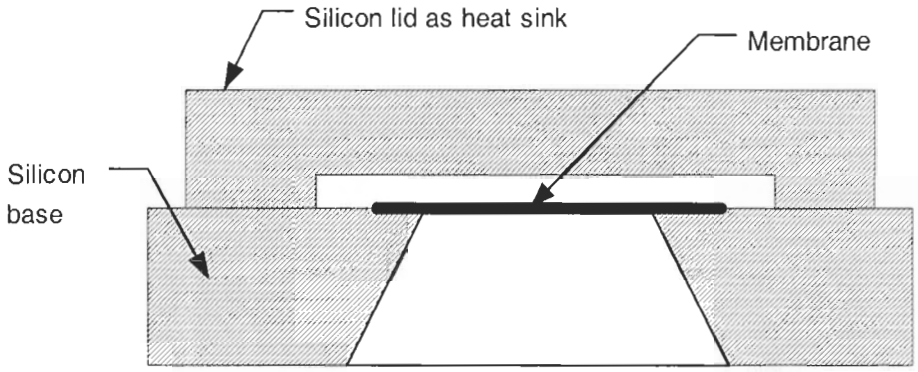


**(a) Cross section view of the sensor**

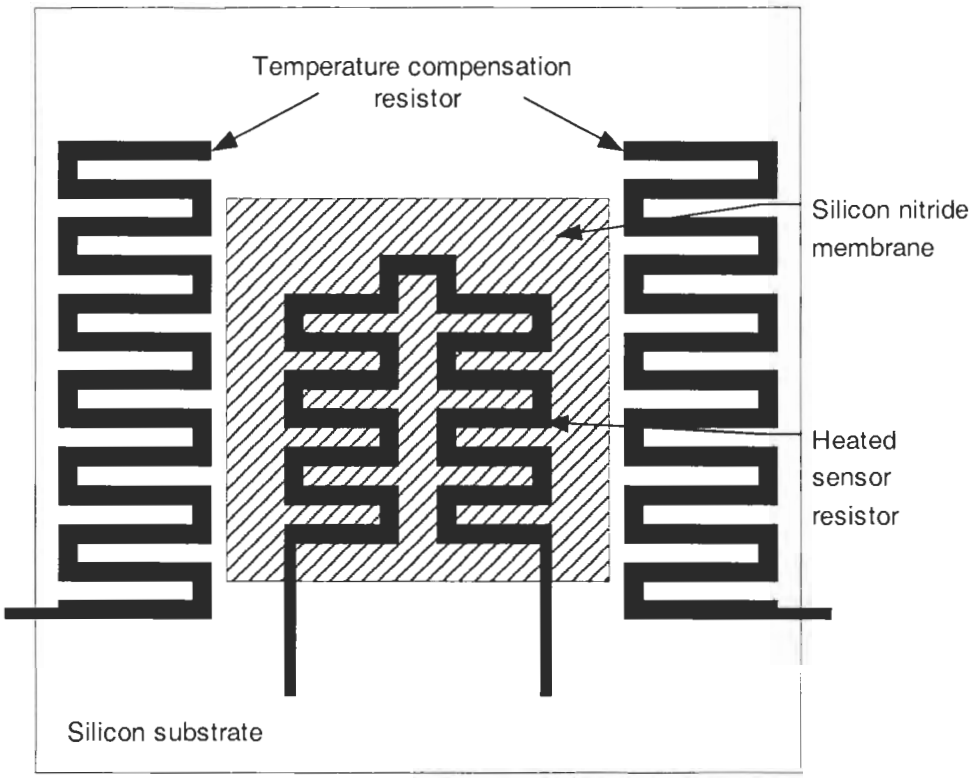


**(b) Top view of the sensor**

**Figure 2-9 Sensor made by Alvesteffer**

[Alvesteffer, 1995, redrawn by author with permission]

Erno H. Klaassen and G.T.A. Kovacs presented a vacuum sensor with an on-chip control system to maintain a constant temperature difference between the sensor and the substrate [12].

The prototype vacuum sensor could measure pressure from 0.8Pa to approximately 920kPa. The sensor was fabricated using post-processing methods on an unmodified foundry CMOS process. Figure 2-10 gives a top view of the sensor. The sensing structure was a small circuit suspended over a cavity etched in the (100) silicon substrate. A PMOS transistor was used as the heater and a diode-connected bipolar transistor was used as the temperature sensor. "The two advantages of using an MOS transistor rather than a polysilicon or diffused resistor were that the on-chip amplifier did not require an output buffer, and that the current through the MOS transistor can be modulated while the drain-source voltage across it was maintained constant. The power dissipated in the heater is then directly proportional to the source-drain current, which could be used as the output of the sensor system [12]. "

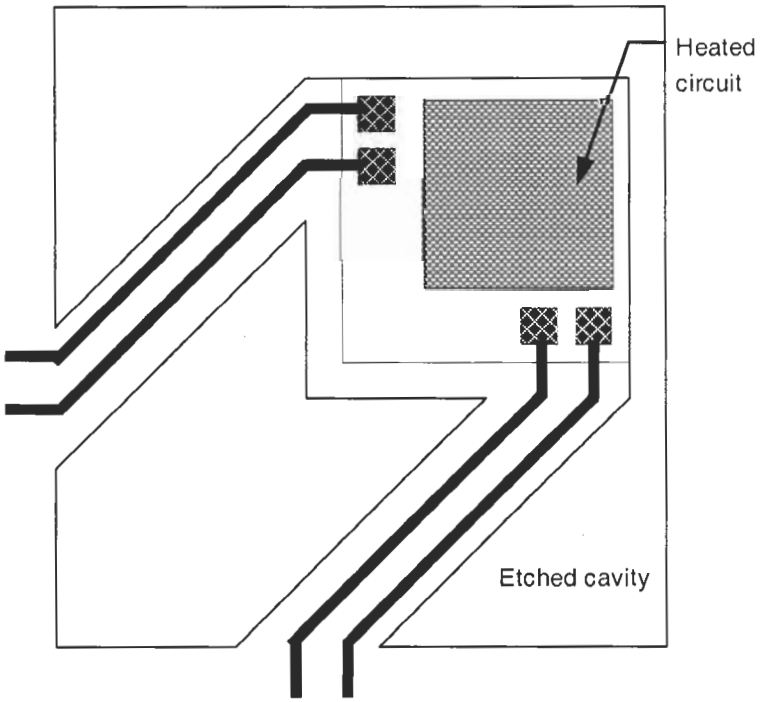


**Figure 2-10 Top view of the sensor made by Klaassen and Kovacs**

[Klaassen and Kovacs, 1997, redrawn by author with permission from Elsevier]

The thermal microsensor presented by O.M.Grudin in 1997 used alternating current (AC) heating for gas-pressure measurements [21]. The resistor is a serpentine 0.1μm-thick Ni film, a

0.03μm-thick Titanium (Ti) is deposited beneath it for adhesion. A floating LPCVD silicon nitride membrane was manufactured under the resistors. This is one of a few researches that use AC power to heat up the resistor.

Bruce C.S. Chou et al used a crucial freeze-drying step to avoid stiction and made a device with 300nm gap in 1999 [3, 34]. It is well known that any surface-micromachined suspended structure released by wet sacrificial etching can be pulled down to the substrate and stuck there. Bushing structures combined with the t-butyl alcohol freeze-drying method prevented this problem.

In Figure 2-11, the floating membrane had an active area of $50\times50\mu m^2$ and was supported by four kink-shaped leads that were 80μm long and 10μm wide. Platinum resistors (TCR of 0.28%/°C) were used for the heater and dummy resistors. Polysilicon was the sacrificial layer to form the small gap. Pressure up to 7 bars (700kPa) is measured linearly with nitrogen. Better performance could be obtained with a large area and a more sensitive readout circuit.

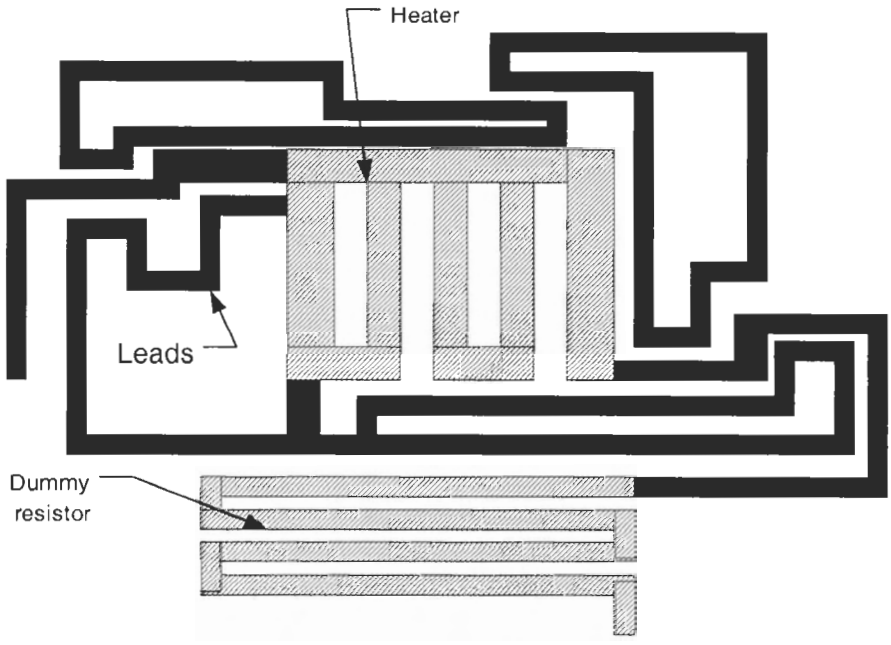


**Figure 2-11 Structural view of the sensor made by Chou, etc**

[Chou and Shie, 1999, © Sensors and Materials, redrawn by author by permission]

In a paper published in 2000, Bedo et al compared two micro vacuum sensors: a planar structure and a sandwich structure [22]. Both sensors consisted of a heating element and a sensing probe made by Pt thin-film resistors on a thin silicon nitride membrane floating over a 660μm silicon substrate (Figure 2-12). Both DC measurements and AC modulation techniques were tried. Only the planar structure is described here because the two are similar and the planar one is the one of interest. The planar structure is easier to produce and costs lower. The sensor structures were made by lift-off technique in a nitride membrane. The distance between the heater and probe was 210μm [22].

Under constant temperature mode, pressure measurements over a range of 30μbar (3Pa) to 100mbar (10kPa) were obtained with nitrogen. Temperature modulation could enlarge the range; improve the sensitivity and the response time. Combining all the three signals, the power amplitude, the probe amplitude and the probe phase, a measurement range of 10μbar (1Pa) to 1 bar (100kPa) was achieved for both structures.

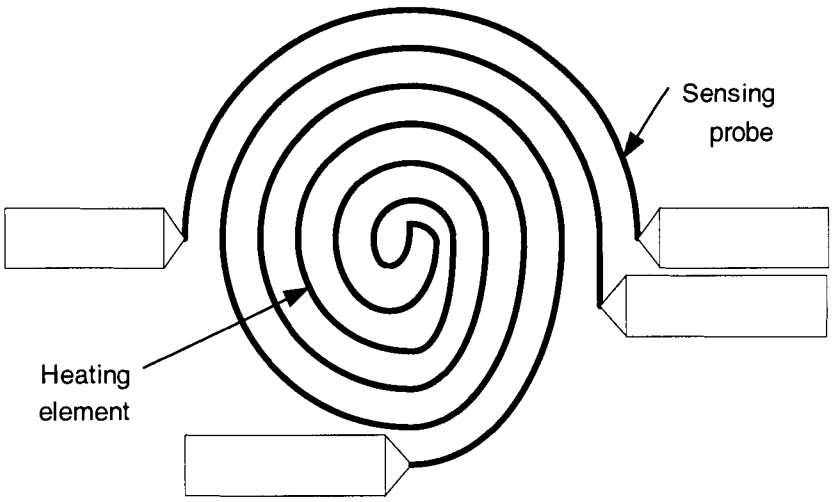


**Figure 2-12 Planar sensor fabricated by Bedo**

[Bedo, 2000, redrawn by author with permission from Elsevier]

In 2001, T. M. Berlicki proposed a unique approach to reduce the heat transfer from the substrate [23]. An additional heating element was incorporated to lower the temperature gradient

along the substrate.

The sensor consisted of two similar plates made of glass foil arranged as in Figure 2-13. Plate 1 was the sensing part and consisted of a heating resistor and a thermopile. The resistor was made of NiCr, and the thermopiles were made of Ge(Au)-NiCu, all deposited by magnetron sputtering. Plate 2 was added to improve the sensitivity and extend measurement range by reducing the heat loss through the radiation and thermal conduction of the substrate. Plate 2 also contained a heating resistor and a thermopile. The edge of plate 2 was put on the plate 1 with the heating resistor adjoined the plate 1 below the warm tips of thermocouples. An increase in sensitivity and extension of measurement range from the side of lower pressures was achieved. The measurement range of the sensor was $2\times10^{-3}$Pa to $10^{3}$Pa.

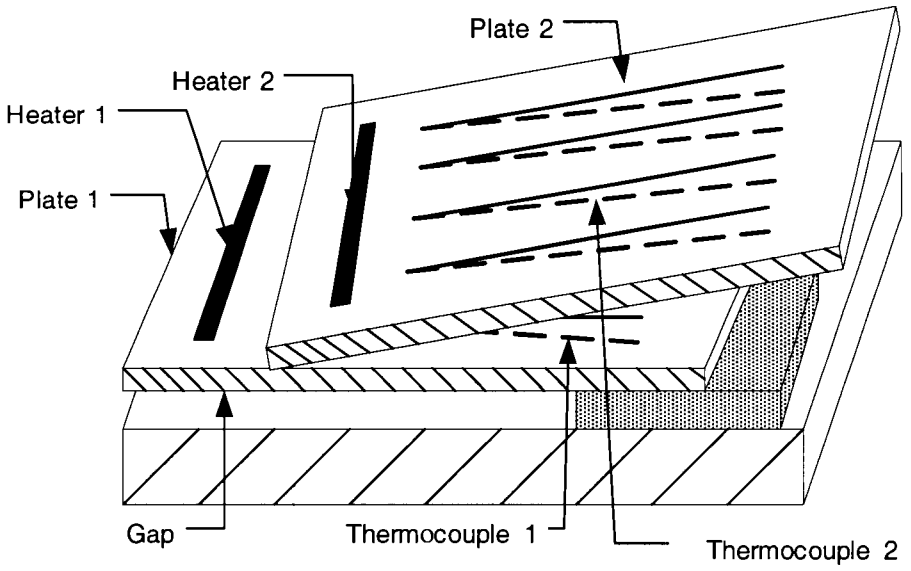


**Figure 2-13 Sensor made by Berlicki**

[Berlicki, 2001, redrawn by author with permission from Elsevier]

R. Puers reported an extremely miniaturized sensor fabricated by focused ion beam (FIB) rapid prototyping in 2002 [4]. The smallest one only had a $10\mu m\times1\mu m$ active area. The heater was a suspended tungsten (W) bridge. The air gap between the bridge and the substrate was made by the FIB technique as 400nm. FIB is good for prototyping, but is time consuming and costly,

thus not suitable for batch manufacturing.

Besides pressure measurements, monitoring the thermal conductivity of gases can be used to measure many other properties of the ambient atmosphere, such as gas type sensor [38], flow sensors [11, 24, 39] etc.

The sensors and their important properties that are discussed above are summarized in Table 2-1.

**Table 2-1 Summary of Related Work**

| No | Researcher | Year | Heater | Structure | Gap (μm) | Oper mode | Pressure (Pa) | Ref |
|---|---|---|---|---|---|---|---|---|
| 1 | Pirani | 1906 | Metal | wire | | | 100m-100k | 2/7 |
| 2 | Herwaarden | 1985/ 1988 | Silicon | Heater and thermopile | 120~ 250 | CP | 1m-1k | 13/36 |
| 3 | Higashi | 1988 | NiFe | Microbridge resistor | 2 | CT | 100-1M | 1 |
| 4 | Mastrangelo | 1991 | Poly | Microbridge resistor | 25 | CT | 10-10k | 15 |
| 5 | Robinson | 1992 | Poly | Meandering resistor in a platform | 50 | CP | 1.3-13 | 16 |
| 6 | Weng | 1993 | Pt | Serpentine Pt resistor in a square glass membrane | N/A | CT | $1.3\times10^{-5}$- 800 | 17 |
| 7 | Paul | 1995 | Metal 2 | Metal 2 resistor Metal 1 sacrificial layer | 0.65 | CP | 100-1M | 19 |
| 8 | Alvesteffer | 1995 | Ni | Serpentine Ni resistor in silicon nitride membrane | A few | CT | 0.01-133 | 20 |
| 9 | Klaassen | 1997 | Transistor | Transistor as heater diode as temp sensor | N/A | CT | 0.8-920k | 12 |
| 10 | Grudin | 1997 | Ni | Serpentine Ni resistor in silicon nitride membrane | 300 | AC heating | atmospheric pressure | 21 |
| 11 | Chou | 1999 | Pt | Pt resistor and Poly as sacrificial layer | 0.3 | CP | 0.13-700k | 3/ 34 |
| 12 | Bedo | 2000 | Pt | N/A | N/A | DC/AC heating | 1-100k | 22 |
| 13 | Berlicki | 2001 | NiCr | Thermopile GeAu-NiCu | N/A | CT | 0.002-1k | 23 |
| 14 | Puers | 2002 | W | FIB | 0.4 | CP, bridge | atmospheric pressure | 4 |
| 15 | Our sensor | 2000 | Poly | Poly resistor | 0.05 | CP, bridge | Up to 800k | |

Poly-polysilicon
CT-constant temperature mode
CP-constant power mode

# CHAPTER 3 DESIGN

## 3.1 Design Considerations

Design needs to consider the technology, fabrication, testing and cost of the sensor. Sensor materials and structures are the primary factors considered in the work.

The sensor does not require advanced IC technology, fabrication processes are constrained to the 3μm technology available in the cleanroom at Simon Fraser University (SFU). The equipment and chemicals that are available in the cleanroom would be considered. The test system includes the pressure system and the electrical test system.

It is important to choose proper materials for the heater, the sacrificial layer, the heat sink and the bonding pad. One of the most important process steps is removing a sacrificial layer and releasing the heater structure to create a gap between the heater and the heat sink. The distance of the gap determines the pressure measurement range and is the most critical dimension of the sensor. The selection of material for the heater and the sacrificial layer is discussed in detail in this chapter, as well as the layout and dimensions of the sensor structures that affect the sensor performance and fabrication yield.

### 3.1.1 Heater

#### 3.1.1.1 Heater Structure

Two methods are available for designing the heater and its temperature-sensing element. The first method is to fabricate the heater and sensing element separately. The heater can be implemented by a resistor or transistor, while the temperature sensor can be a resistance temperature detector (RTD), thermocouple, diode or transistor. Table 3-1 gives the thermal

sensing principles and the common implementation examples in micromachining.

**Table 3-1 Thermal sensing principles and the associated implementation examples** [2, 11]

| Principle | Micromachining implementation | Measurement |
|---|---|---|
| T→R | • RTD –metal like Pt, W, Ni etc and Silicon, Polysilicon | • Temperature/difference<br>• Heating power |
| T→V | • Thermocouples –Polysilicon/ metal; p-Polysilicon/n-Polysilicon | • Temperature/difference |
| T→Electronics | • Transistors/Diodes | • Temperature/difference |

The second approach is to combine the heater and temperature sensor as one integrated element. We adopt the second one for simplicity and design the heater in resistive format (for simplicity, we call the integrated element 'heater' hereafter unless there is a need to clarify). The sensor works under a constant power (CP) mode. The constant electrical power raises the heater to a certain temperature by self-heating. The temperature changes with pressure and is measured by the resistance.

### 3.1.1.2 Heater Materials

The selection of heater materials depends on the thermal and electrical properties of the material, as well as the cost, availability and compatibility with the fabrication process.

The important thermal and electrical properties that affect the performance of a thermal sensor are electrical resistivity $\rho$, the temperature coefficient of resistance (TCR) and the thermal conductivity $k$ of the sensor materials. Materials with higher $\rho$ (compare to aluminium and gold), higher TCR and lower $k$ are preferred for our design.

Table 3-2 summarizes the properties of materials commonly used in micromachining.

**Table 3-2 Physical properties of common semiconductor materials** [40]

| Material | Resistivity $\rho$ $\mu\Omega$ cm@20°C | TCR @0-100°C ($K^{-1}$) | Thermal conductivity $k$ @0-100°C ( W/ m K ) |
|---|---|---|---|
| Al | 2.67 | 0.0045 | 237 |
| Au | 2.2 | 0.0040 | 318 |
| Cr | 13.2 | 0.00214 | 94 |
| Mo | 5.7 | 0.00435 | 138 |
| Ni | 6.9 | 0.0068 | 90.9 |
| Si | $23 \times 10^{10}$ | - | 80-150 |
| $SiO_2$ | $10^{14}$ @25C | 0.0005 | 1.2-1.4 |
| Pt | 10.58 | 0.00392 | 71.6 |
| Ti | 54 | 0.0038 | 21.9 |
| W | 5.4 | 0.0048 | 173 |

#### *3.1.1.2.1 Resistivity*

The resistivity and size of the resistors determines the final resistance, and consequently, the maximum power supply for the resistor. Higher electrical resistivity is wanted for good resolution. Refractory metals present relatively higher electrical resistivity. Thermal sensors made out of Pt, W, and Ni resistors were reported [4, 17, 19, 20-22, 34]. However, silicon or polysilicon resistors possess even higher electrical resistance that is easily altered by doping concentration. The electrical resistivity of doped polysilicon is always higher than that of the single-crystal silicon for the same impurity concentration level [29]. Therefore, doped polysilicon resistors can achieve highest resistance value.

#### *3.1.1.2.2 Temperature Coefficient of Resistance*

The temperature coefficient of resistance (TCR) of a resistor is used to translate its resistance change to the average temperature change. It affects sensitivity of the sensor.

The TCR of a material is defined as the resistance change per unit resistance per degree temperature rise of the material under test and is given by

$$\alpha = \frac{\Delta R / R}{\Delta T}, \tag{3.1}$$

where $\alpha$ is the TCR value as per degree Celsius or Kelvin, $\Delta R$ is the change in resistance of the

material, $R$ is the nominal resistance before the temperature change, and $\Delta T$ is the temperature change. The TCR could be positive (resistance becomes larger with rising temperature) or negative.

Metals generally have negative TCRs. Nickel (Ni) has the highest TCR at 0.0068/°C, compared with Gold (Au), Tungsten (W), Platinum (Pt), Titanium (Ti), and Molybdenum (Mo). The TCR of silicon is moderately positive ([0 -0.002]/°C) throughout most of its doping range and fairly constant over a wide temperature range [28].

#### *3.1.1.2.3 Thermal Conductivity*

As discussed in Section 2.2.2, heat losses of the heater to its environment are primarily through solid conduction and air conduction. Solid thermal conduction is through the direct contact between the heater and the sink, and the heat loss is pressure-independent. Air thermal conduction is through the air gap between the heater and the sink, and the heat loss changes with pressure. For our design, the latter is most significant and is the main measurement feature of our sensor. For higher sensitivity of the sensor, more heat has to be conducted through the air gap, which requires the heater material has smaller $k$.

Gold (Au) has high thermal conductivity and low electrical resistivity, resulting in a low sensitivity for the sensor. Compared with Au, Ni has lower thermal conductivity, higher TCR and resistivity. Sensors made with Ni would exhibit higher sensitivity and more precise temperature reading than that made of Au. It would allow higher input power supply too.

Compared with Ni, Pt has a lower TCR (about twice as low as Ni), lower $k$ and higher $\rho$; Tungsten (W) has higher $k$, lower $\rho$ and lower TCR. Chromium (Cr) has the lowest TCR in the group but higher resistivity (about two times) than Ni and similar $k$. Sensors made with Cr would be less sensitive than that made by Ni but with twice higher $V_{in}$ (measurement resolution).

#### *3.1.1.2.4 Standard IC Process Compatibility*

Platinum (Pt) and Au are not standard microelectronic materials, and are usually deposited in post-process [35]. The presents of Pt and Au in the structure will result limitations on subsequent processes steps and structure optimisation.

It was reported that Au and Cr are resistant to EDP while W is not etched in 44% KOH at 70°C [35]. It was also reported that Cr and Au are resistant to KOH/water (1:2 by weight) at 75°C [13]. Because Ni, Pt and W have low thermal conductivity and relatively high TCR, they are potentially good temperature sensors. It is the reason why they are used in the previous work. In our design, we choose polysilicon as the heater material because of the following discussions.

### 3.1.1.3 Properties of Polysilicon

Polysilicon is widely used in semiconductor industry, in applications ranging from simple resistors, gates for MOS transistors, thin-film transistors (TFT), DRAM cell plates, and trench fills, as well as in emitters in bipolar transistors and conductors for interconnects [35]. It also acts as the central structural/mechanical material in surface micromachining [26]. It is readily available, easily deposited and compatible with the standard IC process. The material properties are easily adjusted by the changing of deposition details, such as temperature, dopant and pressure and are significantly different between the thin films and the bulk materials [33].

Using polysilicon as the heater material, the design and fabrication processes is greatly simplified and easily optimised. Also, the processing can be easily integrated into standard CMOS commercial foundries.

#### *3.1.1.3.1 Electrical*

"Polysilicon consists of aggregates of single-crystal silicon grains of various orientations and sizes, bounded by grain boundaries. Typical grain size ranges from 10 to 500nm and the grain boundary is only a few lattice spacing [29]."

The electrical properties of polysilicon are similar to bulk silicon for sensing applications [35]. They are primarily governed by the dopant type and concentration level, the final grain size after all thermal treatments, and the nature of the grain-grain boundary interface. For large grain sizes and small boundary effects, the resistivity and TCR are close to the properties of single-crystal silicon with the same doping concentration. On the other hand, films with smaller grain size, lighter doping, larger boundaries, and/or higher trap densities can be expected to have resistivities many orders of magnitude higher than those of the moderately doped silicon [28].

The TCR of a polysilicon layer over a specified temperature range is affected by the doping concentration, grain size and trap state [27, 29]. The TCR for doped polysilicon exhibits the following features [29]:

1) The TCR can be selected + or - through selective doping.

2) The resistance change with temperature is not linear; there is a limited temperature range over which TCR can be assumed constant. And the temperature dependence increases with decreasing doping concentration.

3) A unique TCR value corresponds to a unique doping level, thus the resistivity.

#### *3.1.1.3.2 Thermal Conductivity*

The thermal conductivities for polysilicon thin films differ substantially from those of bulk silicon and are often process dependent [30]. Thermal conductivities of doped polysilicon layers are significantly lower than those of single-crystal silicon layers due to phonon scattering on the grain boundaries [30]. At room temperature the thermal conductivity of a polysilicon layer is reduced by a factor of approximately two compared to a single-crystal silicon layer with a similar dopant concentration [30].

The following are some observances of the thermal conductivities of a doped polysilicon thin film [30].

1) For a comparable doping concentration, a doped polysilicon layer has a thermal conductivity value less than a single-crystal layer at all temperatures.

2) A doped polysilicon layer exhibits higher thermal conductivity values at all temperatures compared to an undoped layer; for a given dopant type, the sample with higher concentration has lower thermal conductivity values.

3) At the same dopant concentration, layers doped with phosphorus have higher thermal conductivity values than boron-doped layers.

4) Thermal conductivity values of doped polysilicon at room temperature range from 30W/m K to 60W/m K approximately.

#### *3.1.1.3.3 Process*

Polysilicon film can be etched by alkaline solutions like ethylene diamine/pyrocatechol (commonly known as EDP), Potassium Hydroxide (KOH) and other strong alkaline solutions such as cesium hydroxide (CsOH), sodium hydroxide (NaOH) and tetramethylammonium hydroxide (TMAH) [35]. A distinct advantage of EDP is its high etch selectivity with $SiO_2$, $Si_3N_4$ and metals like Au, Cr, Ag and Cu, which can be used conveniently as masking films because polysilicon is not resistant to EDP [35]. Another important property of the etchant is its effect on metal. Most of the etchants mentioned above attack interconnect layers, while EDP does not attack gold metallization [35]. Special passivation and isolation techniques are required using other etchants.

The etch rate for polysilicon in EDP is temperature-dependent, governed by the Arrhenius law [35]

$$R = R_0 e^{(-E_a/kT)} \tag{3.2}$$

where $R_0$ is a constant, and $E_a$ is the activation energy, both are determined experimentally; $k'$ is the Boltzmann's constant, and $T$ is the temperature in K.

#### *3.1.1.3.4 Stress in the Polysilicon Structural Layer*

Residual stress stays in nearly all films, due to mismatch in the thermal expansion coefficient, non-uniform plastic deformation, lattice mismatch, substitutional or interstitial impurities, and growth processes [26]. The stress will lead to film cracking, bulking, delamination, and void formation. Stress in polysilicon films varies significantly with deposition temperature and pressure. It restricts the size of the freestanding structures, causes malfunctions of the thin-film structures. Control of film stress can be done in many ways like temperature treatments, structure design, and doping [26].

### 3.1.2 Heat Sink

The heat sink can be provided by the silicon substrate, or some metals. In most sensor designs, the silicon substrate is a natural choice.

### 3.1.3 Sacrificial Layer

The focus of the design is to make the gap between the heater and heat sink as small as possible, well below 1μm. The gap distance is determined by the sacrificial layer. A good sacrificial material with the following qualities like good film uniformity, high etch rate and good etch selectivity is desirable. Other considerations include ease of processing, availability and low cost. Photoresist, metal or oxide and other materials like low-temperature oxide (LTO) or Phosphosilicate glass (PSG) are all possible materials for the sacrificial layer [26]. For our design, $SiO_2$ is chosen as the sacrificial layer.

Silicon dioxide is an excellent electrical and thermal insulator. Thin-film $SiO_2$ is amorphous and has a lower density than silicon [35]. Its resistivity is high ($10^{15}$ Ω/m), and its thermal conductivity is low (1.4 W/m K). Because this film can be readily removed by buffered HF (BOE) without affecting the structural polysilicon, it is commonly used as a sacrificial layer [35].

Isotropic etching of $SiO_2$ is usually done in wet chemistry with diluted HF or BOE, and photoresist is commonly used as the masking material. If exposed aluminium is on the wafer, dihydroxyalcohol or glycerol may be added to slow the attack on the metal [35]. In our design, aluminium is used as the bonding pad, so glycerol is added to BOE to etch the $SiO_2$.

### 3.1.4 Bonding Pads

Bonding pads are made by aluminium and the connecting wire can be either aluminium alloy or gold, all is readily available. The difficulty of using Al is that it is not compliant with BOE, the etchant for $SiO_2$. Buffed HF (BOE), the most popular etchant for $SiO_2$, attacks Al (actually BOE is the one that is used to etch Al in the fabrication). Other metals are eliminated because of the process and cost issues. Actually in the beginning of the experiment, polysilicon was tried as the bonding pad and the conductive epoxy was used to glue the gold wire to the polysilicon bonding pad. This approach did not work because the resistance of the epoxy was always changing. The etchant of 30ml Glycerol mixed well with 50ml BOE was used to etch the $SiO_2$ and Al was used eventually.

The drawback of adding Glycerol to BOE is that the oxide etching becomes very slow and it takes hours to release the polysilicon resistor. To prevent the bonding pad being undercut and lifting off from the silicon substrate, the bonding pads are designed relatively large compared to the line width of the resistor. The maximum dimension of the bonding pad is $900\times900\mu m^2$. The line widths of the resistor are typically from $10\mu m$ to $50\mu m$, thus the resistor will be released with most of the bonding pad intact. The following is the observance of the releasing steps:

After 40 minutes in the etchant, two-third of the width of the polysilicon line was etched while Al bonding pad was intact; 60 minutes later, most of the line was released; after 70 minutes, the only part not released was the corner where two lines joined together; after 80mins, the line was totally released with sufficient oxide left to hold the bonding pad on the substrate.

### 3.1.5 Test Setup

There are two different operational modes in the test setup, the constant-power (CP) and constant-temperature (CT) modes. In the CP mode, a fixed amount of power is dissipated in the heater to put it at a certain temperature; as pressure changes, the heat losses of the heater through the ambient gas change accordingly, so does the temperature of the heater. By monitoring the temperature of the heater (from its resistance, for example), the ambient air pressure is known.

In the CT mode, the temperature of the heater is fixed; the power fed into the heater becomes a measure of pressure and is varied to compensate for the heat loss. A feedback loop monitors the temperature of the heater to maintain a constant temperature difference between the heater and the sink. This mode is more complicated than the CP mode.

The CP mode is chosen in our design because it is simple to implement with available equipment.

## 3.2 Design

As discussed above, n-doped polysilicon is chosen to construct the resistors because of its good electrical and thermal properties, its compatibility with standard IC processes, and the granular surface to build the gap. Silicon dioxide is used as the sacrificial layer and silicon substrate as the heat sink. Aluminium is used for the bonding pads.

Four experimental runs were fabricated and tested. The first two runs tested the feasibility of the concept and set up the design rules. In these two runs, released resistors (called heaters) with various shapes and sizes were fabricated. In the last two runs both heaters and unreleased resistors (called dummy resistors) were fabricated and connected in a Wheatstone bridge configuration to improve the sensor performance. The fabrication procedure for producing a released resistor and an unreleased resistor is described in the next section followed by discussion of the structure and layout design.

### 3.2.1 Process Design

The main considerations for process design are:

- Use minimum number of masks.

- Obtain good electrical and thermal isolation.

- Sacrificial etching for heater release.

- Use local facilities and standard IC technology.

The starting wafers are Si (100) wafers with the $SiO_2$-Poly- $SiO_2$ sandwiched layers (Figure 3-1 (a)). A 0.5$\mu$m oxide layer is thermally grown on the silicon substrate. On top of the thermal oxide layer, an n-doped and 0.55$\mu$m-thick polysilicon layer is deposited by low-pressure chemical vapour deposition (LPCVD). Another 0.5$\mu$m oxide layer is CVD deposited on top of the polysilicon layer. N-doped polysilicon is used to build the tiny resistors. The thermal oxide layer is the sacrificial layer, whose thickness determines that the maximum height for the gap between the heater and the heat sink is less than 0.5$\mu$m.

The etchant for polysilicon is EDP, for Al and CVD oxide is BOE. A mixture of 30ml Glycerol with 50ml BOE is used to etch the thermal oxide (sacrificial layer) without attacking Al.

At the beginning of the first fabrication run, experiments were conducted to determine the design rules and process procedures. Lines with different widths and lengths were designed and processed for different time intervals. For example, the lines were exposed for 10s, 20s and 30s, respectively, and then etched for 10s, 20s, and 30s, respectively. Dimensions were measured in each step to get the optimum line width and process time. The minimum line width that can be fabricated in this process is 6$\mu$m under the optimised exposure time of 10 seconds.

It only needs two masks to produce a released resistor. Figure 3-1 illustrates the process flow. To fabricate a released resistor and an unreleased one on the same chip takes three masks. The three-mask process flow is given in Figure 3-2.

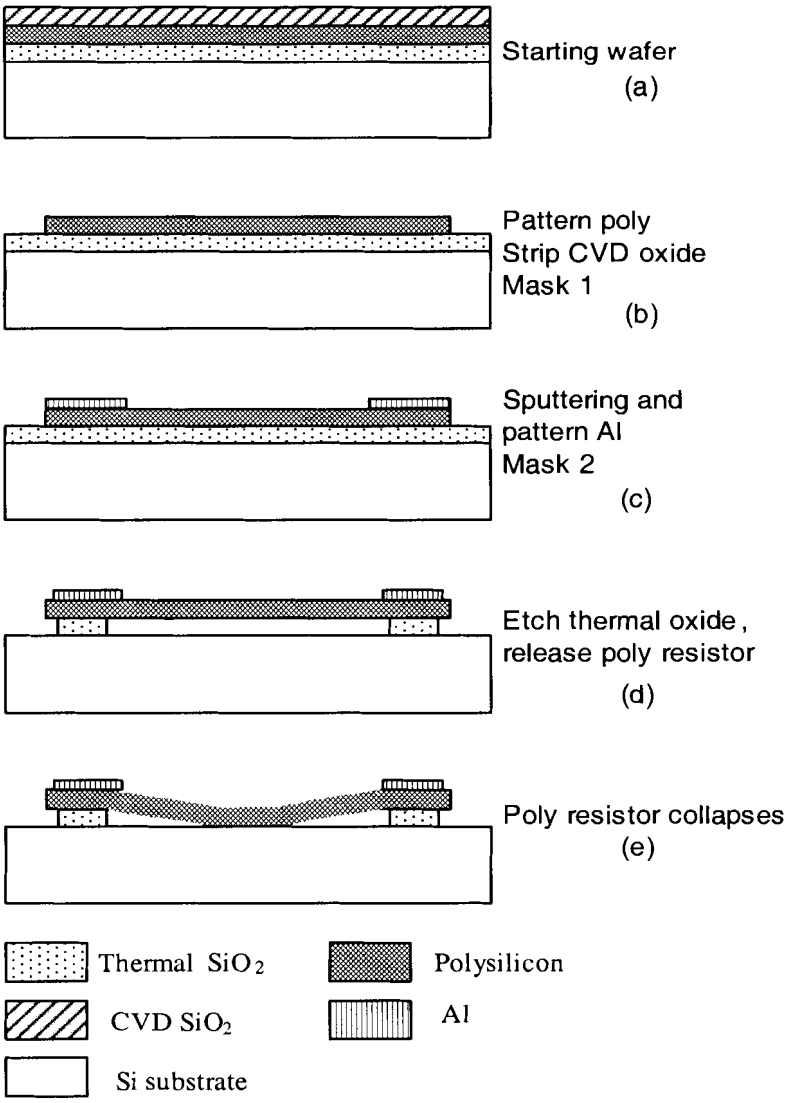


**Figure 3-1 Fabrication procedure for a 2-mask process**

In the two-mask process procedure (Figure 3-1), the first step (b) uses Mask 1 to define polysilicon layer with CVD oxide layer as the etch mask; then the CVD oxide is removed. In step (c), Al thin film is sputtered on the polysilicon layer, and then Mask 2 is used to define Al as the bonding pad above the polysilicon bonding pad with photoresist as the etch mask. Step (d) releases polysilicon resistors by sacrificially etching the thermal oxide layer. This step takes a long time. In the last step (e), the polysilicon resistor collapses to the silicon substrate and sticks there because of the surface tension and stiction effect.

Amongst many aspects in the process, the last two steps (d) and (e), the sacrificial etching and structure collapse, are of particularly important.

#### 3.2.1.1 Sacrificial Etching

Sacrificial etching is used to produce suspended or floating sensor structures in surface micromachining. First, the structural material has to be deposited on a solid surface that is called the sacrificial layer. The sacrificial layer serves as a spacer and a temporary anchor surface for the deposition [35]. After forming the needed sensor structures, the sacrificial layer is completely removed to free the structure.

The challenge in freeing microstructures by undercutting is the etch selectivity ratio for the spacer layer and the microstructure [26, 35]. The spacer etch rate must be much faster than the attack on the structural element. This type of complete undercutting only can be achieved by wet etching. Etching narrow gaps and releasing wide areas with BOE can take hours [26].

#### 3.2.1.2 Stiction

An important limitation of the above releasing step is "that large-area structures tend to deflect through stress gradients or surface tension induced by trapped liquids and attach to the substrate layer during the final rinsing and drying step, a stiction phenomenon that may be related to hydrogen bonding or residual contamination [26]".

After the structure is totally released, a long and thorough rinse in deionized water is followed. As the water dries, the surface tension of the rinse water pulls the delicate microstructure to the substrate and a combination of forces firmly pin it there. Once the structure touches the substrate, it is impossible to separate them without damaging the microstructure. This is the situation that all the previous work tried to avoid. In contrary, we took advantage of the collapse and the non-smooth surface of polysilicon to produce tiny air gaps in the order of tens of nanometer inexpensively.

In addition, extended rinsing causes a native oxide to grow on the surfaces of the polysilicon structure. Such a passivation layer is desirable because it provides electrical isolation between the polysilicon and the silicon substrate. The passivation layer can also be formed easily by a short dip in 30% $H_2O_2$ [26].

#### 3.2.1.3 Three-Mask Fabrication Procedure

Unreleased resistors called dummy resistors were added to the design in the third and fourth runs to configure a Wheatstone bridge with the released resistors. The feature of the process is to reserve both oxide layers on the two sides of unreleased polysilicon resistors. Aluminium is used as the etch mask to protect them from being removed. The CVD oxide on top of the dummy resistors provides the electrical isolation between the Al protective plane and the underneath polysilicon resistors. The process flow chart for the three-mask fabrication procedure is illustrated in Figure 3-2.

In the three-mask procedure, after defining polysilicon layer in step (b) with mask 1, CVD oxide is patterned in step (c) with mask 2, only the oxide on top of the released resistors is removed. Mask 3 defined the Al bonding pad and the protective plane in step (d). Steps (e) and (f) are same with the two-mask procedure. Detailed process steps can be found in Appendix B.

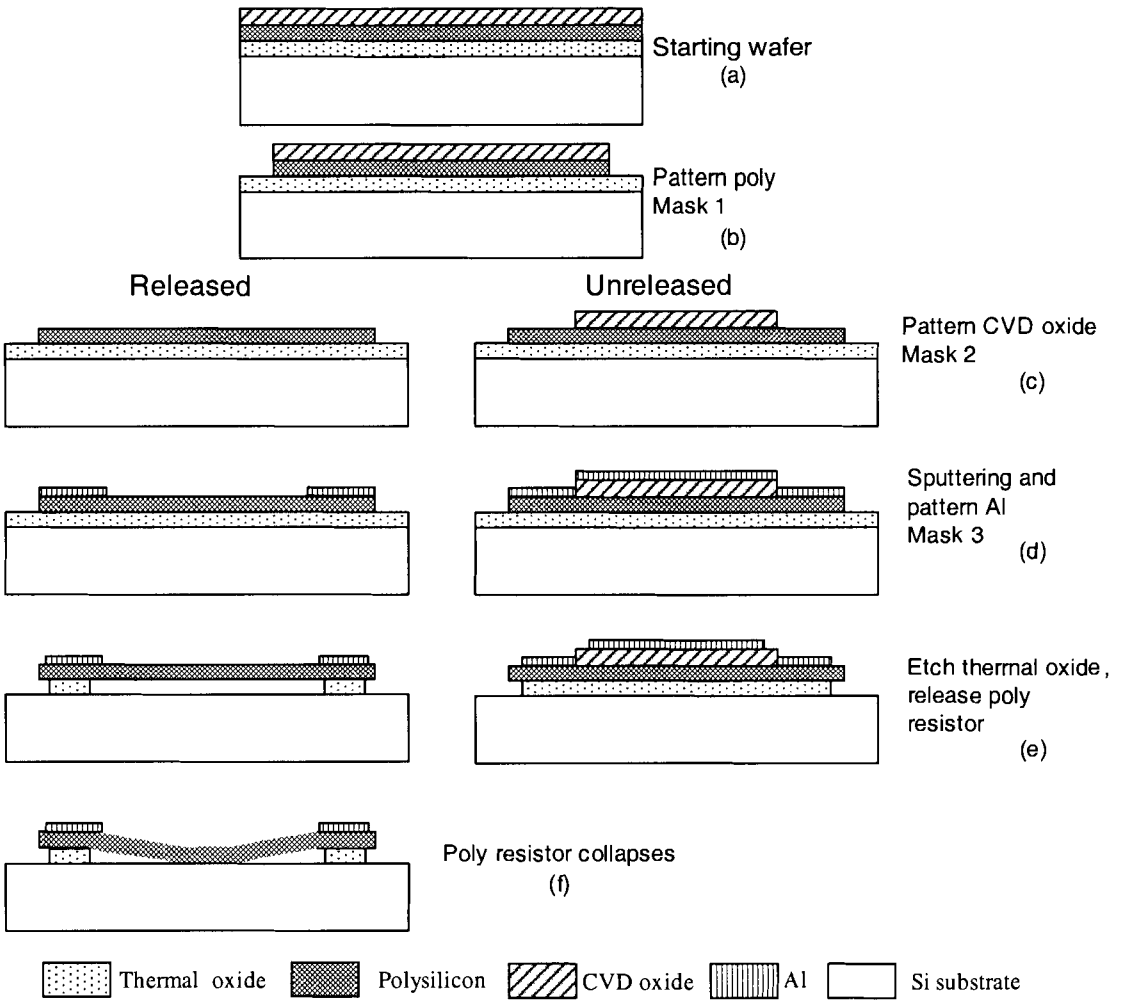


**Figure 3-2 Three-mask fabrication procedure producing released and unreleased structures**

### 3.2.2 Structural Design and Mask Layout

Cadence Mitel 15 is the design tool used for the layout.

#### 3.2.2.1 Resistor Structures

Various structures like straight beams and U-shape cantilevers shown in Figure 3-4 (a) and (b) were tried out for the resistors; the length and width of the lines were varied to choose the proper dimensions.

In Figure 3-4 (a), $l$ and $w$ represent the length and width of the beam, respectively; in (b), the arms are used to facilitate the collapse.

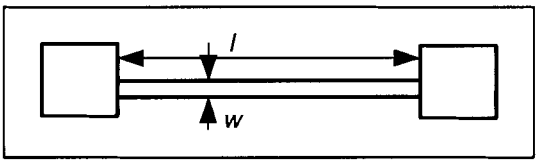


**(a) Top view of a straight beam resistor**

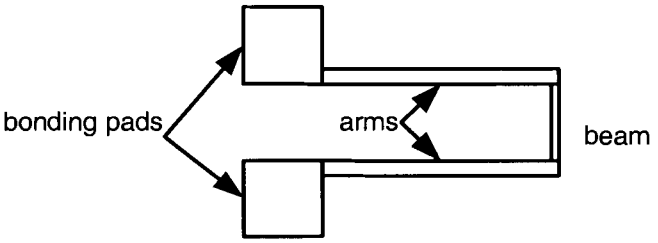


**(b) Top view of a U-shape cantilever resistor**

**Figure 3-3 Different structures for the resistors**

A number of factors are important in the design: the sensitivity of the sensor primarily depends on the temperature difference between the heater and the sink (substrate). If the substrate temperature is used as the reference temperature and is kept constant, the sensitivity is solely determined by the heater's temperature, which in turn is determined by the heating power that is dissipated in it and the heat loss to the environment.

Higher heating power gives better sensor resolution. The power is determined directly by the bias current of the device that is limited by the maximum allowable current density and the cross-sectional area of the beam.

The heat loss consists of two parts. Besides the pressure-dependent heat transport through the gap, there is also a pressure-independent heat loss to the substrate by conduction through the solid contact. This is considered as a 'parasitic' heat loss, concealing the wanted heat transport through the gap. The goal of the design is to enlarge the gas contact area for higher sensitivity of the sensor.

Figure 3-4 shows part of the various sensor structures used in the first and second runs. The widths of the lines are 10μm, 20μm or 50μm; the lengths are from 100μm, 200μm to

2000μm or 3000μm and the resistances vary from 200Ω to 2kΩ.

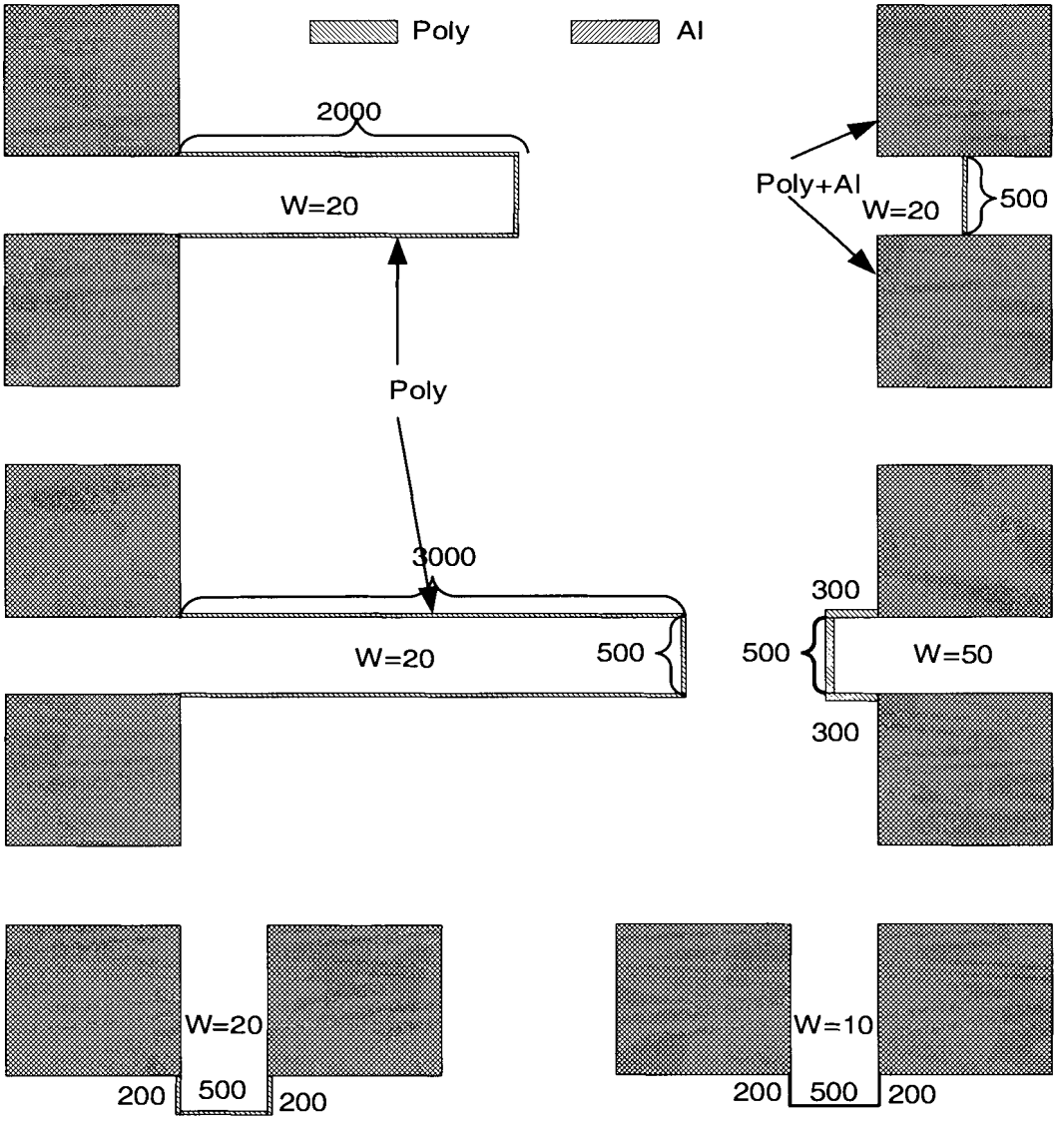


**Figure 3-4 Designs of the first and second runs**

### 3.2.2.2 The Wheatstone Bridge

A Wheatstone bridge can detect small resistance changes and even out the common mode errors such as the ambient temperature drift (improve resolution and reduce noise). In the third and fourth runs, four identical resistors were fabricated on a single chip. Two of the resistors are released, i.e., the $SiO_2$ layer underneath the beams is removed. As mentioned before, the resistors are used as the heat sources and temperature sensors, but called 'heaters' for simplicity. The other

two resistors are dummy resistors with unreleased beams - the $SiO_2$ layer underneath is intact. The four resistors are separated in the chip and can be tested individually or connected as a Wheatstone bridge externally.

Figure 3-5 illustrates the design structure in the third run. The patterns in the third run are all same, just the width and length of the resistor are different. Line widths are 10μm, 20μm and 50μm, the lengths are 250μm, 750μm to 900μm. The resistances are from 300Ω to 1kΩ.

The fourth run is a multi-finger design. There are multiple beams at the end of the arms. These beams are called 'fingers' to distinguish them from that in the 'one-beam' design. The goal is to increase the air conduction area by increasing the number of released beams. There are eight different design patterns, with different numbers of fingers and different distances between the fingers. The line widths are 6μm, 8μm and 10μm and the distances between the fingers are 2μm, 4μm and 5μm, respectively. The lengths of the fingers are 150μm, 200μm or 250μm, respectively. The original design files are listed in Appendix A.

Figure 3-6 illustrates pattern 3 of the fourth design run. There are four fingers in the end of the arms. Each finger is 6μm wide and 150μm long. The space between each finger is 5μm. The arms are 50μm wide and 300μm long.

Figure 3-7 gives pattern 8 of the fourth design run. There is only one finger in the end of the arms. The finger is 10μm wide and 250μm long.

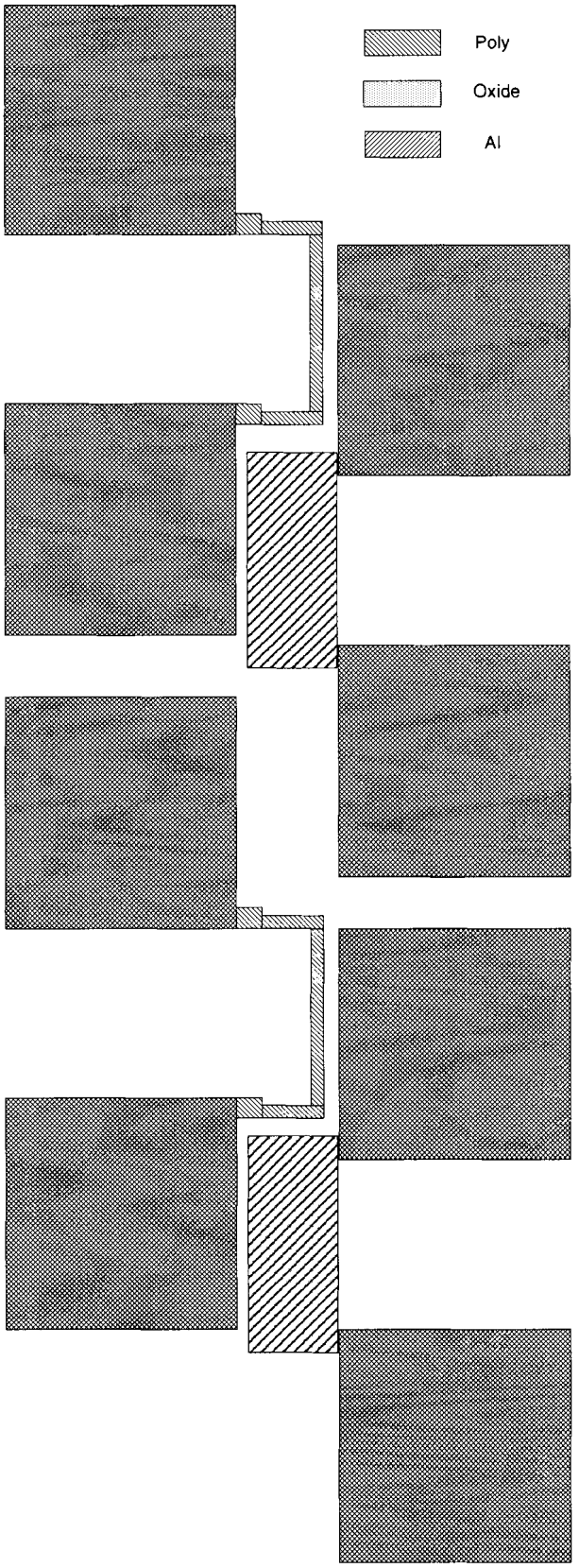


**Figure 3-5 Structures of the third design run**

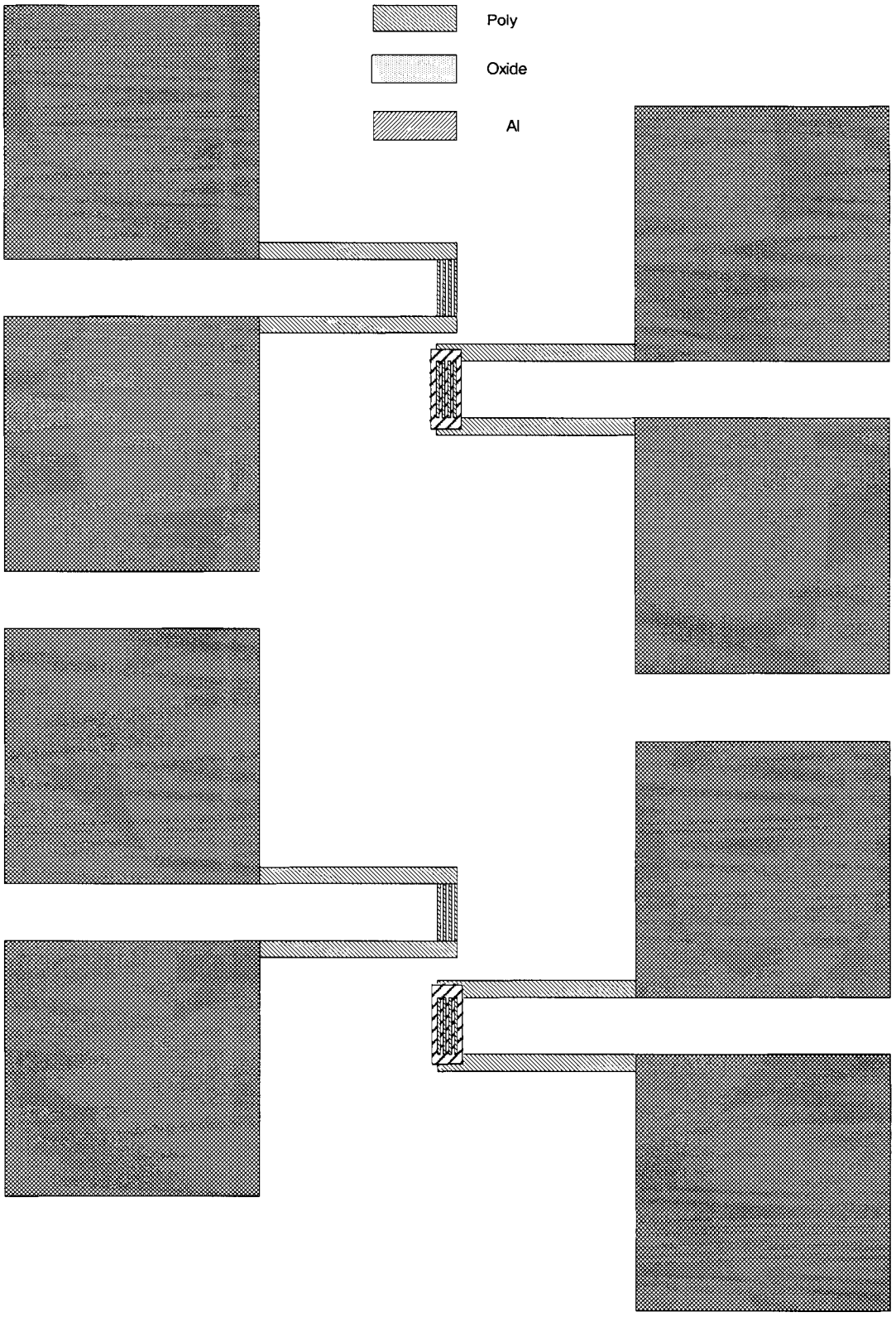


**Figure 3-6 Structures of pattern 3 in the fourth run**

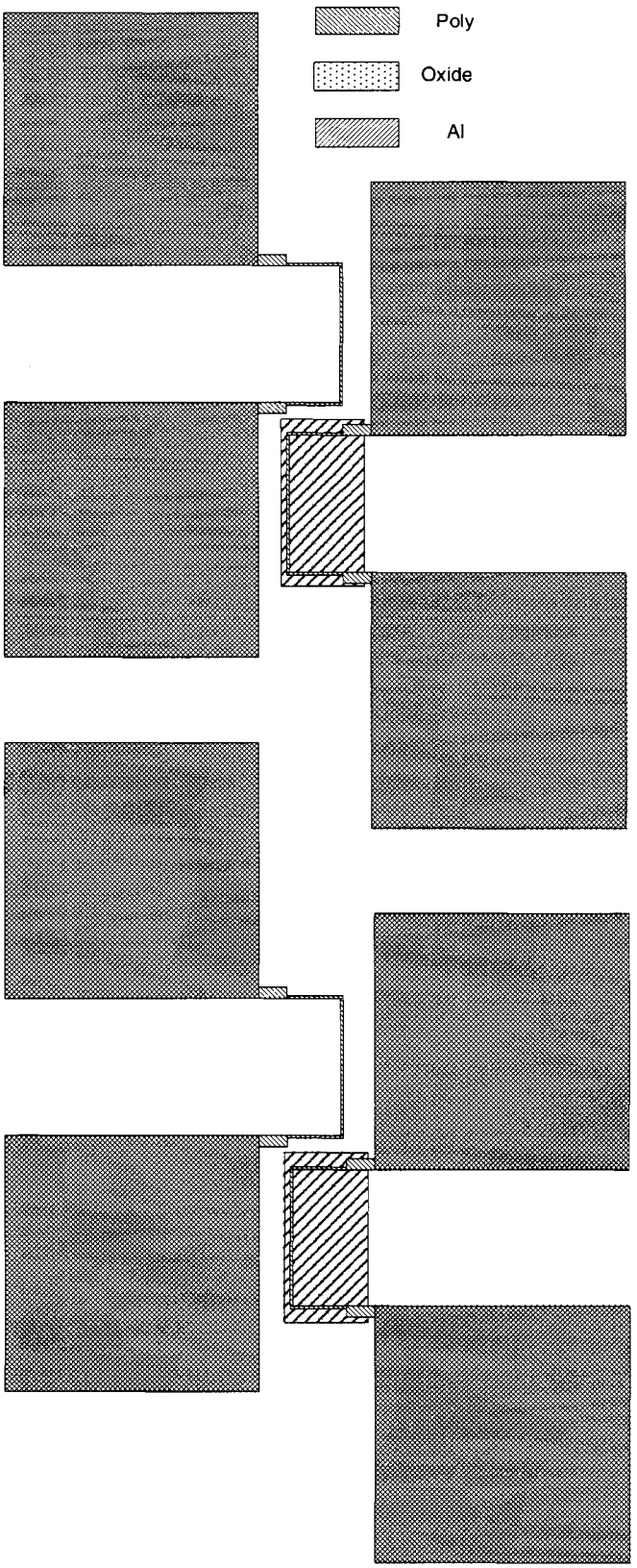


**Figure 3-7 Structures of pattern 8 in the fourth run**

#### 3.2.2.3 Mask 1

Mask 1 is used to define polysilicon structures, the resistors and the bonding pads. Figure 3-8 illustrates the layout of Mask 1 for the structures in the third design run (Figure 3-5).

#### 3.2.2.4 Mask 2

This mask is specially added for the Wheatstone bridge design. Mask 2 is used to open the contact area between the polysilicon bonding pad and aluminium while reserving the oxide layers in the dummy resistor area. If aluminium makes direct contact with the dummy polysilicon resistor underneath, the resistance of the dummy resistor will be significantly reduced, which makes the Wheatstone bridge extremely unbalanced and yield poor performance. There was one run that failed in this way in the third design, the details can be found in Appendix C.

Figure 3-9 illustrates the layout of Mask 2.

#### 3.2.2.5 Mask 3

Mask 3 defines the aluminium layer, which has two functions. First, aluminium is used for the bonding pads to provide electrical connection between the polysilicon bonding pads to the package; the second is used as the protective plane to prevent the dummy resistors from being released.

Figure 3-10 illustrates the layout of Mask 3.

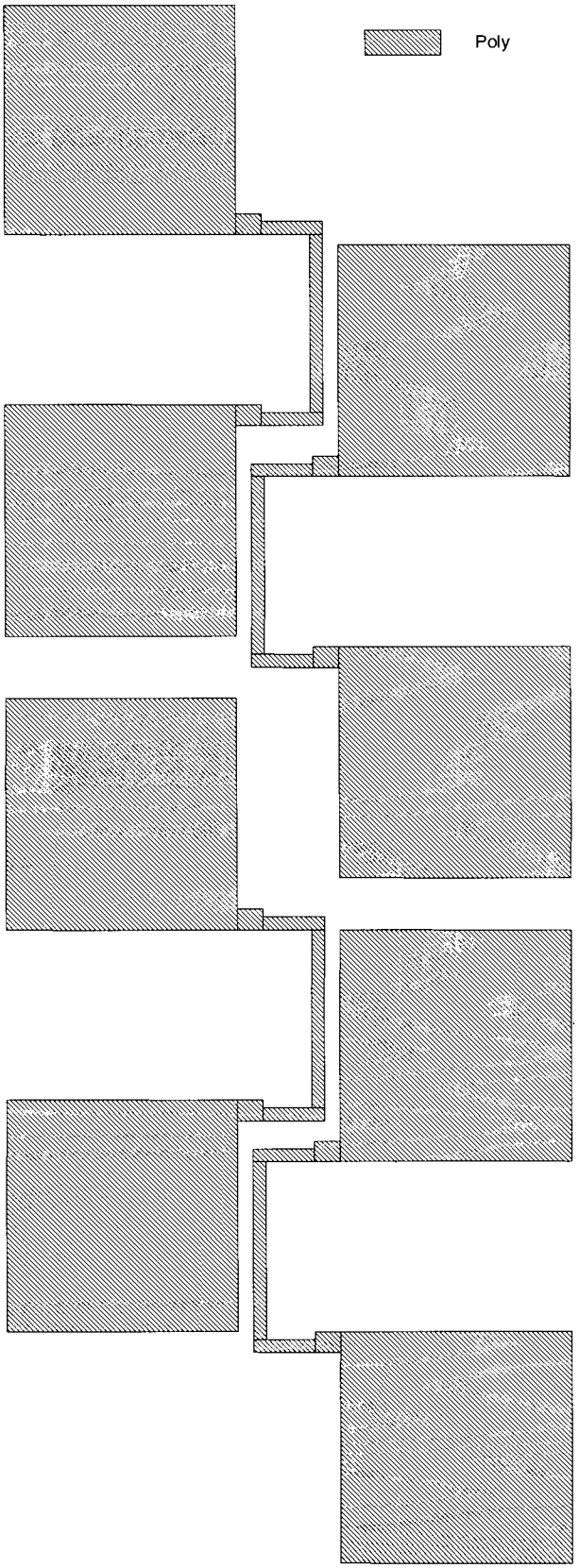


**Figure 3-8 Layout of Mask 1, third design run**

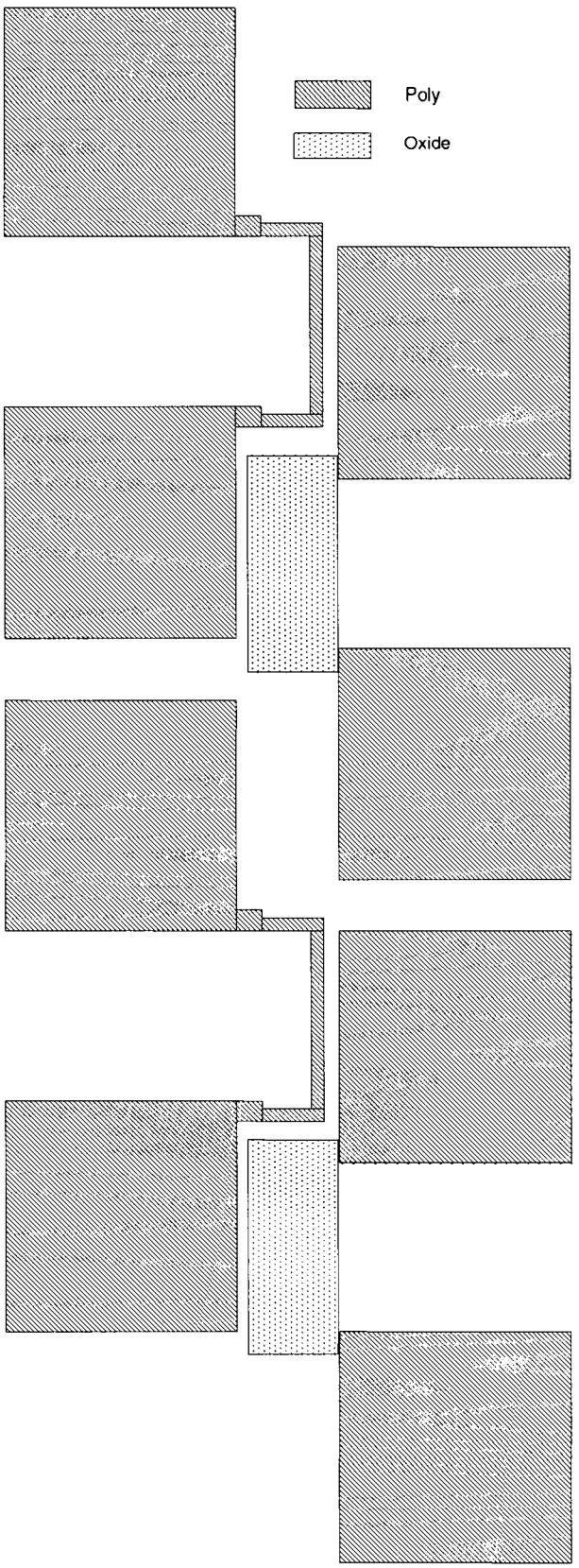


**Figure 3-9 Layout of Mask 2, third design run**

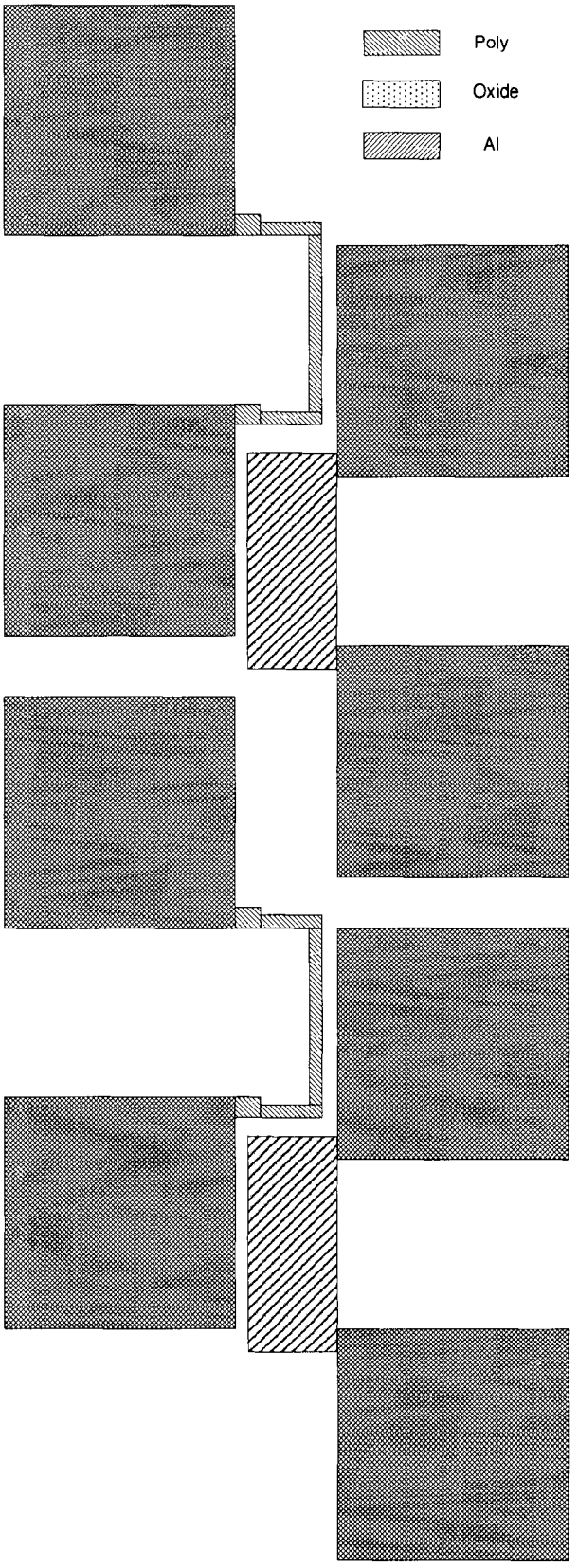


**Figure 3-10 Layout of Mask 3, third design run**

### 3.2.3 SEM Pictures of the Fabricated Devices

Pictures of the fabricated devices are taken by scanning electron microscope (SEM) in the Nano-imaging facility in Simon Fraser University. The pictures shown here are for the device of design pattern four in the fourth run. More pictures of other devices are given in Appendix D.

Design pattern four has only one finger. The resistors are in the cantilever shape and the line is 8μm wide and 200μm long. The resistances are in the 1kΩ ranges. Details about the different design pattern and summary of devices can be found in Appendices A and C.

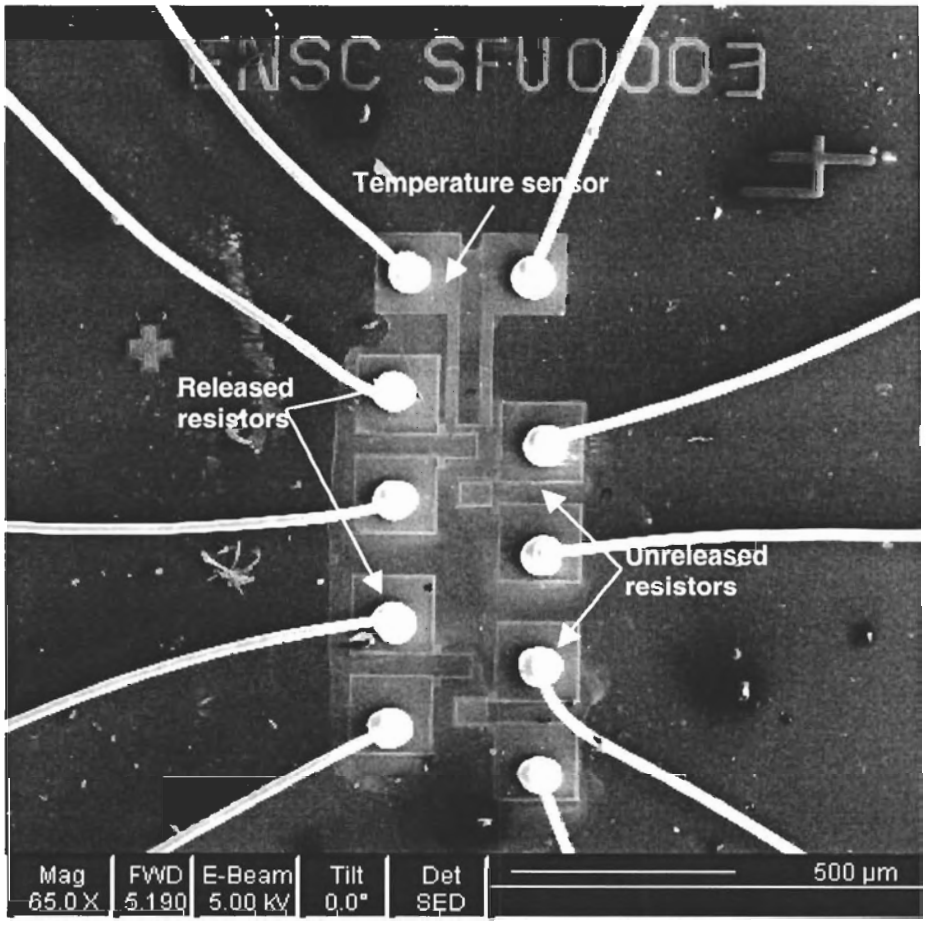


**a. Overall chip**

**Figure 3-11 SEM pictures of the pattern 4 of the fourth design run**

The picture above gives the overall layout of the device. It consists of two released resistors, two unreleased resistors and one aluminium resistor as the temperature sensor. The

temperature sensor was designed to measure the temperature of the nearby heater directly and compare the data with the temperature indirectly determined by the resistance changes. However it did not function well in the experiment, the resistance of the temperature sensor is too small to discern any changes in it.

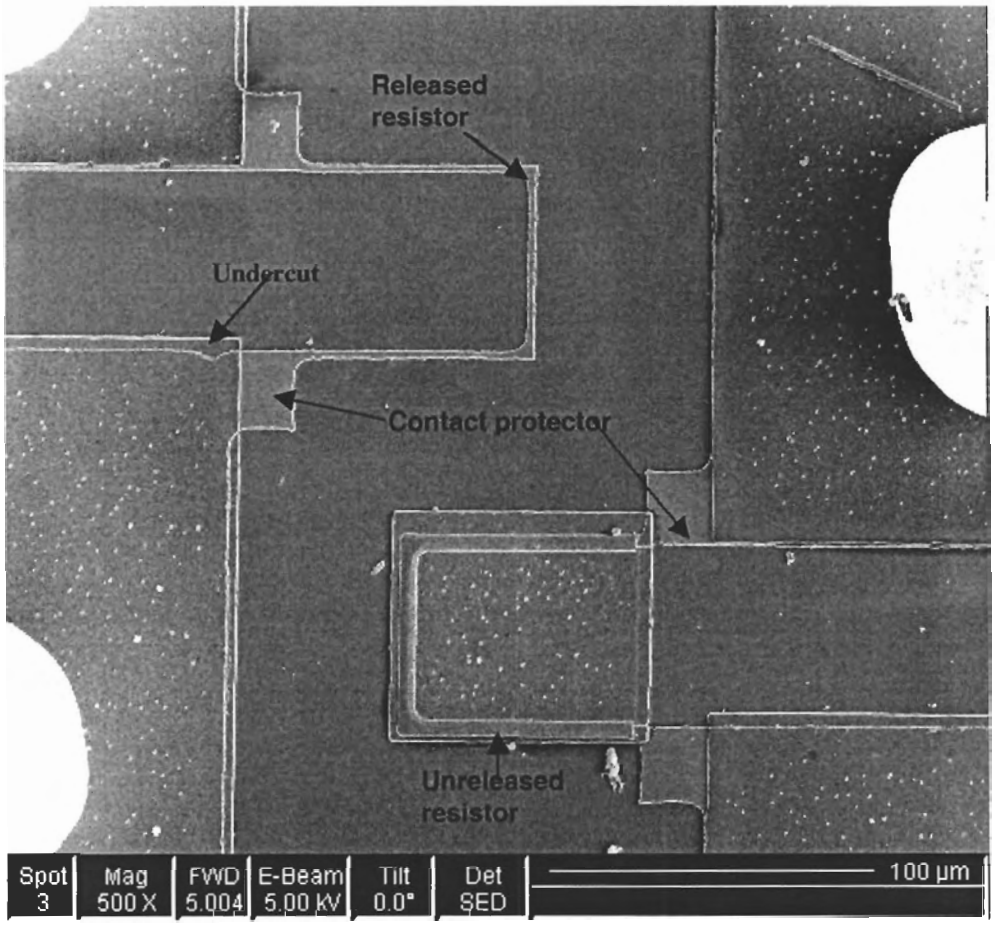


**b. Two resistors, top: released one; bottom: unreleased one**

**Figure 3-11 SEM pictures of the pattern 4 of the fourth design run**

The picture above is a half bridge with the released resistor on top and the unreleased one in the bottom. It is seen that the released resistor is much thinner than the unreleased one because of overetch; typically the line would shrink by 4μm after all the processing steps. There are two purposes for the part that contacts the line and the bonding pad to be relatively large; one is to separate the Al protective plane with the bonding pad, the other is to ensure the connection not

broken by overetch because it is not protected by Al. It is also seen the small undercut of the polysilicon in the edge of the bonding pad.

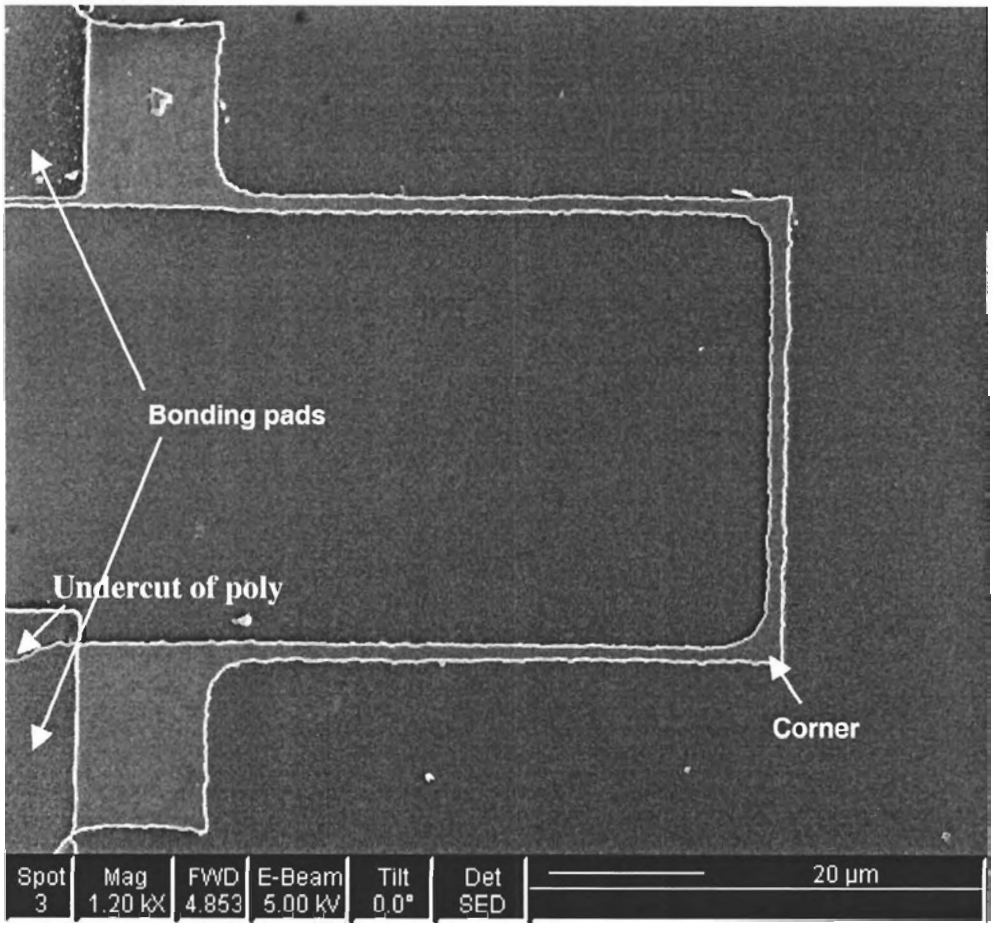


**c. Released resistor, heater**

**Figure 3-11 SEM pictures of the pattern 4 of the fourth design run**

A released resistor is shown in the picture above. The coarse edge of the line shown in the picture demonstrates the non-smooth surface of polysilicon. The corner takes longer to release.

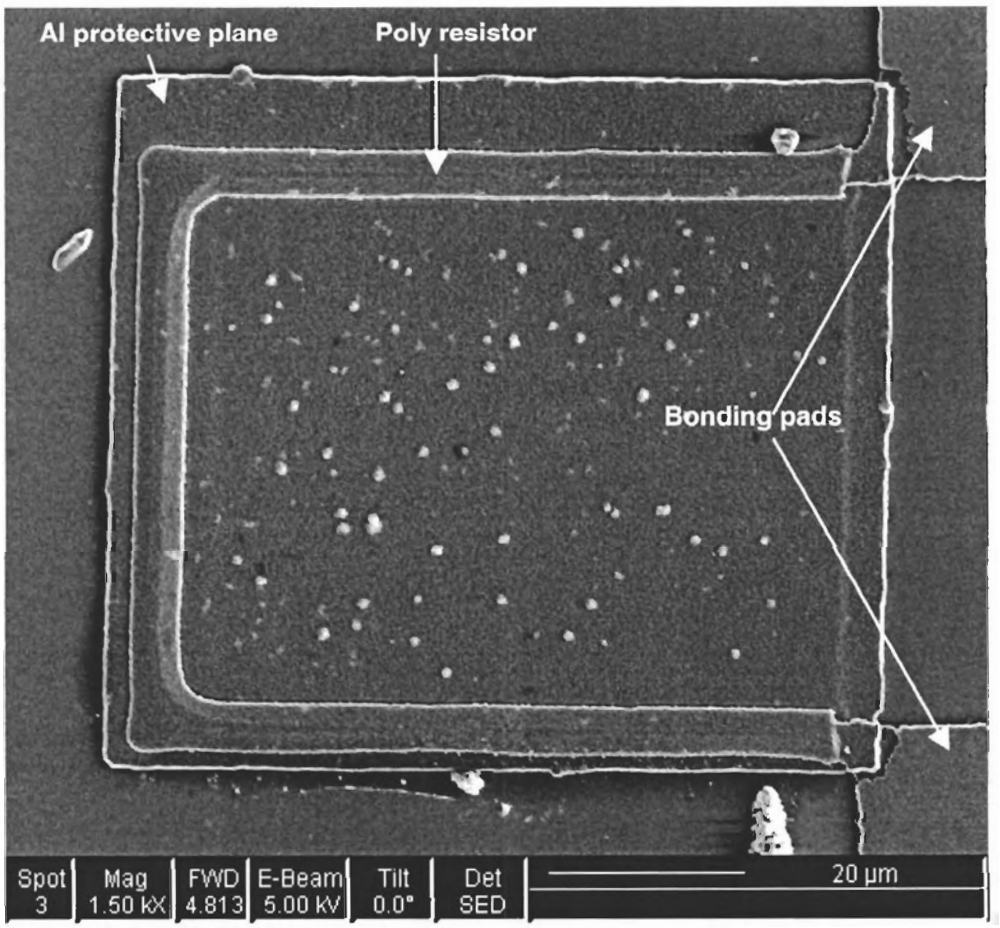


**d. Unreleased resistor, dummy resistor**

**Figure 3-11 SEM pictures of the pattern 4 of the fourth design run**

The picture shows an unreleased resistor. The aluminium etch mask is effective in its role to protect the oxide and polysilicon layers underneath. The polysilicon dummy resistor is intact in the fabricated device.

# CHAPTER 4 EXPERIMENTAL RESULTS

This chapter discusses the experimental set up and the test results for the pressure sensor. The performance of the sensor has been investigated for various structures for the heaters and the Wheatstone bridge under different power values.

There are four design runs in the experiments. The first two runs were designed to determine the optimum process parameters for the heater fabrication. The first run did not yield meaningful results. Based on the experience gained, the second run was successful in producing useful experimental data. The last two runs focus on the Wheatstone bridge configuration for optimisation of the design. The results shown here are mostly from the third and fourth runs.

The sensing element is the polysilicon heater resistor embedded in the $SiO_2$ films and suspended over the silicon substrate. A typical resistor is in the shape of a beam of 150μm long, 6μm wide and 0.55μm thick. The gap between the heater and the substrate is estimated to be in the nanometre range.

The Wheatstone bridge is used to measure small resistance changes and compensate for the ambient temperature drift. It consists of four identical polysilicon resistors: two of them are released and their resistances are sensitive to pressure changes. The other two are dummy resistors with pressure-independent resistances. When fed by a constant input voltage, the differential resistance changes in the heaters cause the bridge output voltage to change and the changes are pressure-dependent. The drift of the bridge output voltage due to the ambient temperature variations is cancelled by dummy resistors in the bridge.

## 4.1 Test Setup

The test system consists of the pressure system and the electrical measurement system. In the test, a known pressure is applied to the sensor and the outputs of the sensor are measured. The known pressure is referred as the reference pressure.

### 4.1.1 Pressure System

Figure 4-1 illustrates the setup of the pressure system. It consists of a pressure chamber, a regulator, a reference pressure meter and pipes. The pressure chamber has a socket to hold the chip and an electrical feed-through for the electrical signals coming in and out of the chamber. The chamber can withstand pressure up to 150psi (1.03MPa). The air comes from a compressed air system of the cleanroom. The amount of air entering the chamber is controlled by the regulator and the pressure is read by a PG-2000 commercial pressure sensor made by Scientific Technologies Inc.

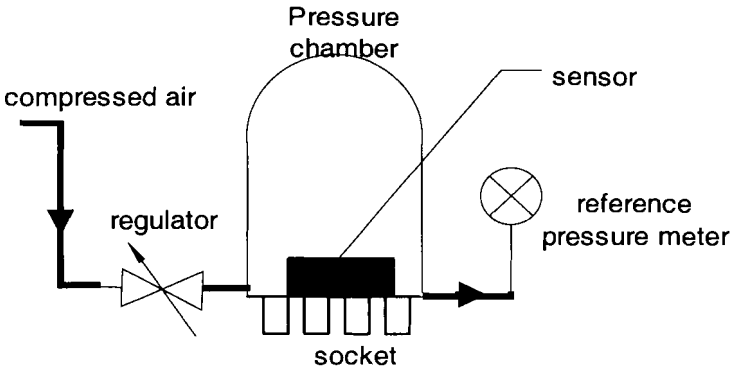


**Figure 4-1 Pressure system setup**

### 4.1.2 Electrical System

Because the constant-power (CP) operating mode is used, the electrical test setup is simple. It consists of a DC power supply, a voltmeter and an ammeter. Figure 4-2 gives the test setup for a single heater and a Wheatstone bridge, respectively. In the test set up for a single heater (Figure 4-2 (a)), the DC power supply applies a constant input voltage to the resistor, the

voltage is controlled by the operator and is recorded from the built-in voltmeter of the power supply; the ammeter measures the current flowing through the resistor. The resistance and heating power are calculated from the voltage and current measurements.

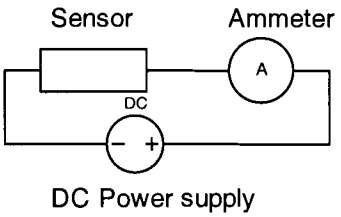


**(a) The single heater test setup**

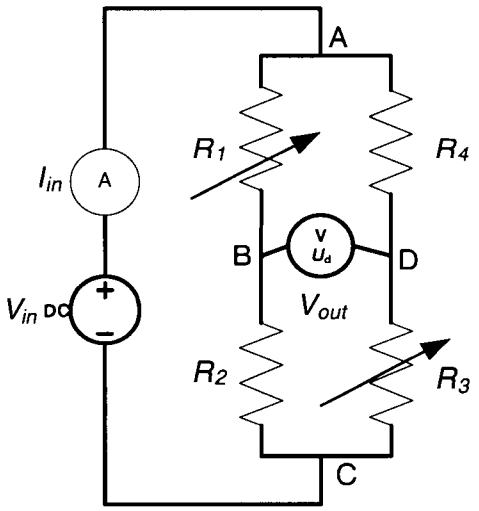


**(b) The Wheatstone bridge test setup**

**Figure 4-2 Setups of the electrical test system**

In the setup for the Wheatstone bridge shown in Figure 4-2 (b), resistors $R_1$ and $R_3$ are the pressure-sensitive heater resistors while $R_2$ and $R_4$ are the dummy resistors. The DC power supply applies a constant input voltage $V_{in}$ to the bridge. The ammeter measures the current drawn by the Wheatstone bridge $I_{in}$. The power applied to the sensor is calculated as the product of $V_{in}$ and $I_{in}$. A voltmeter records the bridge's output $V_{out}$. An amplifier is not necessary because the bridge's output is large enough (mVs). Detailed analysis of the Wheatstone bridge is in Appendix E.

## 4.2 Test Procedure

First the resistors were measured with an ohmmeter to check the integrity of the sensor. If there were no short or open circuits, and the resistances of the four resistors for the Wheatstone bridge were close, the sensor was subjected to a thorough test: the individual heater was tested as a pressure sensor first, and then the performance of the Wheatstone bridge was evaluated.

Oxide breakdown was conducted for some devices to break the thin layer of oxide between the polysilicon bonding pad and the aluminium above. The oxide may be the residual oxide from incomplete oxide etching or native oxide growing during the rinse in deionised water. It blocks the contact between the polysilicon and the aluminium.

The following measurements were conducted to get proper parameters of polysilicon.

### 4.2.1 Self-Heating of the Polysilicon Resistor

At a constant ambient temperature and pressure, the V-I relationship of the polysilicon resistors was measured in the released and unreleased resistors. Power and resistance were calculated from the measurement results and shown in Figure 4-3.

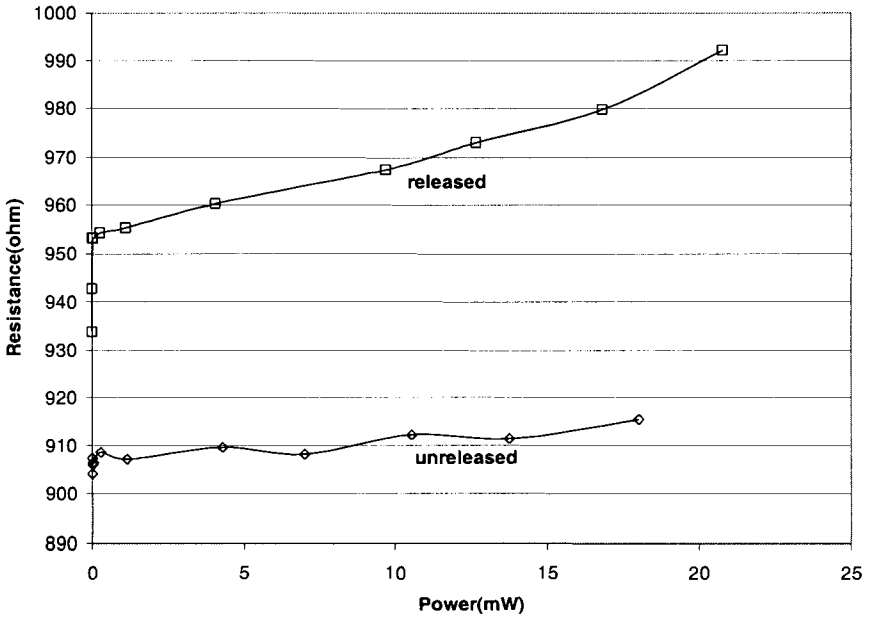


**Figure 4-3 Self-heating effect in polysilicon resistors –released and unreleased**

As shown in Figure 4-3, the resistance of the released polysilicon resistors increases significantly with increasing electrical heating power while the resistance of the unreleased resistors varies much less. It is because the dominant heat loss of the unreleased resistors is through the highly conductive silicon substrate ($k$=140W/m K), which makes the temperature rise in the resistors small, leading to a small change in resistance in turn. On the other hand, because of the tiny air gap that separates the released resistors from the substrate, the dominant heat loss of the released resistors is through the poor thermal conductor, the air ($k$=0.026W/m K), which leads to a significant temperature rise and the resistance increase in the resistors.

The relationship between the resistor and the power density of the released resistor is used later in the calculation to determine the value of the thermal conductivity $k$ of the gap. Details can be found in Chapter 5.

### 4.2.2 Temperature Coefficient of Resistance of Polysilicon

The temperature coefficient of resistance (TCR) of polysilicon is used to convert the resistance change of the resistor to its average temperature change and is dependent on the batch and fabrication process. The TCR of polysilicon was determined by placing a number of polysilicon resistors, released and unreleased, in a uniform temperature oven. The change in resistance was measured as the oven temperature was varied over a range from around 20°C to 80°C. The results are shown in Figure 4-4.

The TCR of polysilicon is calculated from the measured data. The nominal resistances of various samples at room temperature are approximately from1kΩ to 2kΩ; the resistors are 10μm or 20μm wide, 150μm to 250μm long. The temperature of the oven was changed from 20°C to 80°C and was measured by an alcohol-based thermometer placed directly in the oven next to the devices under test. The resistance was measured at various intermediate temperatures by an ohmmeter. From the data shown in Figure 4-4, the average TCR was calculated as 669ppm/°C for

the released polysilicon resistors for the temperature range from 20°C to 80°C and 611ppm/°C for the unreleased ones in the same temperature range. The difference between the values for released and unreleased resistors is due to the measurement error.

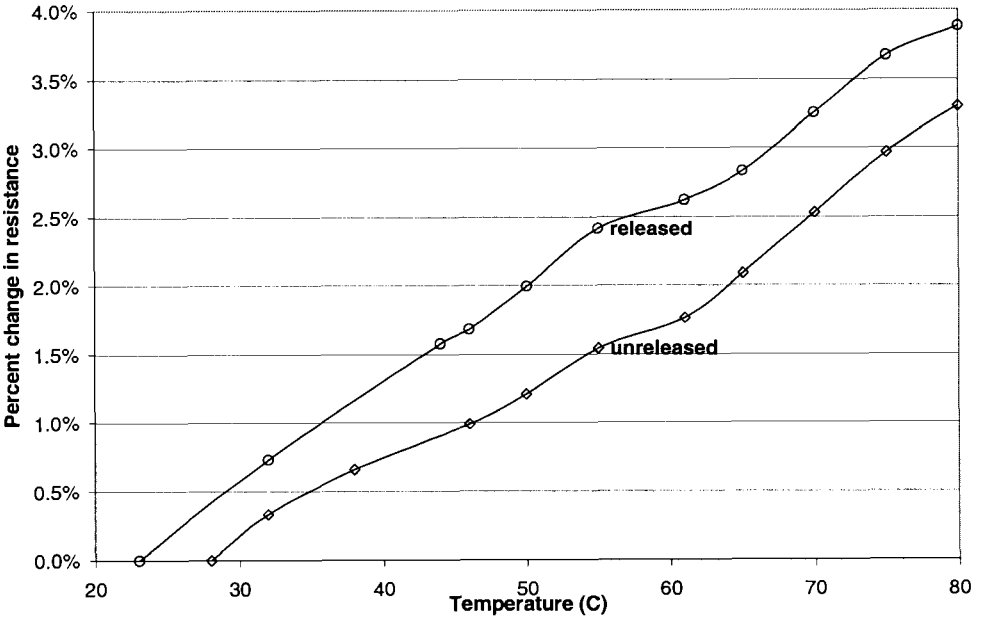


**Figure 4-4 Resistance changes with temperature for polysilicon resistors**

## 4.3 Test Results

The linearity, sensitivity and operating range of each sensor were evaluated under different heating power density conditions.

Measurements were done recording device output and corresponding pressure values at constant power densities from 0.001mW/$\mu m^2$ to 0.02mW/$\mu m^2$. The pressure range is from 14.7psia (101.3kPa) to approximately 117.6psia (810.6kPa).

The power density is calculated by dividing the electrical power applied to the sensor by the area of the resistors. The power consumed by the sensor is equal to the product of the voltage and the current of the power supply.

The devices under test are identified as No. 1 to No.5. No. 1, 4 and 5 are devices of the

fourth run while No. 2 and 3 are from the third run. Table 4-1 gives some important parameters of the devices.

**Table 4-1 Important parameters of the devices under test**

| ID | **Size** (widthμm × lengthμm × finger*) | **Area** (μm2) | **Resistance** (Ω) R1/ R2/ R3/ R4 | **Notes** |
|---|---|---|---|---|
| **1** | 4.25×250×1 | 1062 | 957/891/999/909 | 4th run, pattern 8 |
| **2** | 4.55×750 | 3412 | 1263/1237/1276/1252 | 3rd run |
| **3** | 6.72×250 | 1680 | 407/409/405/401 | 3rd run |
| **4** | 2.05×150×4 | 1230 | 368/365/361/369 | 4th run, pattern 3 |
| **5** | 4.15×200×2 | 1660 | 467/427/454/442 | 4th run, pattern 5 |

* The fourth run is a multi-finger design, the third number in the size column is to indicate the number of fingers in the structures; there is no such number in the devices from the third run, because they all have one finger.

### 4.3.1 Device Calibration and Linearity

Experiment results are shown in Figure 4-5 with $V_{diff}$ versus pressure for the five devices listed in Table 4-1 with power density as 0.01mW/$\mu m^2$. The $V_{diff}$ is the change of the output voltage of the Wheatstone bridge, expressed as $V_{diff} = V_{out_{n+1}} - V_{out_n}$. The offset of $V_{diff}$ due to device mismatch is removed and set to 0V at 1atm (101kPa).

In Figure 4-5, the horizontal axis represents the pressure applied to the pressure chamber in kPa, and the vertical axis represents $V_{diff}$ in mV.

It is seen that when pressure changes from 100kPa (1atm) to 800kPa (8atm), $V_{diff}$ increases from around 2mV to 19mV for the five devices, respectively. The change in $V_{diff}$ results from the expected decrease in the heater resistance with rising pressure. Higher pressure introduces more air molecules for heat conduction, and more heat lost leads to a temperature decrease and reduced heater resistances. The curves are similar to the one in the large-response zone in Figure 2-2. The change is more significant in the lower end of pressure and slows down when pressure gets higher and reaches the value of the transition pressure.

It is also seen that the device's response is not linear. Two major factors contributing to the non-linearity are the pressure-independent solid thermal conduction and the pressure-

dependent Knudsen number effect. The solid thermal conduction is determined by the solid contact area between the polysilicon resistor and the silicon substrate, including the bonding pads and collapsed part of the resistors. It is constant all over the pressure range and the significance is affected by the ratio between the solid contact areas to the air gap areas. The nonlinearity introduced by the Knudsen number effect changes with pressure and is more significant at the higher end of the pressure. With rising pressure, the mean free path of gas molecules becomes smaller, so is the Knudsen number. From (2.8), the change of thermal conductivity of air slows down with pressure.

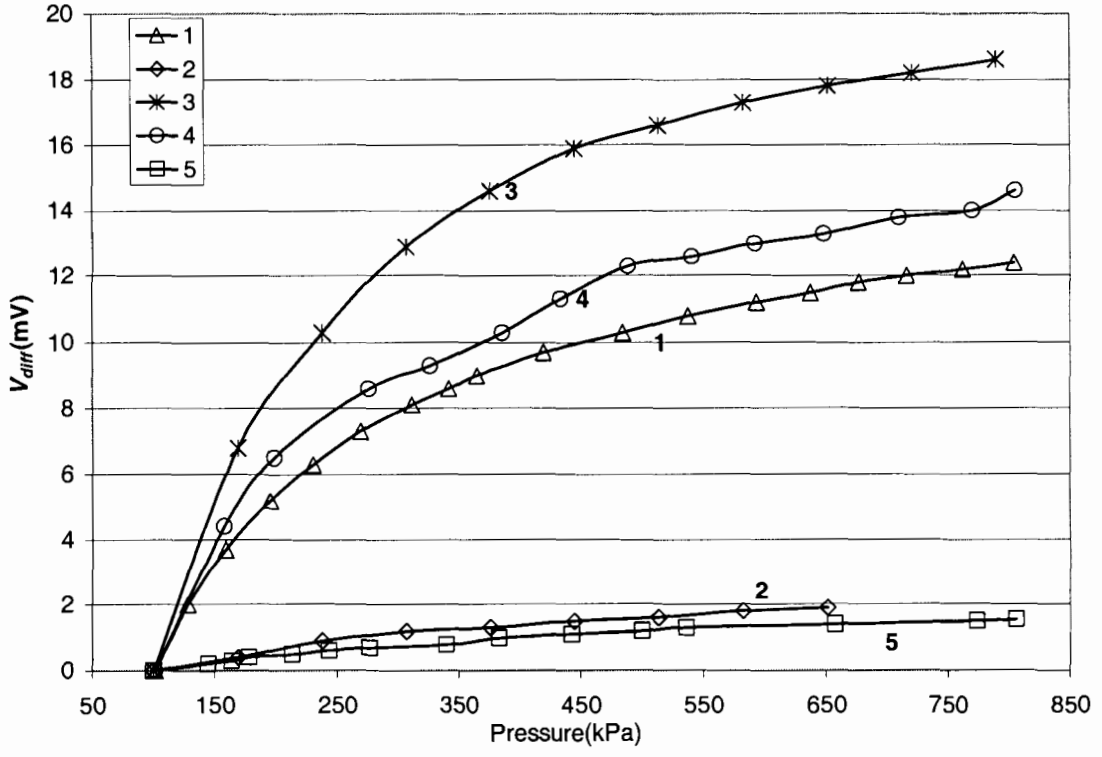


**Figure 4-5 $V_{diff}$ vs. Pressure under a power density as 0.01 mW/$\mu$m$^2$**

Figure 4-6 gives the nominal percent change of $V_{diff}$ versus pressure. Device No.3 shows a nearly 50% change of $V_{diff}$ in the pressure range from 100kPa to 800kPa while devices No. 1 and 4 show a 10% and 15% change respectively. Devices No. 2 and No.5 do not response well to

pressure, $V_{diff}$ changes are below 2%. The difference of the performance is mainly determined by the thermal conduction through the air gap areas, details are discussed in Chapter 5.

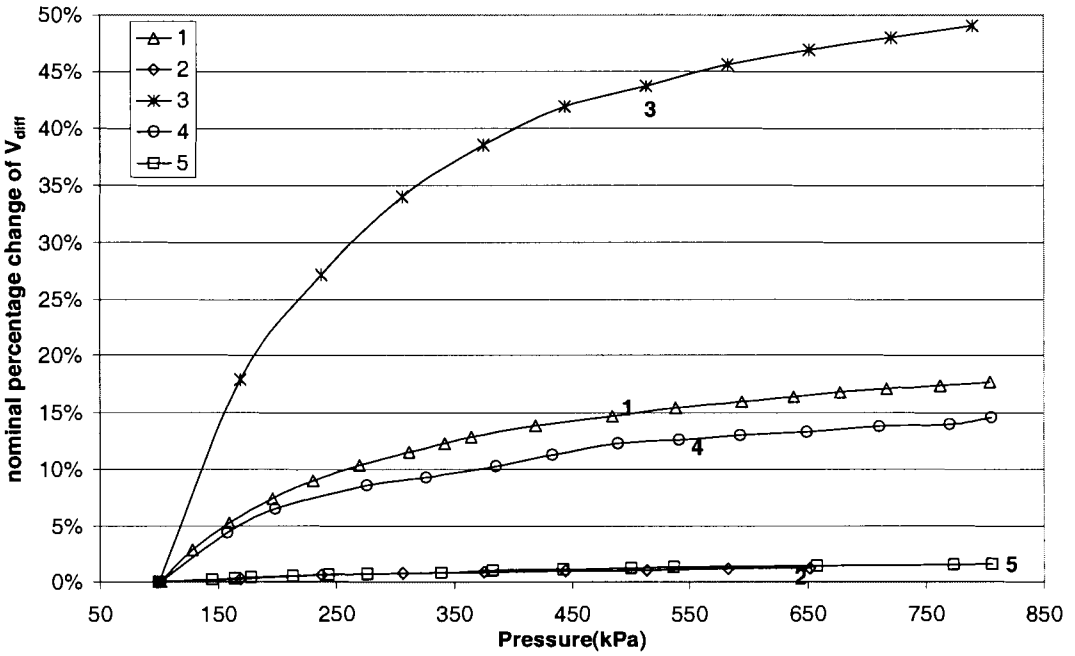


**Figure 4-6 Nominal percent change of $V_{diff}$ vs. Pressure at a power density of 0.01 mW/$\mu$m$^2$**

### 4.3.2 Power Effects

The change of the Wheatstone bridge output voltage, $V_{diff}$, under various power densities for device No. 1 is shown in Figure 4-7. All the other test conditions are the same except the differences in power densities.

Figure 4-7 shows that at a fixed pressure, the measured $V_{diff}$ increases with increasing power density. It is straightforward because $V_{diff}$ of the Wheatstone bridge is proportional to its power supply. It is clear that when power density changes from 0.002mW/um$^2$ to 0.004mW/um$^2$ and then to 0.008mW/um$^2$, $V_{diff}$ doubles. However when power density changes from 0.008mW/um$^2$ to 0.01mW/um$^2$, $V_{diff}$ more than doubles. This phenomenon cannot be explained clearly now, more investigation is required.

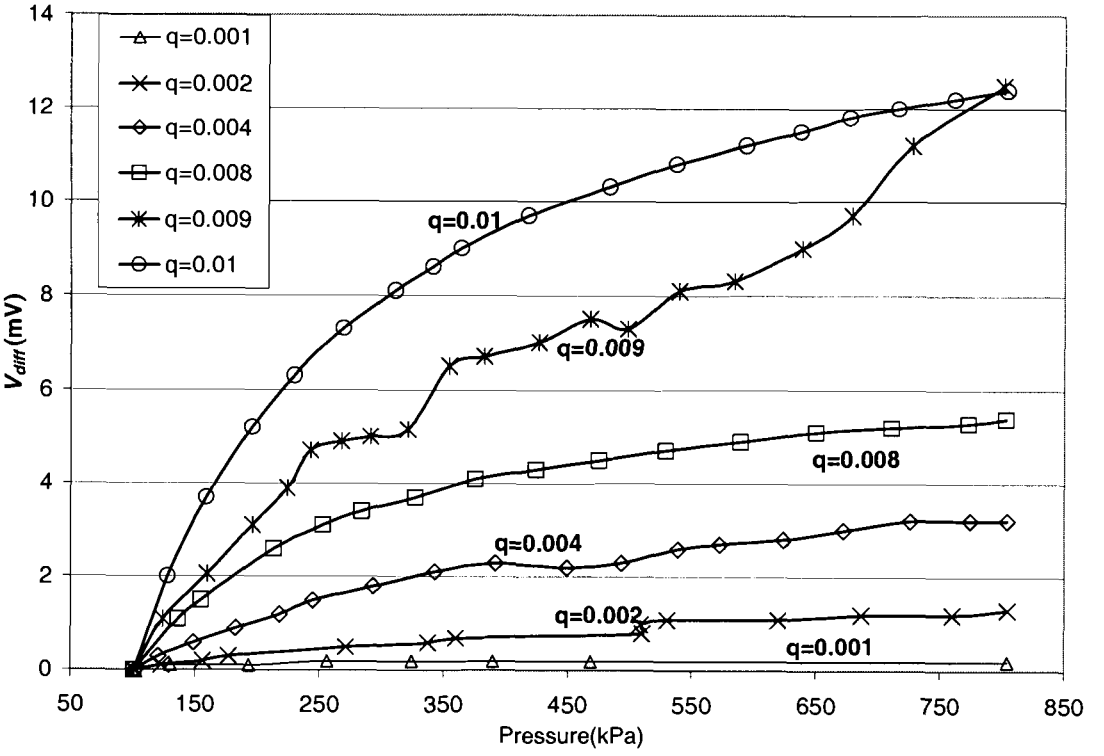


**Figure 4-7** $V_{diff}$ **changes with pressure for sensor No.1 under different power densities**

### 4.3.3 Device Sensitivity

The device sensitivity, $S$, is defined as the relative change of the output voltage per unit of applied pressure, $p$, at the sensors. It is expressed as $S = \frac{V_{diff}}{V}\frac{1}{p}$ for the Wheatstone bridge configuration or $S = \frac{\Delta R}{R}\frac{1}{p}$ for a single heater.

For an equal-resistance Wheatstone bridge, $V_{diff}$ is determined by (E.11), $V_{diff} \approx \frac{\Delta R_1 - \Delta R_2 + \Delta R_3 - \Delta R_4}{4R} V_{in}$. In the bridge, the common mode resistance changes in $\Delta R_1$, $\Delta R_2$, $\Delta R_3$ and $\Delta R_4$ that are irrelevant to pressure are cancelled, only the differential resistance changes in $\Delta R_1$ and $\Delta R_3$ that reflect the pressure change are counted in the final output voltage change, thus

$$V_{diff} = \frac{1}{2}\frac{\Delta R}{R}V_{in}. \tag{4.1}$$

So the sensitivity can be expressed as:

$$S = \frac{\Delta R}{cR}\frac{1}{p} \tag{4.2}$$

where $c$ is a constant

Considering $\Delta R/R = \alpha\Delta T$, the device sensitivity is governed mainly by the TCR of the material for the resistors.

The sensitivity can be evaluated from the device calibration curves. The experimental curves was approximated as $V_{out} = c_1 p + c_2$, the device sensitivity is the slope of the line as $S = c_1$. The average sensitivity as the mean approximate derivative of the device calibration curve is calculated and listed in Table 4-2.

Data from Table 4-2 correspond to device No. 1 with the same test condition except the different power densities.

**Table 4-2 Device sensitivity of sensor No.1 corresponding to power density**

| **Power density** ($mW/\mu m^2$) | **Sensitivity** (mV/kPa) Full range (100-830 kPa) | **Sensitivity** (mV/kPa) Half range (100-480 kPa) |
|---|---|---|
| **0** | 0.0 | 0.0 |
| **0.001** | 0.7 | 1.4 |
| **0.002** | 4.1 | 4.8 |
| **0.004** | 7.6 | 13.8 |
| **0.008** | 18.6 | 28.2 |
| **0.009** | 21.4 | 29.6 |
| **0.012** | 42.0 | 64.1 |

The numbers in the middle column are calculated for the full measurement range (100-830kPa) while the rightmost is for pressure range from 100-480kPa (called half range). It is seen when pressure is low, devices are more sensitive to the pressure change. When pressure is high, voltage changes slow down.

The data in Table 4-2 is drawn in Figure 4-8. It is seen from Figure 4-8 that the device's sensitivity increases with its electrical power. An increase in the heating power leads to an increase in heater's temperature, in turn amplifies the temperature change when pressure changes.

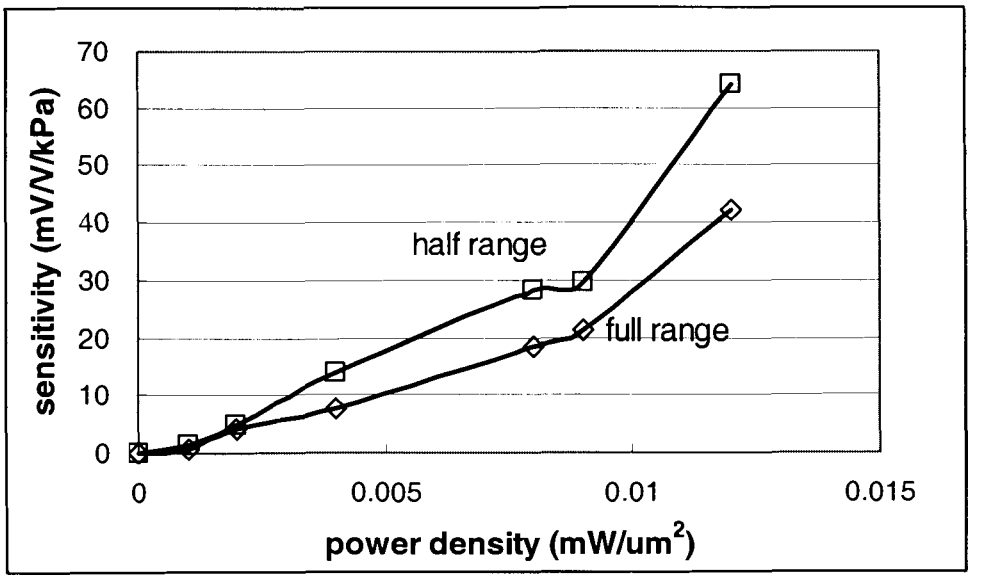


**Figure 4-8 Sensitivity vs. power density for sensor No.1**

### 4.3.4 Measurement Range

The lower limit of measurement range is determined by the solid conduction and thermal radiation. At low pressures, there are simply not many gas molecules available for the gas thermal conduction, so the thermal conductivity of gases approaches zero and the thermal conduction through solid contacts dominates.

The upper limit is set by the transition pressure $P_{tr}$, determined by (2.8). For example, $P_{tr}=2K_N \cdot P$ with $Pr=1$ and $\gamma=1$. It is when $\lambda = d/2$, $P_{tr} = P$; for $d$=50nm, $P_{tr}$ is about 70psia (483kPa), which agrees with the experimental data from our test and others [4, 15]. Using more practical numbers like $Pr$=0.7 and $\gamma$=1.1 ($\gamma$ is always than 1 practically), $P_{tr}$ is the pressure when $\lambda = d/3$. The transition pressure is 105psia (700kPa) when $d$ is 50nm under this condition. The data in our experiments also show that the sensor still responds to pressure change well beyond 70psia

(483kPa). We stopped testing the sensor at around 120psia (830kPa) because of the test setup, not because the sensor stops changing with pressure. There are still a lot room for improvement. We did not test the sensor in vacuum measurement. From theoretical analysis and the previous work, we believe the sensor is capable of measuring pressure below 100kPa.

### 4.3.5 Repeatability and Long-Term Stability

Some of the devices have been tested two or three times under the same test conditions, the results are encouraging in indicating an acceptable repeatability for the sensor. However, due to the constraints on time and device availability, statistic results on repeatability and long-term stability have not been gathered to satisfaction. The future work in Chapter Six will discuss more about this problem.

### 4.3.6 Summary of the Four Runs

The four runs are summarized in Appendix C.

# CHAPTER 5 DISCUSSIONS

As described earlier, heat loss of the heater to the ambient is primarily caused by solid conduction or air conduction. The magnitude of each term depends on the sensor structure and the ambient conditions. In this chapter, the heat conduction mechanisms for the sensor are analysed and the theoretical model has been developed based on the analysis. The sensor errors are evaluated for drifts in ambient temperature, gas flow and gas types.

## 5.1 Heater Structures

The heater is a polysilicon resistor suspended over a silicon substrate as shown in Figure 5-1, which gives the dimensions of the resistor, such as the width $w$ (not shown), length $l$, thickness $z$, and gap $d$.

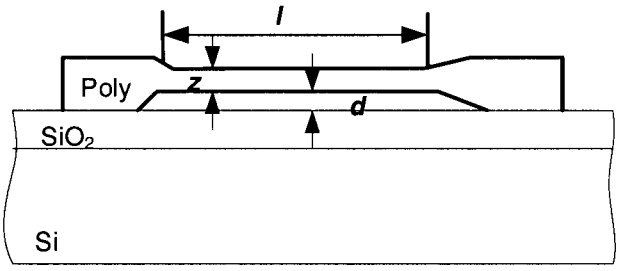


**Figure 5-1 A cross section of the heater and the heater dimensions**

In the fabricated device, the heater is not straight as the one shown in Figure 5-1. During the structure-releasing step in the fabrication, the heater collapses to the substrate and stick there because of surface tension and stiction effect discussed in Chapter 3. A simplified version of the collapsed heater resistor is drawn in Figure 5-2, where the heater is divided into two parts, the collapsed part and the suspended part. We assume that the collapsed part is in the center of the beam with a length of $l_c$; the suspended parts are in the two ends of the beam and each has the same length of $l_s$.

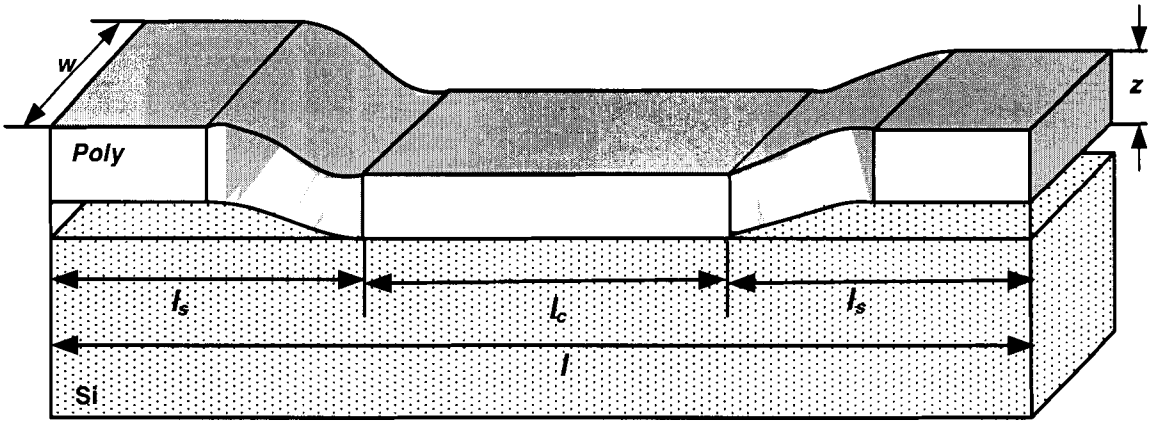


**Figure 5-2 Cross-section view of the collapsed heater**

As has been discussed in Section 2.2.2, two solid surfaces apparently in contact, only touch each other at a few individual spots. "Even at relatively high contact pressure, the actual contact area for most solid surfaces is only about 1 to 2% of the nominal contact area [10]." The interface between the polysilicon and silicon in the collapsed part of the beam $l_c$ is magnified in Figure 5-3. It is clear in Figure 5-3 that the gap distance $d$ is not constant over the whole collapsed part, only the average value is used.

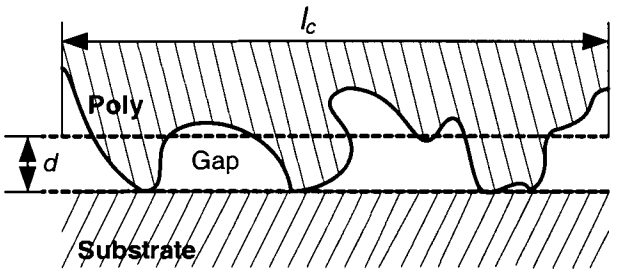


**Figure 5-3 Magnified cross-section view of the collapsed part of the beam**

Figures 5-2 is re-drawn in Figure 5-4 to illustrate the facts discussed in Figure 5-3. In Figure 5-4, the solid contact spots are 'real' solid contacts (e.g. no air gap among them). It is seen there are only a few of them in the beam.

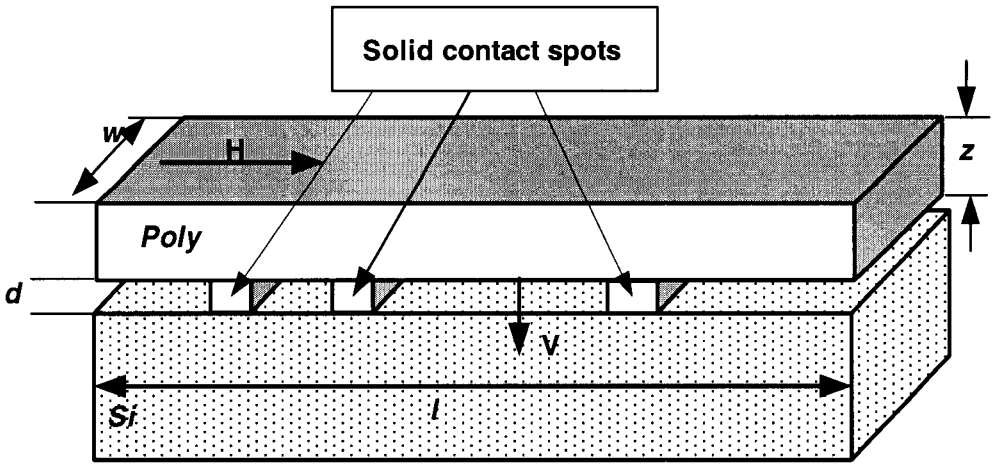


**Figure 5-4 Equivalent view of the beam in cross-section view**

## 5.2 Thermal Conduction of the Heater

As discussed in Chapter 2, the heat loss of the sensor to the environment is attributed to four factors:

a) Conduction through solid contacts between the resistor and the substrate, such as the bonding pads and the contact spots in the collapsed beam.

b) Conduction through the air gap.

c) Convection

d) Radiation.

Conduction losses listed in (a) are not pressure-sensitive, while conduction losses in the air gap (b) are pressure-dependent.

In our sensors, convection losses (c) and radiation losses (d) are negligible. "Convective heat transfer is usually negligible for gap widths of up to about 6mm (corresponding to Grashof numbers of 2000 for air at atmospheric pressure of 101kPa and temperature of 300K) [10]". In our estimation, the interfacial gap is approximately 50nm to 100nm wide and too small for significant convection currents in the gap. For the heat loss from the area above the sensor, the heat transfer path is much longer than the gap distance; heat loss from above the resistor is

shunted by the heat loss through the gap. Radiation is negligible too because the working temperature of our sensors is only around 100°C, less than 300°C [10]. So the primary heat loss in the sensor is from conduction losses (a) and (b), and because "the area available for heat flow through the interstitial gaps is frequently 2 to 4 orders of magnitudes greater than the actual contact area [10]", the principal heat loss mechanism in the sensor is the conduction loss through the air gap (b).

The heat conduction is considered steady because the time response is not important at this stage; there are sufficient time intervals between each reading. The heater is the source of the heat flux and the silicon substrate is the heat sink. Heat is generated from Joule heating of polysilicon resistors. It is assumed that the electrical current flows evenly in the beam along the horizontal direction and the heat is evenly generated from the beam. Assuming that the heat is only conducted in two directions- horizontal direction (denoted 'H' in Figure 5-4 and vertical direction (denoted 'V' in Figure 5-4), the temperature distribution of the beam along its horizontal direction is approximately homogeneous, and the temperature gradient is linear along the vertical direction owing to its thin structure.

For our sensor, we assumed that most heat was conducted in the vertical direction through the air gap. The following analysis compares the thermal conductance in these two directions to prove the validation of our assumption and provide optimisation approaches for the sensor.

For ease of analysis, the beam in Figure 5-4 is modelled in Figure 5-5. In the model, all the individual spots are collected together to re-arrange the beam into two parts, the 'real' solid contact part and the air gap part. Of the total length of the beam $l$, the solid contact part has a length of $\xi \cdot l$ while the air gap part takes the remaining $(1-\xi)l$, where $\xi$ is the coefficient denoting the percentage of the beam area that makes solid contact to the substrate.

Thermal conductance of a material, $G$, is calculated by the following formula:

$$G = \frac{Q}{\Delta T} = \frac{kA}{l} \tag{5.1}$$

where $Q$ is the total heat flow, $k$ is the thermal conductivity of the medium, $A$ is the nominal heat conduct area, $l$ is the distance travelled by the heat flow and $\Delta T$ is the temperature difference across the distance $l$.

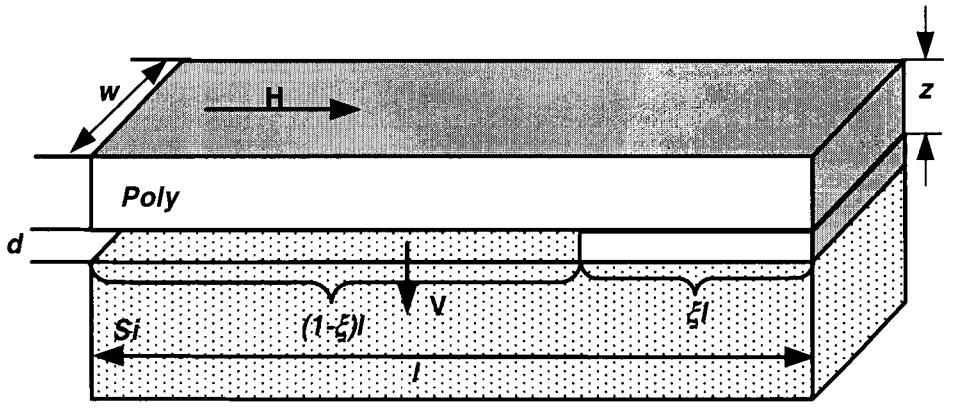


**Figure 5-5 Model of the collapsed beam**

In the horizontal direction, the heat flows through the polysilicon layer into the area $A_H = w \times z$ for distance $l$, as shown in Figure 5-5. The thermal conductance in the horizontal direction is

$$G_H = \frac{k_p wz}{l} \tag{5.2}$$

where $k_p$ is the thermal conductivity of polysilicon.

In the vertical direction, the heat conduction is the sum of the solid conduction and air conduction.

In the solid contact part, heat is conducted through polysilicon to the substrate directly with the distance $d$ that is the thickness of the gap instead $z$, the thickness of the polysilicon layer and area $\cdot\xi l \cdot w$, assuming the temperature of the beam (the polysilicon layer) is constant along the

horizontal direction, so the thermal conductance is

$$G_{Vp} = k_p \frac{\xi \cdot l \cdot w}{d}. \tag{5.3}$$

In the air gap part, heat is conducted through the air gap to the substrate. In the air gap part, the heat-conducted area is $(1-\xi)\cdot l \cdot w$ and the distance is $d$, so the thermal conductance is

$$G_{Vg} = k_g \frac{(1-\xi)\cdot l \cdot w}{d} \tag{5.4}$$

where $k_g$ is the thermal conductivity of the gap.

The total thermal conductance in vertical direction is

$$G_V = G_{Vp} + G_{Vg} = k_p \frac{\xi wl}{d} + k_g \frac{(1-\xi)wl}{d}. \tag{5.5}$$

The thermal conductance in the vertical direction is compared to that in the horizontal direction, the result is

$$\begin{aligned} G_V / G_H &= \frac{k_p \frac{\xi wl}{d} + k_g \frac{(1-\xi)wl}{d}}{\frac{k_p wz}{l}} \\ &= \frac{k_p \frac{\xi}{d} + k_g \frac{(1-\xi)}{d}}{k_p z} l^2 . \end{aligned} \tag{5.6}$$

A large ratio means more heat is conducted in the vertical direction and if the heat is conducted through the air gap, the sensitivity of the sensor would be higher. For example, assuming some typical values in (5.6), with $k_p$ = 40 W/m K [30], $k_g$ = 0.026 W/m K, $z$ = 500nm, $d$ = 50nm and $l$=100um, $G_V/G_H$ is 40,000 when $\xi$=1 and 260 when $\xi$=0.

The example shows that most of the heat is conducted away from the heater in the vertical direction and little heat is lost in the horizontal direction. This is because the thermal

conductivity of polysilicon is almost 1600 times of that of the air. Since most heat is distributed vertically, it is necessary to analyse heat conduction in vertical direction in details.

### 5.2.1 Model of the Collapsed Beam

The thermal conduction in vertical direction consists of the one through the contacts and the one through the air gap. The magnitude of each term depends on the beam structure. Based on the analysis of the conductions through these two parts, a model has been derived to relate the sensor's sensitivity to the coefficient $\xi$ that denotes the areas that make contact with the substrate.

According to Figure 5-5, the beam is divided into two parts: a solid contact part and an air gap part. The heat flow is separated into two parts accordingly: one through the solid contact, $Q_t$, and the other through the air gap, $Q_g$ [10]

$$Q = Q_t + Q_g . \tag{5.7}$$

The solid contact conductance in unit area is defined as

$$g_t = Q_t / A_t \Delta T \tag{5.8}$$

and the air conductance of the gap in unit area is defined as

$$g_g = Q_g / A_g \Delta T . \tag{5.9}$$

In the air gap, heat is conducted through two materials, $SiO_2$ and air. The total thermal conductance in the gap is the conductance of the two materials in serial, $g_g = g_o \,//\, g_a$. In the solid contact area heat is conducted through two materials, polysilicon and $SiO_2$. Similarly, the total thermal conductance in the solid part is $g_t = g_p \,//\, g_o$. The $g_p$, $g_o$ and $g_a$ are the thermal conductance for polysilicon, oxide and air, respectively.

Because the temperature distribution in the beam is linear along the vertical direction, the thermal conductance $g$ is equal to $k/l$, where $k$ is the thermal conductivity of the medium, and $l$ is

the distance travelled by the heat flow. For polysilicon and air, $l$ is the gap $d$; for $SiO_2$, $l$ is the thickness of the material.

$$g = k/l \tag{5.10}$$

Because the temperature of the beam is constant in the horizontal direction, the temperature difference between the beam and the substrate in both parts is the same. The total thermal conductance is

$$\begin{aligned} Q &= Q_g + Q_t \\ &= g_g A_g \Delta T + g_t A_t \Delta T \end{aligned}, \tag{5.11}$$

Using the relationship between the areas like $A_g + A_t = A$, $A_g = (1-\xi)A$, and $A_t = \xi A$, then

$$\Delta T = \frac{q}{(1-\xi)g_g + \xi g_t} \tag{5.12}$$

can be derived, where $q$ is the power density (heat flux) defined as $q = Q/A$.

The equivalent thermal conductivity $k_{eq}$ in the vertical direction is

$$k_{eq} = \left((1-\xi)g_g + \xi g_t\right)d\,. \tag{5.13}$$

Typical values are calculated for $k_{eq}$ using (5.13). The thermal conductivity of air corresponding to pressure is determined by (2.7), where $k_c$ is 0.026 W/m K and the gap distance $d$ is 50nm. The thermal conductivity for polysilicon and oxide is determined by (5.10). The thermal conductivity values used in the calculation for polysilicon are 34.5 W/m K and 1.17 for $SiO_2$ respectively [33]. The heat travel distance in the polysilicon layer is the same as the gap $d$, 50nm while the oxide is assumed to have a uniform thickness of 20nm, although the exact value is unknown. The contact area factor $\xi$ is varied to demonstrate its effect on the sensitivity of the

sensor. For example, the curve named 'theory, solid 1%' represents the theoretical values of $k_{eq}$ with solid contact areas account for only 1% of the total area of the beam ($\xi$=0.01), values for $\xi$=0.05 and $\xi$=0.5 are also shown.

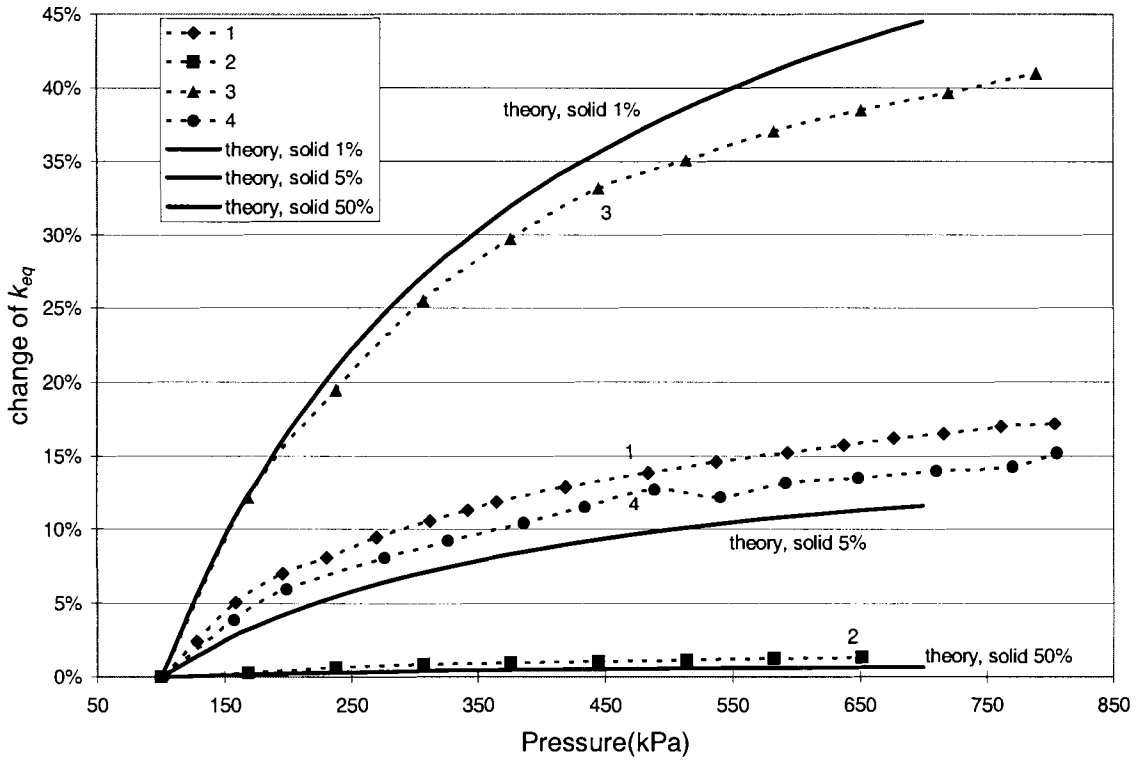


**Figure 5-6 Change in $k_{eq}$ vs. Pressure for different value of $\xi$**

In Figure 5-6, devices No. 1, 2, 3 and 4 are the same sensors listed in Figure 4-5. The experimental data in Figure 5-6 are calculated from the measured data in Figure 4-5. The general procedure is as follows: from the data in Figure 4-5 ($V_{diff}$ vs. Pressure), $\Delta R/R$ is obtained using

(E.12) $\frac{\Delta R}{R} = \frac{\Delta R_1}{R_1} = \frac{\Delta R_3}{R_3} = \frac{AV_{in} - BV_{out}}{DV_{out} + 2R_1R_3V_{in}}$ derived from the analysis of a Wheatstone bridge,

then $\Delta T$ is calculated from (E.14) $\Delta T = \Delta R/R_0/\alpha$. From there, the experimental data of $k_{eq}$ is obtained as $q/\Delta T$, where $q$ is the power density in mW/$\mu$m$^2$.

Comparing Figure 5-6 with Figure 4-5, it reveals that devices No. 1, 3, and 4, the well-performed sensors, are bounded by the $\xi$=0.01 and $\xi$=0.05 theoretical curves. The $k_{eq}$ changes

from 10% to as high as 45% in these sensors when pressure changes from 101kPa to 800kPa. On the other hand, the experimental results for sensor No.2 lie close to the 50% solid contact area ($\xi$=0.5) theoretical curve and has very poor sensitivity. The reason for the device having 50% solid contact area is still under investigation. Some speculations are that the resistor is not totally released (incomplete undercut of the oxide layer), or there is still water in the gap, etc.

The theoretical results are therefore consistent with the experimental data. This is the main discovery of our research. If the gap is small enough, even though the heater collapses and makes contact with the substrate, the sensor can still measure pressure well above 1atm (101kPa) with satisfactory sensitivity if the contact area is small. It is not necessary to keep the heater straight and avoid the contacts between the heater and heat sink for a high cost. This discovery lays a foundation for the design of a low-cost pressure sensor measuring atmospheric pressure with moderate precision.

From the above discussions, it is desirable to have large air gap area and a large $G_V/G_H$ ratio. Long, wide and thin polysilicon beams are likely to perform well.

## 5.3 Transition Pressure

Another discovery of our research is the prediction for the transition pressure by (2.8), $P_{tr} = \frac{2K_N}{\mathrm{Pr}}\left(\frac{2\gamma}{\gamma+1}\right)P$. In the previous work, the transition pressure is simply determined by the experimental data [4, 15], or is the pressure when $K_N$ is 1 [12, 34]. From (2.8), $P_{tr}$ is the pressure when $K_N$ is 1/2 in ideal conditions ($Pr$=1 and $\gamma$=1). It means that the sensor can respond to pressure till $\lambda=d/2$, twice the number believed before. Equation (2.8) proved that the transition pressure is solely determined by the gap distance $d$. And this discovery can be used in the sensor design to determine the gap or the measurement range of the sensor.

## 5.4 Heater Power Density Effects

The data in Figure 4-7, $V_{diff}$ vs. pressure with different heater power densities for sensor No. 1 are analysed to investigate the power density effects for the sensor performance. The results are shown in Figure 5-7 with the thermal conductivity $k_{eq}$ versus pressure for different values of heater power density $q$. For a fixed pressure, the change in $k_{eq}$ is relatively small for changes in power density $q$. Therefore a change in heater power density primarily affects the detected bridge voltage and the change in thermal conductivity is secondary.

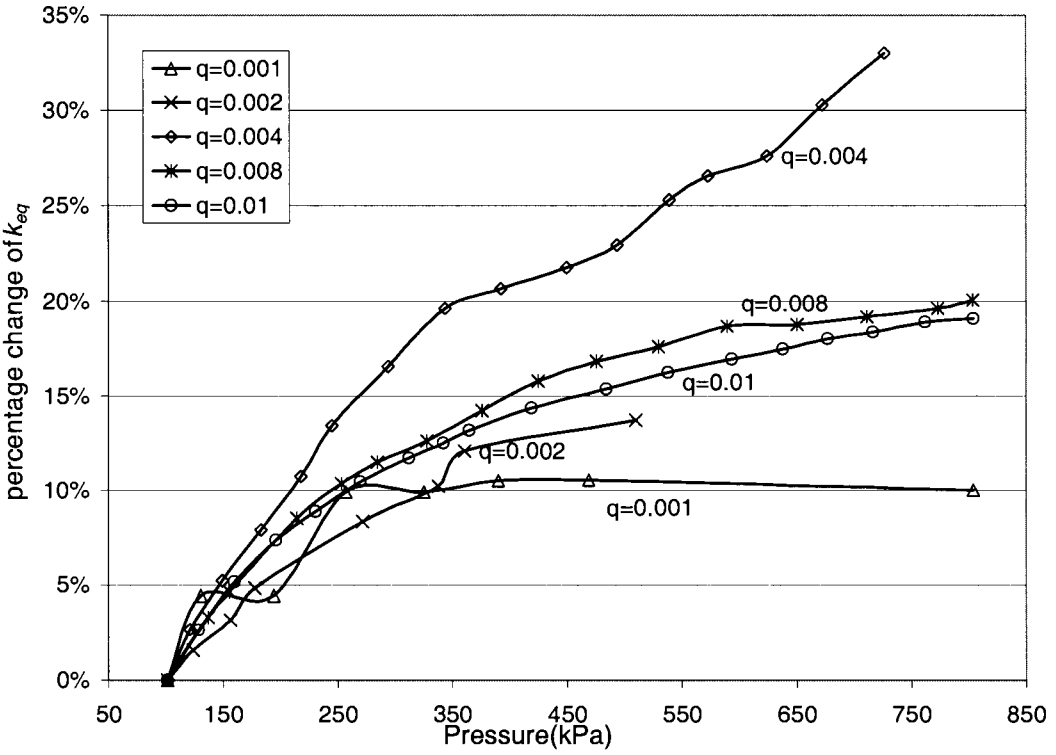


**Figure 5-7 Change in $k_{eq}$ vs. pressure for different power densities for sensor No.1**

The sensitivity to changes in heater power density is consistent with the sensor operation based on Joule heating and thermal conduction. When the heater power density is too low, the temperature of the polysilicon resistor is low, the change in resistivity due to pressure is correspondingly low, and conduction losses are small. A minimum heater power density is required for a minimum sensor sensitivity specification. The upper limit on heater power density

is set by the maximum dissipation of the polysilicon resistor as well as the breakdown voltage of the native oxide grown on the gap.

## 5.5 Error Source

Ambient temperature drift, gas flow, and gas type introduce errors in the sensor. These errors are discussed next.

### 5.5.1 The Effects of Ambient Temperature Drift

In the sensor, it is not the temperature of the heater alone but the temperature difference between the heater and the reference temperature that determines the measurement accuracy. In the above discussions, the ambient temperature around the sensors is used as the reference temperature and considered constant over the measurement. Actually the real reference temperature should be the temperature of the heat sink (the substrate). If there are temperature differences between the temperature at the heat sink and the ambient temperature, or the ambient temperature changes, the measurement accuracy is directly affected. Bridge structures, dummy resistors and signal processing can compensate for ambient temperature drift.

The following calculation gives an example of the temperature drop from the heat sink to the ambient temperature for a single heater.

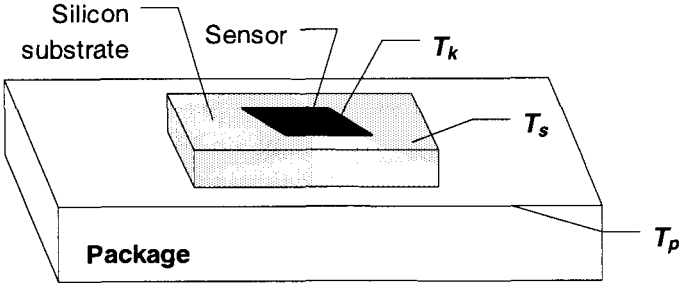


**Figure 5-8 Calculation of reference temperature error**

In the structure shown in Figure 5-8, the temperature of the heat sink, $T_k$, is the 'real' reference temperature. The temperature of the package $T_p$ is the 'used' reference temperature in

the calculation and considered the same as the ambient temperature. The temperature drop from $T_k$ to $T_p$ is the sum of two other temperature differences: the temperature difference from the heat sink $T_k$ to the substrate $T_s$, and the temperature difference from the substrate $T_s$ to the package $T_p$.

The temperature drop introduced by the silicon substrate from the heat sink to the back of the die is $\Delta T = qs/k$, where $q$ is the power density, $k$ is the thermal conductivity of bulk silicon (150 W/m K), and $s$ is the thickness of substrate, about 600$\mu$m. The temperature drop $\Delta T$ is 0.01°C when $q$=2.5×10$^3$W/m$^2$ (heating power=10mW with chip area as 2mm×2mm).

The second temperature drop is from the back of the die to the ambient through the package. The package used in our research is a ceramic 16-pin dual-in-line package (DIP) with a thermal resistance from junction to ambient of $\theta_{JA}$=70°C/W. For a typical die with active area A=1000$\mu$m$^2$ and power density q=0.01mW/$\mu$m$^2$, the temperature drop from the junction to the ambient is $\Delta T = qA\theta_{JA}$ =0.7°C.

So from the heat sink where the 'real' reference temperature is taken to the ambient temperature at which pressure is measured, there is an extra temperature drop of about 0.7C for a power density of 0.01mW/$\mu$m$^2$. For a single heater, the actual reference temperature is 0.7°C higher than the measured reference temperature used in the calculation. For a bridge structure with differential measurements, the common mode temperature changes (like the drift of the ambient temperature) are cancelled in the output. Only the differential resistance changes of the two heaters that results from pressure variations is measured.

However, if the Wheatstone bridge is not perfectly balanced, the ambient temperature drift will eventually affect the measurement of the gas thermal conductivity.

### 5.5.2 Gas Flow and Gas Type

The sensor principle is based upon the heat loss of the heater to its substrate through thermal conduction of gases. Anything that affects this mechanism will affect the sensor performance. For example, if there is air moving over the sensing element, the heat loss mechanisms will be changed; errors are introduced into the measurements.

Changes of the composition of the air also introduce errors. The continuum value of the thermal conductivity is not identical for different gases because of the different sizes of the gas molecules. The value of thermal conductivity for most gases and vapours ranges between 0.01 and 0.03 W/m K at room temperature and atmospheric pressure. Notable exceptions are helium (0.15 W/m K) and hydrogen (0.18 W/m K) [4].

Sensor errors resulting from gas flows and changes in gas types are not analysed in this work, and are recommended for future research activities.

# CHAPTER 6 CONCLUSION

## 6.1 Achievements

An innovative short-distance thermal conduction pressure sensor fabricated by surface micromachining technique has been presented in this thesis. The advantages of the new device over other existing devices are the simple and inexpensive fabrication procedure, and the capability of measuring higher pressure.

The working principles and the design options of the sensor have been thoroughly examined. Extensive surveys of the existing similar sensors have been conducted to help optimising the design. Design considerations like the selection of the material and the operating mode have been addressed. A fabrication procedure has been put together to produce functional devices inexpensively. Devices fabricated with a three-mask, 3μm and CMOS compatible process have been tested on its sensitivity, linearity, power effects and operating range. Preliminary test results demonstrate the potential for a commercial adaptation.

An analytical model was developed to describe the device behaviour based on its simplified representations. The model demonstrates the quantified relationship between the solid contact area of the resistor and the performance of the sensor. Higher sensitivity associates with less solid contact areas. Theoretical boundaries have been derived to predict that sensors with solid contact areas less than 5% of the whole resistor area perform better. The output voltage of the Wheatstone bridge changes from 10% to nearly 50% over pressure range form 100kPa to 800kPa for these sensors. Experimental results correlate well with the theoretical analysis.

The device's response has some variations from linearity. Two major contributing factors to the non-linearity are the pressure-independent solid thermal conduction and the pressure-

dependent Knudsen number effect. The solid thermal conduction is determined by the solid contact area and is approximately constant over the measurement range. The Knudsen number effect is caused by the decrease of the molecular MFP with rising pressure, and is more significant at the high end of the pressure.

The device's sensitivity was evaluated from its calibration curves. Experimental data demonstrate that the device's sensitivity increases with the heating power. A sensitivity of 30mV/V/kPa was measured for a power density of $0.008mW/\mu m^2$. The relationship of the transition pressure with the gap distance has been established. The predicated value for transition pressure from the equation is consistent with the experimental results.

One of the promising applications of the new pressure sensor is in automotive industry. For example, the new device can be used as a durable and inexpensive sensor in the tire pressure monitoring system, which amounts to 500 million dollars in North America market in 1998 [26]. The automotive industry is the largest customer for micromachined silicon sensors with pressure and acceleration sensors make the biggest share. Pressure sensors are the most mature silicon-micromachined devices commercially available today, they are available in range from fractions of 1psi (6.89kPa) all the way to 15,000psi (103MPa) and the costs have come down dramatically [26].

Two major manufacturing options are available: bulk micromachining in single crystal silicon and surface micromachining in polysilicon [26]. The polysilicon surface micromachined pressure sensors are more compatible with regular IC process than bulk micromachined sensors. The advantage of polysilicon sensors is low-cost. For applications requiring moderate accuracy, polysilicon represents the least costly solution today [26]. However the difficulty in controlling polysilicon properties in different laboratories may prevent it achieving long-term accuracy and repeatability.

## 6.2 Future Work

Future work will focus on the optimisation of the design and process flow to get better controllability for the process and better performance for the device.

The process-dependent properties of polysilicon thin film and the randomness of the contact points between the heater and heat sink make the sensor's output hard to predict and repeat. The device-to-device variations may require individual calibration for each device, which increases the fabrication cost. One solution is to use on-chip signal process circuits. The device variation and the non-linearity will both be compensated.

The wet etching process to release the structure is hard to control and takes a long time. Better process control and optimised design may alleviate this problem. For example, making the resistor narrower will reduce the etching time.

The constant-temperature (CT) operating mode can be employed for more accurate temperature measurement and better control of the device. A separated temperature sensor like a thermocouple or thermopiles can be added to measure the heater's temperature directly. A thermocouple is more stable than a temperature sensor made by polysilicon resistor in a long term.

Much work is needed to address the repeatability and long-term stability of the device. Contaminations from the environment may block the tiny air gap or attach to the polysilicon surface and change the thermal behaviour of the sensor. Besides, native oxide will continue to grow on the surfaces of the polysilicon and silicon in the gap, the influence to the sensor is still unknown. Will the bridge structure collapse further to the substrate with repeated pressure cycling and how it affects the performance of the sensor? These are some of the questions that need to be answered in the future work.

# APPENDIX A
# ORIGINAL DESIGN FILES (THE FOURTH RUN)

The design files of the fourth run are listed as follows.

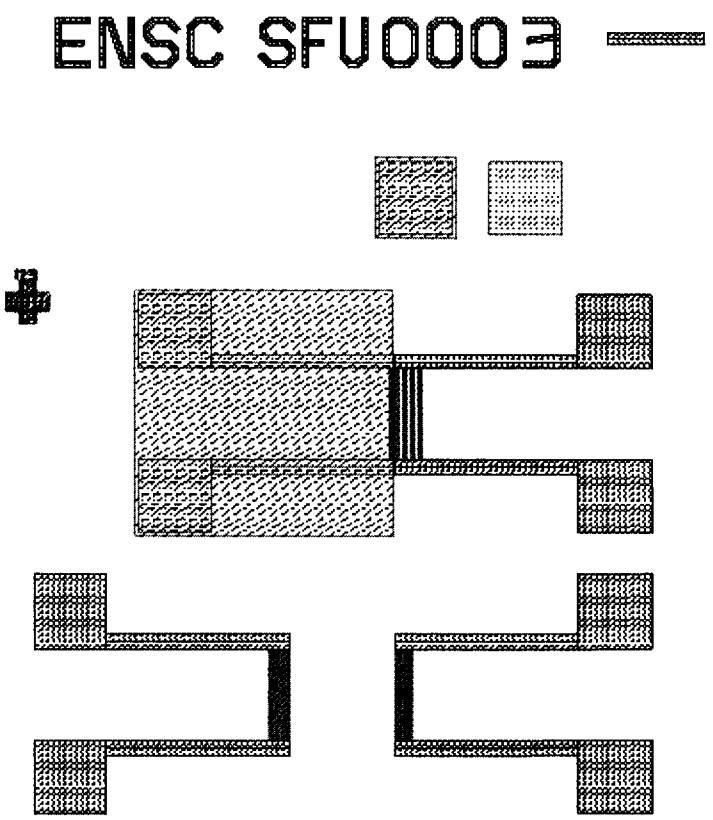


**Figure A-1 Design pattern 1 of the fourth run**

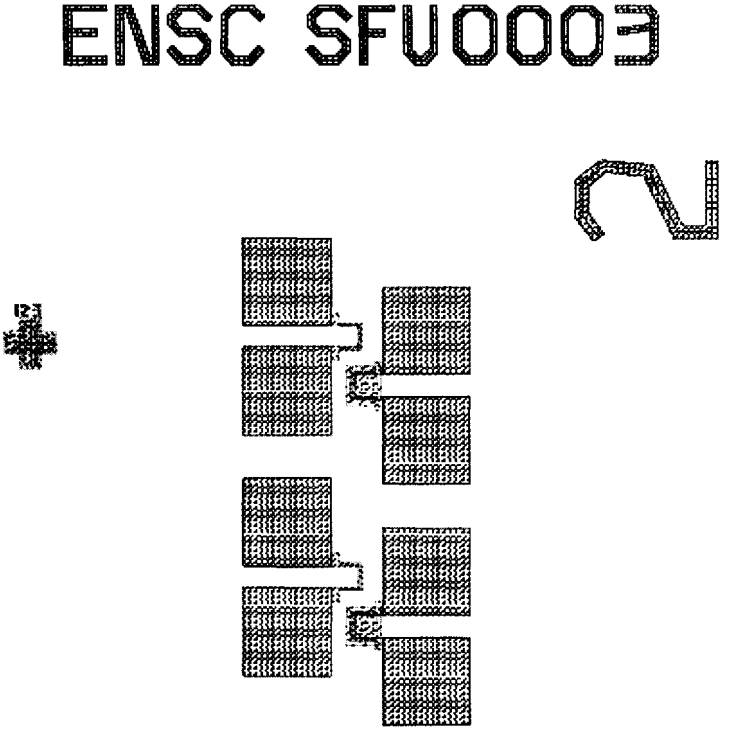


**Figure A-2 Design pattern 2 of the fourth run**

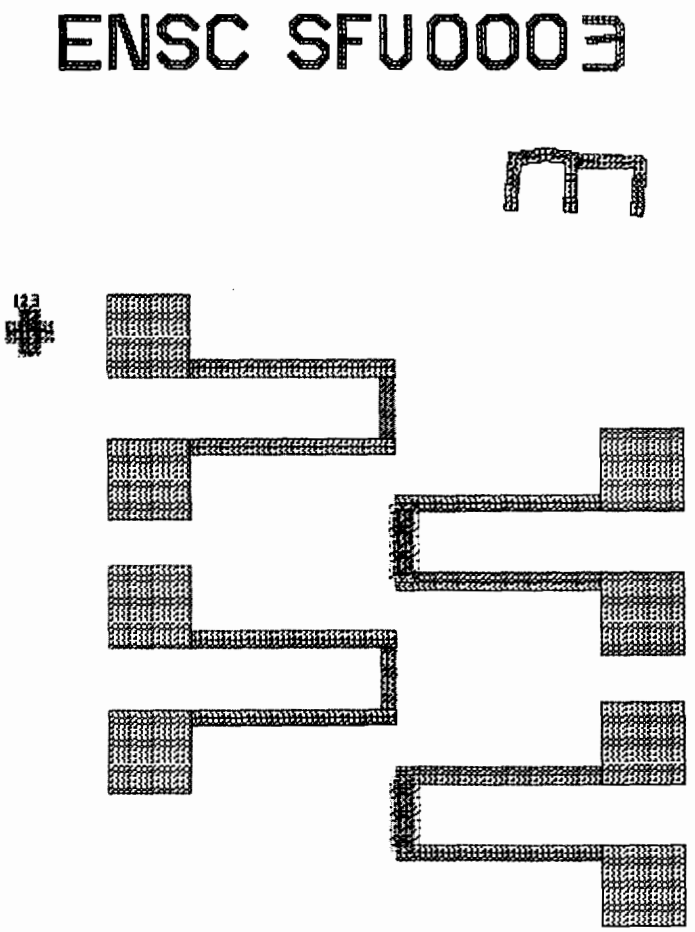


**Figure A-3 Design pattern 3 of the fourth run**

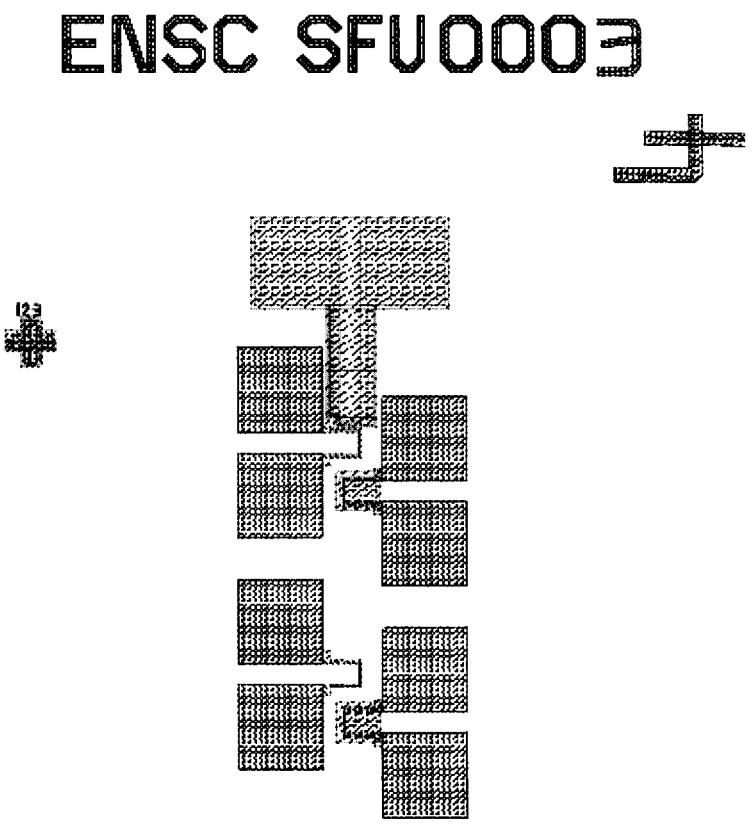


**Figure A-4 Design pattern 4 of the fourth run**

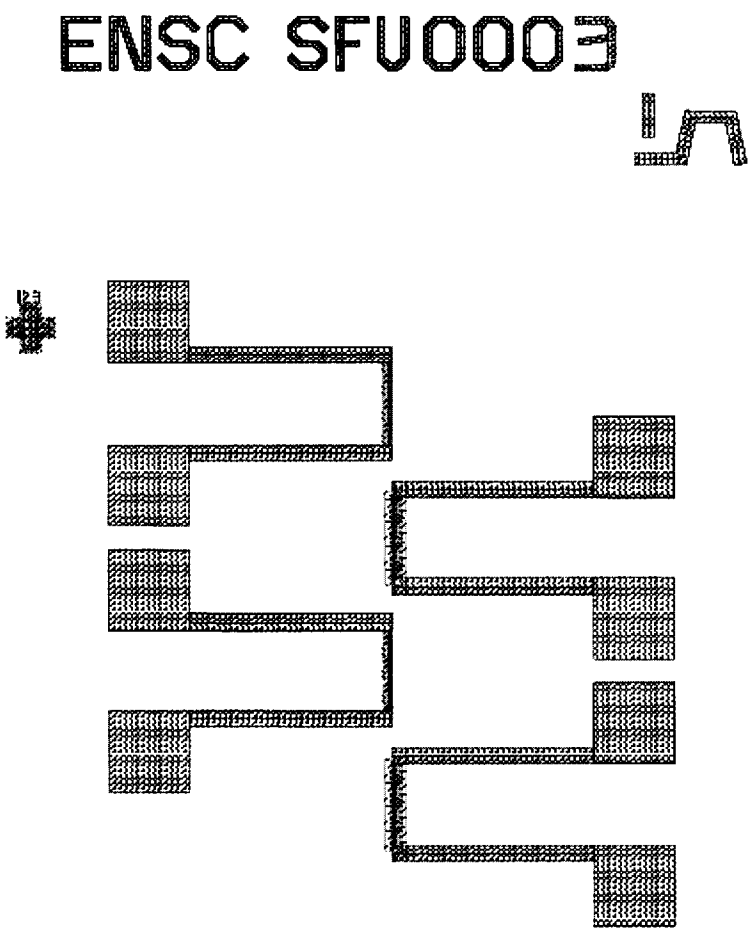


**Figure A-5 Design pattern 5 of the fourth run**

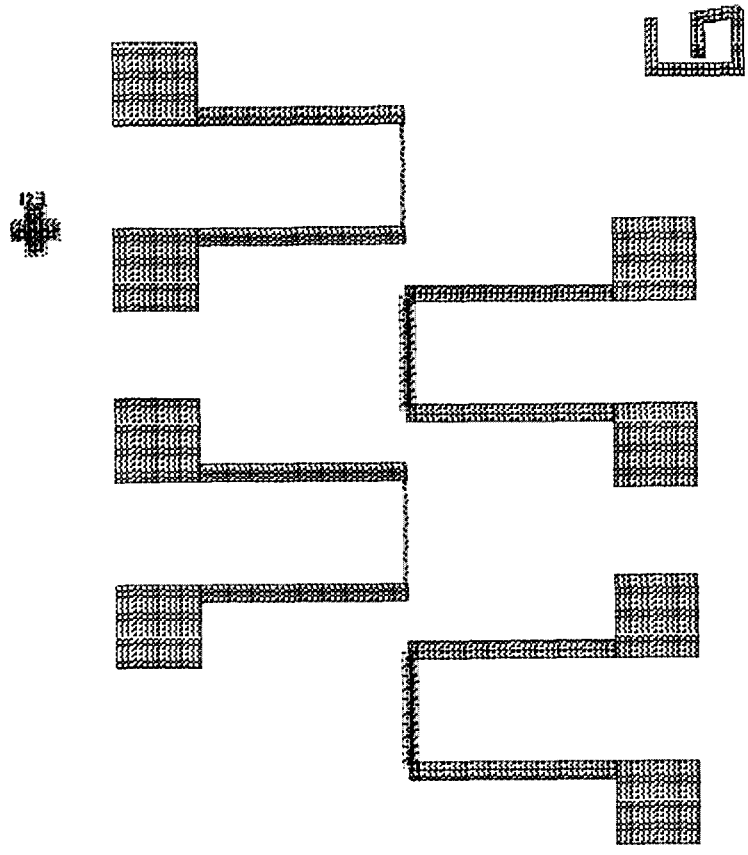


**Figure A-6 Design pattern 6 of the fourth run**

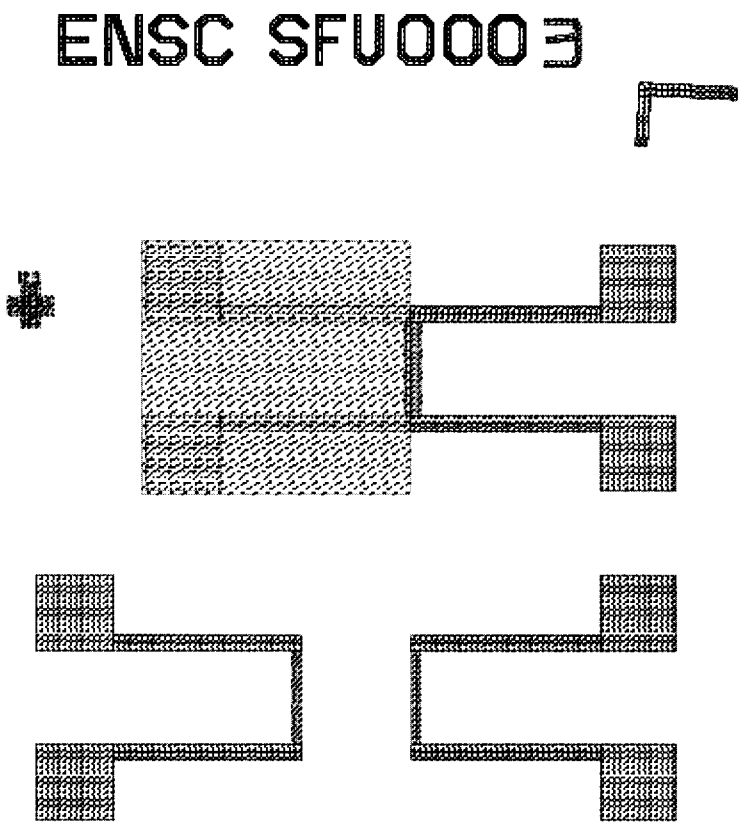


**Figure A-7 Design pattern 7 of the fourth run**

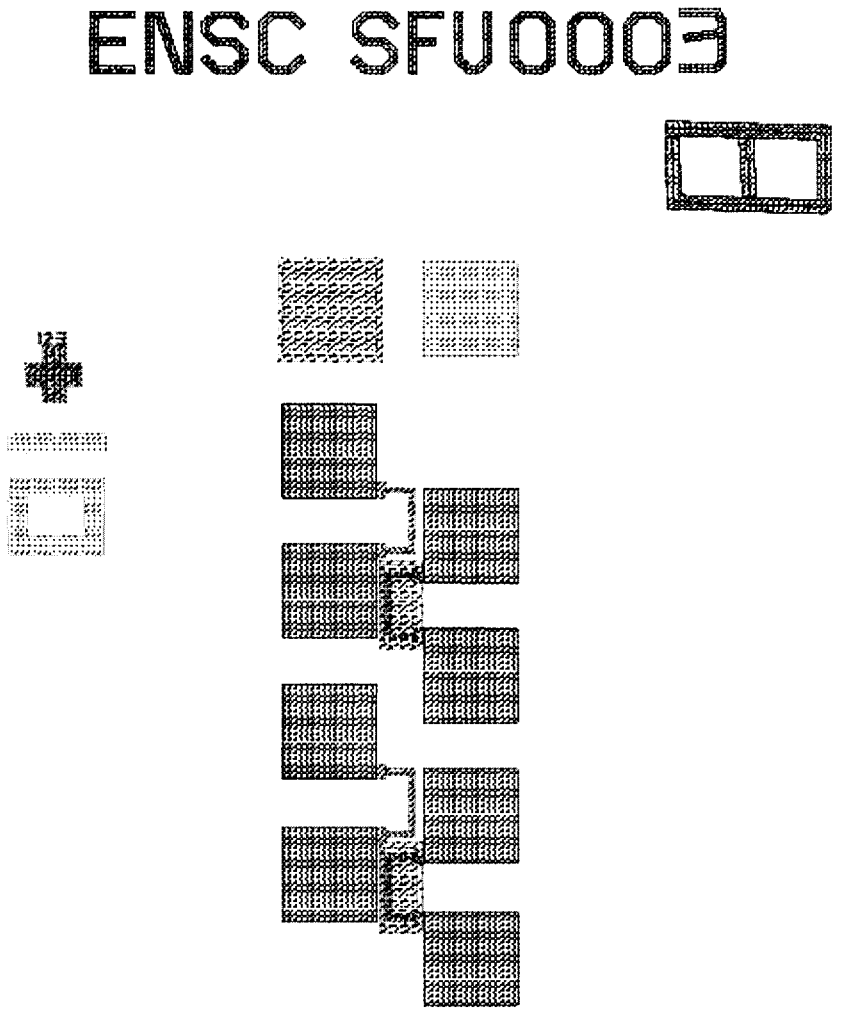


**Figure A-8 Design pattern 8 of the fourth run**

# APPENDIX B
# FABRICATION PROCEDURE

The final procedure is as follows:

1. Pre-bake wafer in the oven at 120°C for 1 hour

2. **Mask1**: define polysilicon structure.

   a. Spin on primer (help adhesion of the photoresist):

      4000rpm for 30s and bake 1min at 100°C

   b. Spin on photoresist:

      4000rpm for 30s and bake 25min at 100°C

   c. Expose: P=30mW; $\lambda$=314nm; t=10s; UV

   d. Develop: time varies; MF319 developer

   e. Postbake: 20min at 120°C

   f. Etch $SiO_2$: 2m30s using BOE at room temperature

   g. Strip photoresist: $SiO_2$ becomes the etch mask for Poly

   h. Etch Poly: using EDP at 95°C for 47s

3. **Mask2**: define oxide

   Prebake: 75m at 120 °C

   Repeat step2 a, b, c, d and e,

   Etch Oxide: BOE, 2m

4. Al sputtering deposition (Al thickness 1$\mu$m)

   Aluminium was deposited using a DC magnetron plasma sputtering machine

5. **Mask3:** define Al

   Repeat step 2 a, b-Primer, photoresist, exposure time 8s

   Etch Al: BOE, time varies

   Acetone clean

   Anneal Al at 475°C for 30min

6. Etch Oxide, release beams

   Etchant: 30ml Glycerol mixed well with 50ml BOE

   Time: 80-100mins

7. Rinse the finished wafer in deionized water to clean the etchant and promote the growth of natural oxide

8. Once the structures were released, the chip was wire bonded, packaged and ready for test.

# APPENDIX C
# SUMMARY OF THE FOUR DESIGN RUNS

Summary of all the test runs
All packages are 16-pin DIP

Test: No.0 (pre-run); Date: Jun. 13, 2000

| |
|---|
| 10μm, 20μm lines were designed and exposed for 10s, 20s and 30s, respectively. After develop, the line width was checked. It was concluded that the results for 10s exposure time were better. Same method was used to determine the best etch time. |

Test: No.1; Date: Jun. 14, 2000; One mask is designed with only released resistor

| **Design** | **Process/Test** | **Comments** |
|---|---|---|
| Different structures included bridge and, cantilever, and various sizes of the resistors were tried out.<br><br>Line widths varied from10μm, 20μm and 50μm; lengths were from 100μm, 200μm, 2000μm to 3000μm; | This design is mainly used to test the process and the feasibility of the design. Only one mask was used to define poly.<br><br>Poly was used as the bonding pad and conductive glue (epoxy) was used to glue the wire to the poly bonding pad.<br><br>Six devices were packaged (3 for 10μm line width and 3 for 20μm) | Wafer cut is good, glue part is tricky.<br><br>2. The resistance kept changing. Breaking down the oxide did not help. Devices were unstable.<br><br>3. It was concluded that the property of the epoxy and its dependence of temperature made it not suitable for the work. The solution was to use metal as the bonding pad. |

Test: No.2; Date: Jun. 21, 2000; Two-mask design with only released resistors

| **Design/Package** | **Process/Test** | **Comments** |
|---|---|---|
| Mask 1 is the same as the 1st run; mask 2 is added for Al as the bonding pad.<br><br>Used the wafer left from 1st run;<br><br>Package 6 devices (2 for released 10μm line; 2 for released 20μm line; 2 for unreleased 20μm line | In the last step of BOF etching to release the structure, the whole wafer was cut into half. The first half was etched with BOF. For 12mins, the photoresist began to lift off and clearly Al was not going to stand till the end.<br><br>Using the new etchant discussed in the thesis to protect Al while etching oxide, it took 82mins to release the structure, including the first 12mins.<br><br>Etching the second half wafer took 100mins. | The basic test procedure is to check the resistance change of the poly resistor.<br><br>With constant voltage, a current meter was used to measure the current flowing through the resistor. The resistance was calculated from Ohm's law. The sensor was tested under normal air pressure, vacuum and compressed air in the dark room. Its thermal resistance was tested in the oven. The result was encouraging; thermal conductance had an 85% change when pressure changed from 14.7psia to 147.7psia.<br><br>Encouraged by the results, we decided to try bridge structure with 4 resistors, 2 released and 2 unreleased connected as Wheatstone bridge for improvement. |

Test: No.3A; Date: July. 24, 2000; Two-mask for Wheatstone bridge design

| Design/Package | Process/Test | Comments |
|---|---|---|
| There were 2 heaters plus 2 dummy resistors in the same chip that could be tested as a Wheatstone bridge.<br><br>Al was used as the bonding pad and etch mask for the unreleased part.<br><br>6 devices packaged | 10μm and 20μm lines were designed from the previous experience.<br><br>The length of the beam varied from 250μm, 750μm to 900μm.<br><br>As before, one wafer was cut into two halves.<br><br>Different develop and etch time were tried. | The resistance of the unreleased part was too small because Al attached to poly and changed the resistance. This adversely affected test results.<br><br>Conclusion: had to refine the design; add one more mask to protect the oxide above the unreleased poly resistor, so Al would change the resistance of unreleased resistor. This would make the bridge more balanced. |

Test: No.3B; Date: Aug. 2, 2000; Three masks: poly, oxide and Al

| Design/Package | Process/Test | Comments |
|---|---|---|
| 6 devices packaged (2 for each design- different length of the beams (250μm, 750μm and 900μm)) | | Results were good. |

Test: No.4; Date: Oct. 18, 2000; Three masks, multi-finger design

| Design/Package | Process/Test | Comments |
|---|---|---|
| The number of fingers is 1, 2 and 4; the widths of the lines are 6μm, 8μm and 10μm and the spaces between the fingers would be 2μm, 5μm and 10μm. There are several combinations, like 10μm wide line would have 2μm, 5μm and 10um space and 1, 2 and 4 fingers, total pattern is 8.<br><br>24 devices packaged | Oxide breakdown, the thermal resistance for the released and unreleased resistors were measured. All the chips in bridge were tested. If worked well it would be subject to a through test, all individual resistors would be tested. | Chips with multi-finger didn't outperform the ones in 3B, actually fingers made etching oxide more difficult. |

Table C.1 Summary of the devices in the third run

| ID | Design (width×length) | Actual Width (um) | Area (um²) | R1 (Ω) | R3 (Ω) | R2 (Ω) | R4 (Ω) | Test result |
|---|---|---|---|---|---|---|---|---|
| 1 | 10×750 | | | 1739 | 1529 | 1746 | 1734 | not very well, readings always change |
| 2 | 10×750 | 4.55 | 3412 | 1263 | 1276 | 1237 | 1252 | OK |
| 3 | 10x250 | 6.72 | 1680 | 407 | 405 | 409 | 401 | Very good |
| 4 | 10x250 | | | 443 | 443 | 445 | 402 | good |
| 5 | 10×900 | | | 1849 | 1887 | 1631 | 1092 | Not good |
| 6 | 10×900 | | | 2160 | 2240 | 2310 | 1983 | Not good, not stable |
| 31 | 10x250 | | | 426 | 423 | 425 | 428 | OK |
| 32 | 10x250 | | | 567 | 594 | 571 | 556 | |
| 33 | 10x250 | | | 357 | 361 | 327 | 357 | |
| 34 | 10x250 | | | 428 | 430 | 459 | 463 | |
| 35 | 10x250 | | | 504 | 501 | 501 | 496 | |

Table C.2 Summary of the devices in the forth run

| ID | Design (width×length×finger ) | Width (um) | Area ($um^2$) | R1 (Ω) | R3 (Ω) | R2 (Ω) | R4 (Ω) | Test result |
|---|---|---|---|---|---|---|---|---|
| 4.1.1 | 10×250×4 | 6.05 | 6050 | 3.2 | 179.9 | 176.4 | 178.9 | temp sensor not working |
| 4.1.2 | 10×250×4 | 6.05 | 6050 | 3.3 | 178.6 | 185.2 | 182.6 | only one test |
| 4.2.1 | 6×150×1 | 2.60 | 390 | 945 | 937 | 609 | 1120 | not good |
| 4.2.2 | 6×150×1 | 2.95 | 442.5 | 1174 | 788 | 621 | 921 | device damaged |
| 4.3.1 | 6×150×4 | 2.05 | 1230 | 368 | 361 | 365 | 369 | good |
| 4.3.2 | 6×150×4 | 2.40 | 1440 | 247 | 271 | 270 | 277 | not good |
| 4.3.3 | | | | 219 | 220 | 180.7 | 192.7 | |
| 4.3.4 | | | | 652 | 631 | 575 | 622 | Ok, but not enough test |
| 4.4.1 | 8×200×1 short | 4.35 | 870 | 859 | 657 | 320 | 155 | |
| 4.4.2 | 8×200×1 short | 2.55 | 510 | 1344 | 1420 | 208 | 256 | |
| 4.5.1 | 8×200×2 | 4.30 | 1720 | 789 | 398 | 413 | 395 | |
| 4.5.2 | 8×200×2 | 4.15 | 1660 | 467 | 454 | 427 | 442 | good |
| 4.5.3 | | | | 477 | 458 | 443 | 456 | |
| 4.5.4 | | | | 399 | 401 | 394 | 409 | OK, but only one test |
| 4.6.1 | 10×250×1 | 3.65 | 912.5 | 957 | 1025 | 1037 | 991 | OK, probably need higher power |
| 4.6.2 | 10×250×1 | 3.75 | 937.5 | 706 | 714 | 325 | 330 | |
| 4.6.4 | | | | 1078 | 1039 | 1066 | 1057 | not good |
| 4.7.1 | 10×250×2 | 5.67 | 2833.33 | 3.7 | 387 | 376 | 383 | not test |
| 4.7.2 | 10×250×2 | 6.62 | 3308.33 | 4.5 | 320 | 340 | 328 | not test |
| 4.8.1 | 10×250×1 short | 4.25 | 1062.5 | 957 | 999 | 891 | 909 | good |
| 4.8.2 | 10×250×1 short | 6.25 | 1562.5 | 746 | 707 | 693 | 697 | |
| 4.8.3 | | | | 906 | 864 | 859 | 844 | good |
| 4.8.4 | | | | 722 | 722 | 695 | 717 | |
| 4.6.3 | | | | 736 | 725 | 306 | 762 | need higher power |

# APPENDIX D
# ADDITIONAL SEM PICTURES

The SEM pictures of the finished devices.

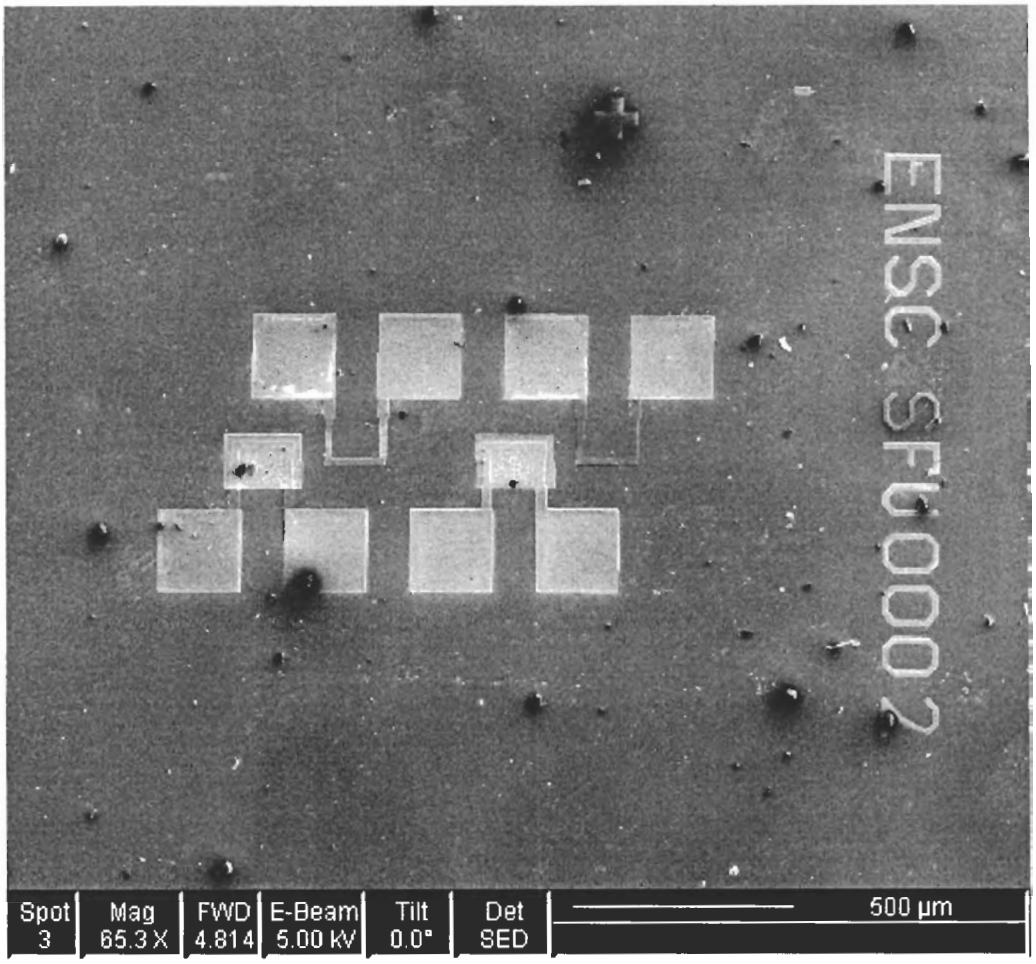


**Figure D-1 SEM of the device in third run**

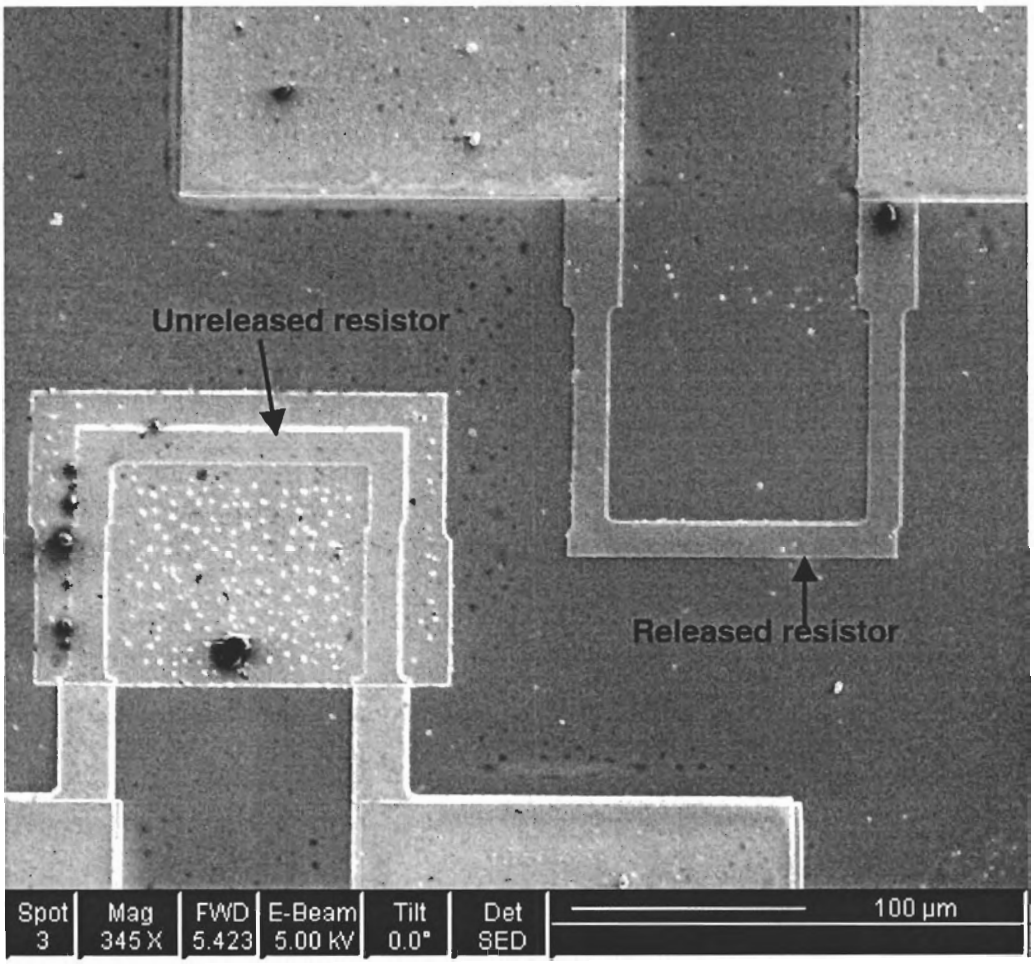


**Figure D-2 Two resistors of the device in third run**

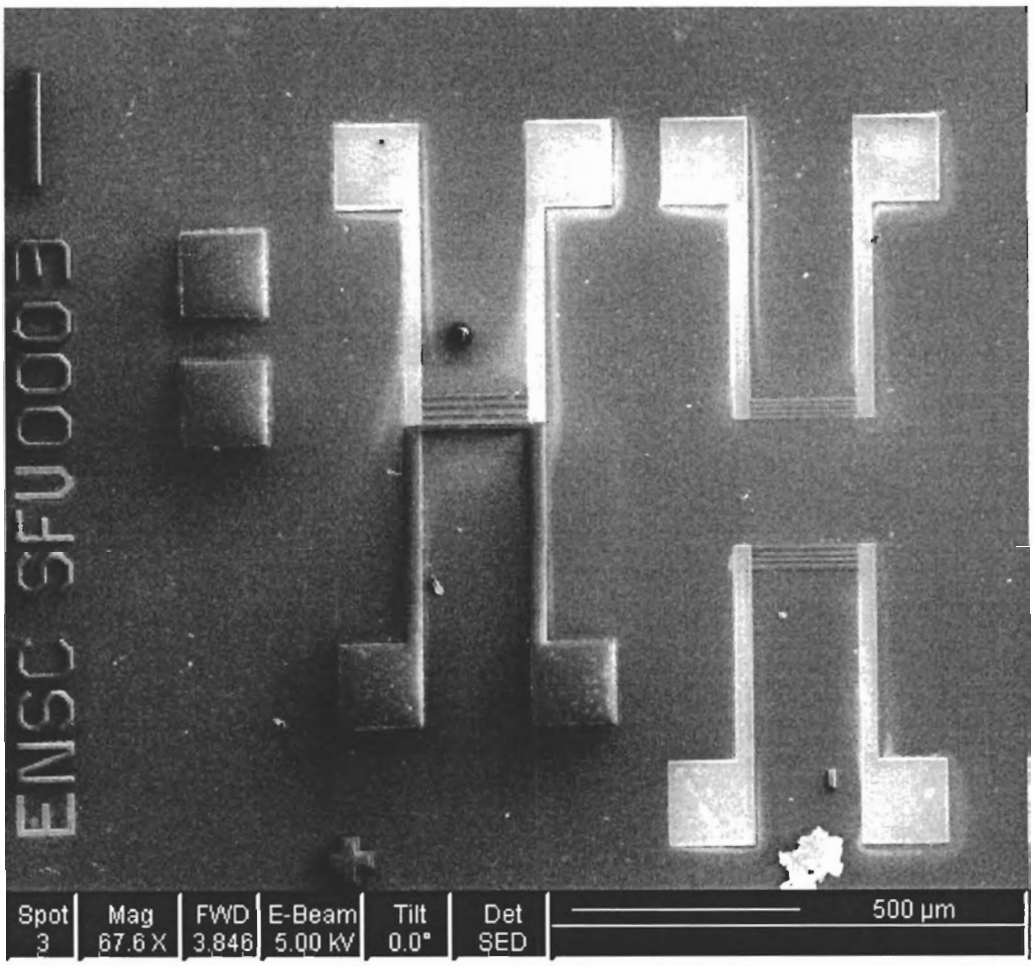


**Figure D-3 SEM of design pattern 1 in fourth run**

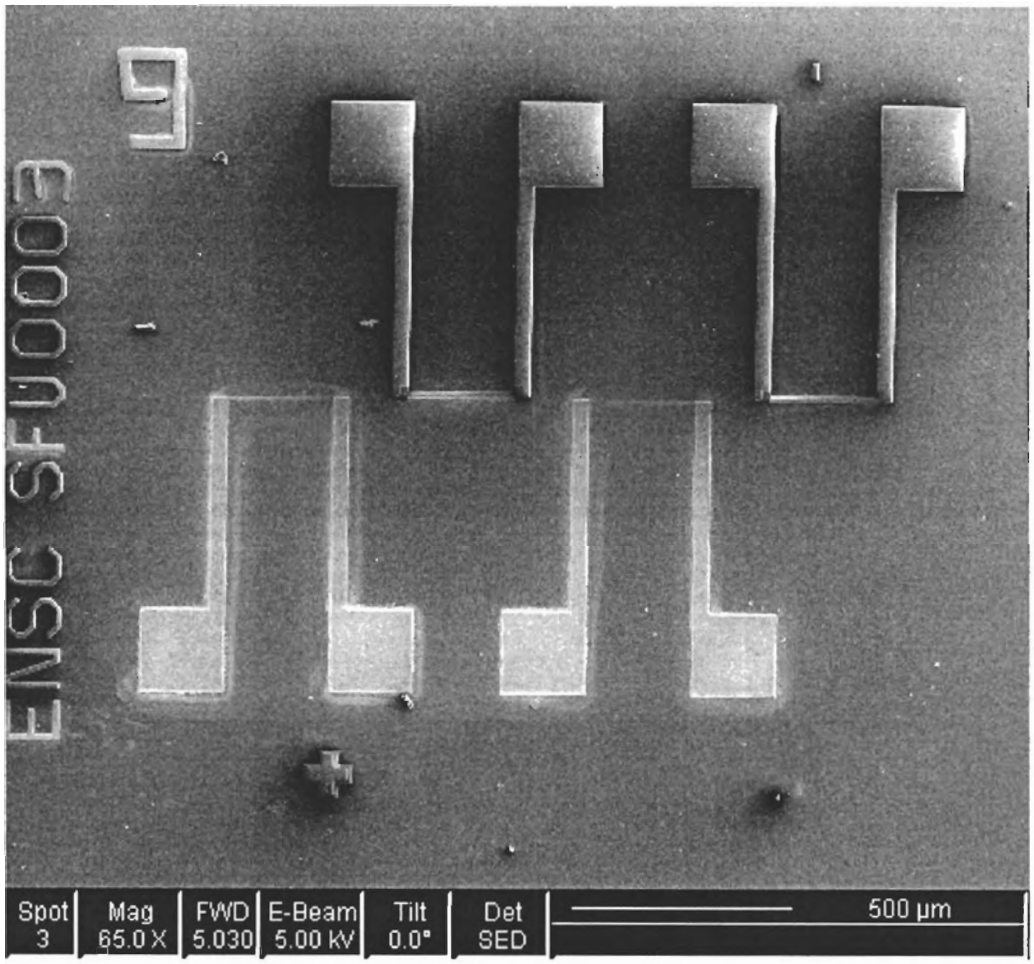


**Figure D-4 SEM of design pattern 6 in fourth run**

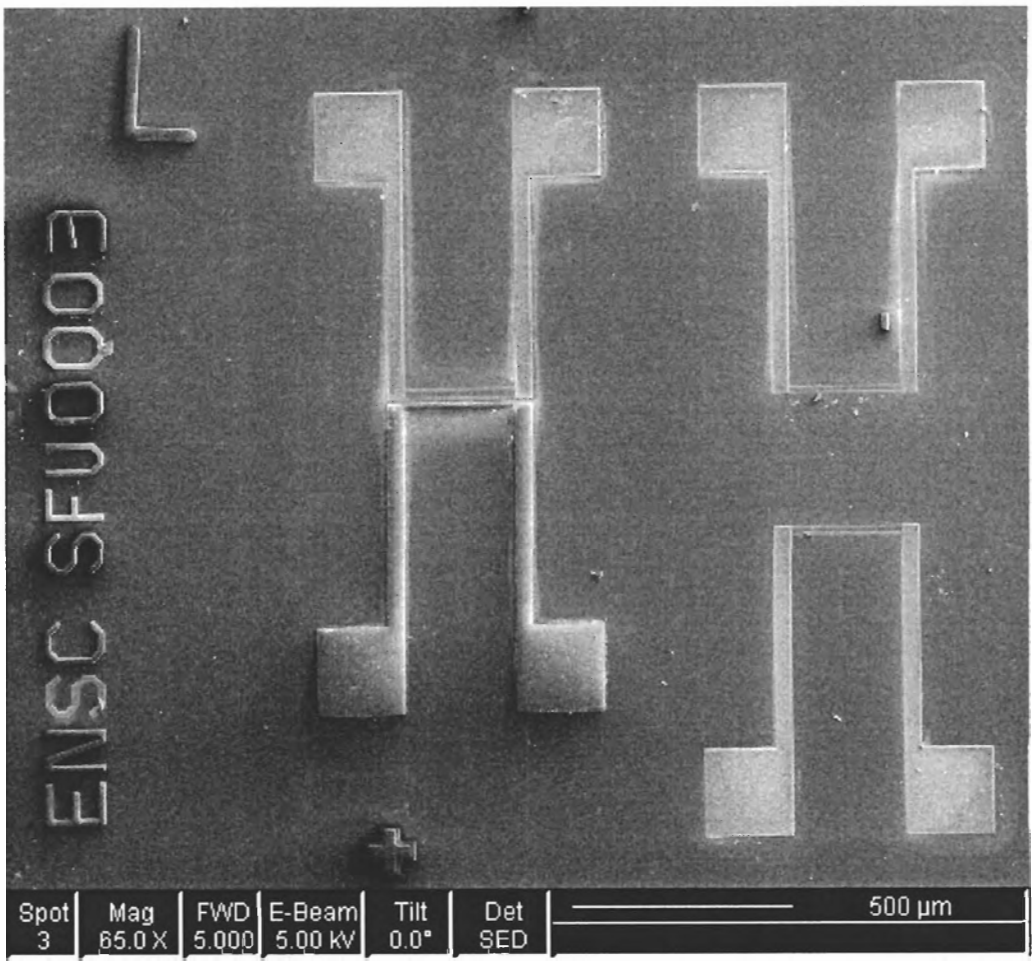


**Figure D-5 SEM of design pattern 7 in fourth run**

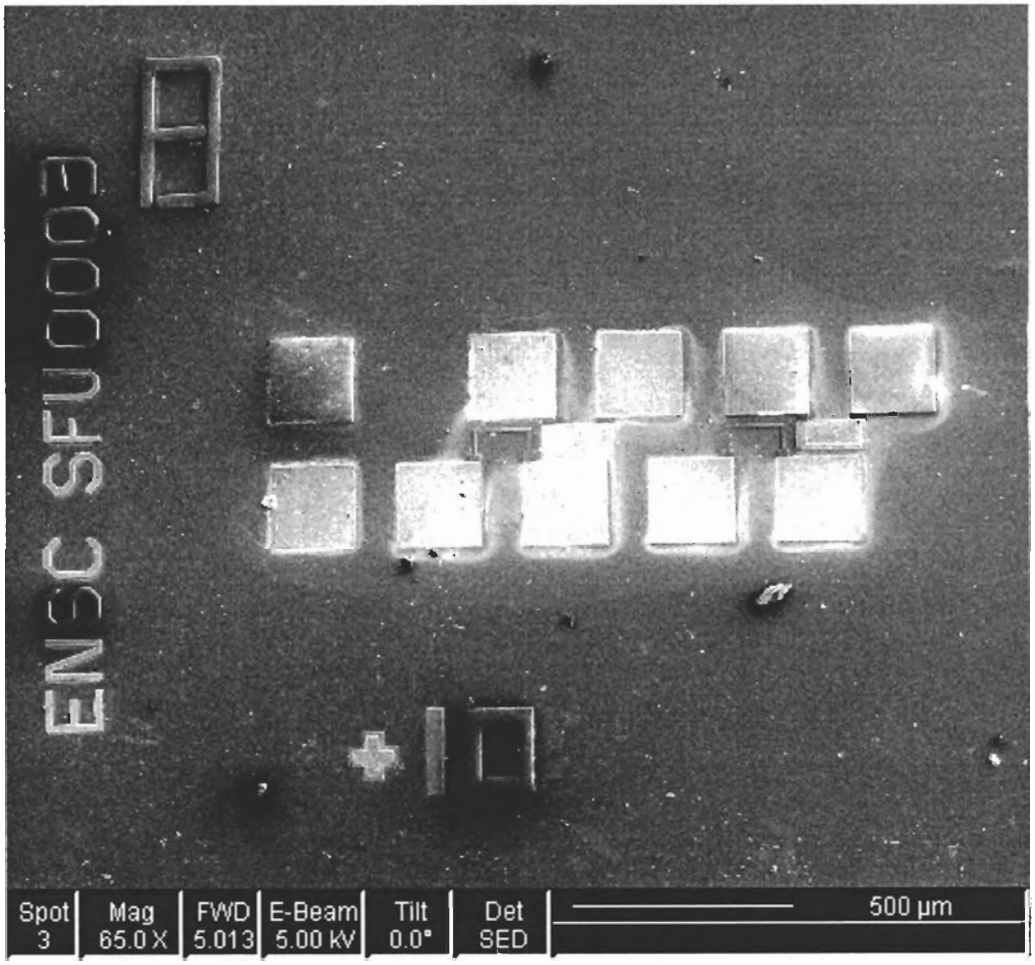


**Figure D-6 SEM of design pattern 8 in fourth run**

# APPENDIX E
# ANALYSIS OF A WHEATSTONE BRIDGE

## I. The Wheatstone Bridge

Bridge circuits are widely used for the measurement of resistance, capacitance, and inductance. The resistive bridge, also known as a Wheatstone bridge, is discussed in detail in the following section.

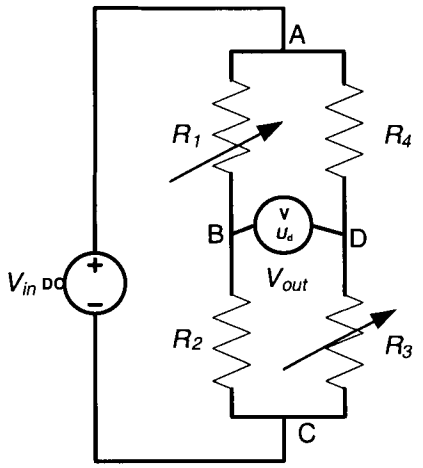


**Figure E-1 Wheatstone bridge circuit configuration**

## II.Basic Circuit

A basic Wheatstone bridge circuit contains four resistors, a constant voltage source, and a voltmeter, as illustrated in Figure E-1.

For a given input voltage $V_{in}$, the currents flowing through branches ABC and ADC depend on the bridge resistances,

$$V_{in} = V_{ABC} = V_{ADC} \Rightarrow I_{ABC}(R_1 + R_2) = I_{ADC}(R_4 + R_3) \tag{E.1}$$

The voltage drops from A to B and from A to D are given by

$$V_{BC} = I_{ABC}R_2 = \frac{V_{in}}{R_1 + R_2}R_2 \tag{E.2}$$

and

$$V_{DC} = I_{ADC}R_3 = \frac{V_{in}}{R_3 + R_4}R_3 \tag{E.3}$$

The output voltage $V_{out}$ is

$$V_{out} = V_{BC} - V_{DC} = \frac{R_2R_4 - R_1R_3}{(R_1 + R_2)(R_3 + R_4)}V_{in}. \tag{E.4}$$

Let $A = R_2R_4 - R_1R_3$ and $B = (R_1 + R_2)(R_3 + R_4)$, then

$$V_{out} = \frac{A}{B}V_{in} \tag{E.5}$$

Suppose all resistors change during the measurement, the corresponding change in output voltage is

$$V_{out} + V_{diff} = \frac{(R_2 + \Delta R_2)(R_4 + \Delta R_4) - (R_1 + \Delta R_1)(R_3 + \Delta R_3)}{(R_1 + \Delta R_1 + R_2 + \Delta R_2)(R_3 + \Delta R_3 + R_4 + \Delta R_4)}V_{in}. \tag{E.6}$$

## III. Balanced Circuit

If the bridge is initially balanced, the initial $V_{out}$ is zero. This yields the following relationship between the four resistors,

$$V_{out} = \frac{A}{B}V_{in} = 0 \Rightarrow R_1R_3 = R_2R_4$$

or

$$\frac{R_1}{R_2} = \frac{R_4}{R_3} = \frac{1}{r} \tag{E.7}$$

Use this result to simplify (E.6), $V_{diff}$ is

$$V_{diff} = \frac{r}{(1+r)^2}\left[\frac{\Delta R_1}{R_1} - \frac{\Delta R_2}{R_2} + \frac{\Delta R_3}{R_3} - \frac{\Delta R_4}{R_4}\right](1+\eta)V_{in} \tag{E.8}$$

where $\eta$ is defined by

$$\eta = \frac{1}{1 + \dfrac{1+r}{\dfrac{\Delta R_1}{R_1} + \dfrac{\Delta R_4}{R_4} + r\left[\dfrac{\Delta R_2}{R_2} + \dfrac{\Delta R_3}{R_3}\right]}}. \tag{E.9}$$

Moreover, when the resistance changes are small (< 5%), the second term in (E.9) is approximately zero.

$$V_{diff} \approx \frac{r}{(1+r)^2}\left[\frac{\Delta R_1}{R_1} - \frac{\Delta R_2}{R_2} + \frac{\Delta R_3}{R_3} - \frac{\Delta R_4}{R_4}\right]V_{in} \tag{E.10}$$

Equation (E.10) describes the basic operation of the Wheatstone bridge for a change in resistance. The coefficient $\frac{r}{(1+r)^2}$ is called the circuit efficiency.

## IV. Equal-Resistance Wheatstone Bridge

In practice, the four resistors are often selected to have the same value. If $R_1 = R_2 = R_3 = R_4 = R$, then $r = 1$, and the change in output voltage is simplified to,

$$V_{diff} \approx \frac{\Delta R_1 - \Delta R_2 + \Delta R_3 - \Delta R_4}{4R} V_{in}. \tag{E.11}$$

By carefully selecting the target and reference resistances, the Wheatstone bridge circuit can amplify small changes in resistance and/or compensate for changes in temperature.

In our designs, we tried to create matched bridge resistances, but there are small disparities introduced by the fabrication processes. Since we adopted the full bridge with two heaters and two dummy resistors, common mode temperature changes cancel out in the bridge. Only the temperature changes of the heaters that are pressure-dependent require consideration.

For heaters, though $\Delta R_1 \neq \Delta R_3$, we can assume $\Delta R_1/R_1 = \Delta R_3/R_3 = \Delta R/R$ because the two heaters are very close in the layout; for the dummy resistors, we assume $\Delta R_2 = \Delta R_4 = 0$. With these assumptions, the change in heater resistance is then equal to

$$\frac{\Delta R}{R} = \frac{\Delta R_1}{R_1} = \frac{\Delta R_3}{R_3} = \frac{AV_{in} - BV_{out}}{DV_{out} + 2R_1R_3V_{in}} \tag{E.12}$$

where $A = R_2R_4 - R_1R_3$, $B = (R_1 + R_2)(R_3 + R_4)$ and $D = 2R_1R_3 + R_1R_4 + R_2R_3$.

The temperature behaviour of the polysilicon resistor is generally described as

$$R = R_0[1 + \alpha(T - T_0)] \tag{E.13}$$

where $R_0$ and $\alpha$ are the resistance and TCR of the polysilicon resistor at the chosen reference temperature $T_0$, respectively,. The temperature rise ($\Delta T$) of the sensor referenced to the ambient temperature $T_0$, is

$$\Delta T = (T - T_0) = \Delta R/R_0/\alpha \tag{E.14}$$

where $\Delta R = R - R_0$. From (E.12) and (E.14), the value of $\Delta T$ is calculated, which is related to the change in thermal conductivity of air $k$.

# REFERENCES


1. S.D. James, R.G. Johnson and R.E. Higashi, "A Broad Range Absolute Pressure Microsensor", Proc. IEEE Solid-State Sensor and Actuator Workshop, pp.107-108, 1988
2. G.C.M. Meijer and A.W. Herwaarden, "*Thermal Sensors*", Institute of Physics Publishing, Bristol and Philadelphia,1996
3. Bruce C.S. Chou and Jin-Shown Shie, "An Innovative Pirani Pressure Sensor", Transducers '97, 1997 International Conference on Solid-State Sensors and Actuators, pp.1465-1468, 1997
4. R. Puers, S. Reyntjens and D. De Bruyker, "The NanoPirani--an extremely miniaturized pressure sensor fabricated by focused ion beam rapid prototyping", Sensors and Actuators A, Vol. 97-98, pp.208-214, 2002
5. Duane Tandeske, "*Pressure Sensors: selection and application*", Marcel Dekker Inc., New York, 1991
6. J.P. Holman, "*Heat Transfer*", 7th edition, McGraw-Hill, Inc., New York, 1990
7. H. Turnbull, R.S. Barton and J.C. Rivire, "*An Introduction to Vacuum Technique*", Grotge Newnes Limited, 1962
8. J. Baker, M.E. Calvert, D.J. Power, E.T. Chen, M.L. Ramalingam, and T.R. Lamp, "On the role of the Knudsen number with respect to heat transfer in micro-scale flows", Proceedings of the 31st Intersociety Energy Conversion Engineering Conference, Vol. 2, 11-16, pp.1396 – 1401, 1996
9. B. Gebhart, "*Heat Conduction and Mass Diffusion*", McGraw-Hill, Inc., New York, 1993.
10. C.V. Madhusudana, "*Thermal Contact Conductance*", Springer, 1996
11. M. Parameswaran, A. M. Robinson, Lj. Ristic, K. Chau and W. Allegretto, "A CMOS Thermal Isolated Gas Flow Sensor", Sensors and Materials, Vol. 2, Issue1, pp.17-26, 1990
12. Erno H. Klaassen and Gregory T. A. Kovacs, "Integrated thermal-conductivity vacuum sensor", Sensors and Actuators A, Vol. 58, Issue 1, pp.37-42, 1997
13. W. Van Herwaarden and P. M. Sarro, "Performance of integrated thermopile vacuum sensors", J. Phys. Instrum., Vol. 21, pp.1162-1167, 1988
14. W. Van Herwaarden, D. C. Van Duyn and J. Groeneweg, "Small-size vacuum sensors based on silicon thermopiles", Sensors and Actuators A, Vol. 27, Issues 1-3, pp. 577-581, 1991

15. Carlos H. Mastrangelo and R.S. Muller, "Microfabricated thermal absolute-pressure sensor with on-chip digital front-end processor", IEEE J. Solid-State Circuits, Vol. 26, No.12, pp.1998-2006, 1991

16. A.M. Robinson, P. Haswell, R. P. W. Lawson and M. Parameswaran, "A thermal conductivity microstructural pressure sensor fabricated in standard complementary metal-oxide semiconductor", Review of Scientific Instruments, 63 (3), pp.2026-2029, 1992

17. Ping Kuo Weng and Jin-Shown Shie, "Micro-Pirani vacuum gauge", Review of Scientific Instruments, 65 (2), pp.492-499, 1994

18. Jin-Shown Shie, Bruce C.S. Chou and Yeong-Maw Chen, "High performance Pirani vacuum gauge", The Journal of Vacuum Science and Technology A, 13 (6), pp.2972-2979, 1995

19. Oliver Paul and Henry Baltes, "Novel fully CMOS-compatible vacuum sensor", Sensors and Actuators A, Vol. 46-47, pp.143-146, 1995

20. W. J. Alvesteffer, D. C. Jacobs, and D. H. Baker, "Miniaturized thin film thermal vacuum sensor", The Journal of Vacuum Science and Technology A, 13 (6), pp.2980-2985, 1995

21. G. Grudin, A. Frolov, I. I. Katsan, and B. I. Lupina, "Thermal microsensor with a.c. heating for gas-pressure measurements", Sensors and Actuator, A, Vol.62, pp. 571-575, 1997

22. Gerlinde Bedo, Werner Kraus, and Rudolf Muller, "Comparison of different micromechanical vacuum sensors", Sensors and Actuators A, Vol. 85, pp.181-188, 2000

23. T. M. Berlicki, "Thermal vacuum sensor with compensation of heat transfer", Sensors and Actuators A, Vol. 93, Issue 1, pp. 27-32, 2001

24. N.T. Nguyen, "Micromachined flow sensors – a review," Flow Meas. Instrum., Vol. 8, pp.7-16, 1997

25. Roger T. Howe, Bernhard E. Boser and Albert P. Pisano, "Polysilicon integrated Microsystems: technologies and applications," Sensors and Actuators A, Vol. 56, pp.167-177, 1996

26. Marc Madou, "*Fundamentals of Microfabrication*", CRC Press,1997

27. W.A. Lane and G.T. Wrixon, "The design of thin-film polysilicon resistors for analog IC applications", IEEE Transactions on Electron Devices, Vol.36, No. 4, pp. 738-744, 1989

28. M.M. Mandurah, K.C. Sarawat, and T. I. Kamins, "A model for conduction in polycrystalline silicon-Parts I and II", IEEE Transactions on Electron Devices Vol. Ed-28, pp.1163-1176, 1981

29. S. Kumar and L. Bouknight, "Modelling of polycrystalline silicon thermal coefficient of resistance", IEEE International Integrated Reliability Workshop Final Report, pp.150 – 151, 1999

30. Angela D. McConnell, Srinivasan Uma, and Kenneth E. Goodson, "Thermal Conductivity of Doped Polysilicon Layers", Journal of Microelectromechanical Systems, Vol. 10, pp. 360-369, 2001

31. T. I. Kamins, "Design Properties of Polycrystalline Silicon", Sensors and Actuators A, Vol.21-23, pp.817-824, 1990

32. M. Parameswaran, H.P. Baltes, Lj. Ristic, A.C. Dhaded and A.M. Robinson, "A new approach for the fabrication of micromechanical structures", Sensors and Actuators, Vol. 19, pp. 289-307, 1989

33. Andrea Irace and P.M. Sarro "Measurement of thermal conductivity and diffusivity of single and multilayer membranes", Sensors and Actuators, Vol. 76, pp.323–328, 1999

34. Bruce C.S Chou, Chung-Nan Chen and Jin-Shown Shie, "Fabrication and Study of a Shallow-Gap Pirani Vacuum Sensor with a Linearly Measurable Atmospheric Pressure Range", Sensors and Materials, Vol. 11, No.6, pp.383-392, 1999

35. S. M. Sze, "*Semiconductor Sensors*", John Wiley & Sons, Inc., 1994

36. A.W. Herwaarden and P.M. Sarro, "Integrated vacuum sensor", Sensors and Actuators, Vol. 8, pp.187–196, 1985

37. Albert M. Leung, "Pressure sensor based on short-distance heater conduction in gases", report in Feb. 2001

38. S. Wessel, M. Parameswaran, S.R. Morrison and R.F. Frindt, "A CMOS thermally-isolated heater structure as a substrate for semiconductor gas sensors", Microelectronics Journal, Vol. 23, pp.451-456, 1992

39. J Robadey, O Paul and H Baltes, "Two-dimensional integrated gas flow sensors by CMOS IC technoloty", J. Micromach. Microeng. Vol. 5, pp.243-250, 1995

40. Goodfellow Cambridge Corporation, "Index of Materials", http://www.goodfellow.com/csp/active/static/A/A.htm, accessed 2004-07-20